Title
Surface-Atmosphere Connections on Titan: A New Window into Terrestrial Hydroclimate

Author
Faulk, Sean

Publication Date
2018

Peer reviewed|Thesis/dissertation

UNIVERSITY OF CALIFORNIA
Los Angeles

Surface-Atmosphere Connections on Titan:
A New Window into Terrestrial Hydroclimate

A dissertation submitted in partial satisfaction
of the requirements for the degree
Doctor of Philosophy in Geophysics and Space Physics

by

Sean Faulk

2018

ABSTRACT OF THE DISSERTATION

Surface-Atmosphere Connections on Titan:
A New Window into Terrestrial Hydroclimate

by

Sean Faulk
Doctor of Philosophy in Geophysics and Space Physics
University of California, Los Angeles, 2018
Professor Jonathan Lloyd Mitchell, Chair

This dissertation investigates the coupling between the large-scale atmospheric circulation and surface processes on Titan, with a particular focus on methane precipitation and its influence on surface geomorphology and hydrology. As the only body in the Solar System with an active hydrologic cycle other than Earth, Titan presents a valuable laboratory for studying principles of hydroclimate on terrestrial planets. Idealized general circulation models (GCMs) are used here to test hypotheses regarding Titan's surface-atmosphere connections. First, an Earth-like GCM simulated over a range of rotation rates is used to evaluate the effect of rotation rate on seasonal monsoon behavior. Slower rotation rates result in poleward migration of summer rain, indicating a large-scale atmospheric control on Titan's observed dichotomy of dry low latitudes and moist high latitudes. Second, a Titan GCM benchmarked against observations is used to analyze the magnitudes and frequencies of extreme methane rainstorms as simulated by the model. Regional patterns in these extreme events correlate well with observed geomorphic features, with the most extreme rainstorms occurring in mid-latitude regions associated with high alluvial fan concentrations. Finally, a planetary surface hydrology scheme is developed and incorporated into a Titan GCM to evaluate the roles of surface flow, subsurface flow, infiltration, and groundmethane evaporation in Titan's climate. The model reproduces Titan's observed surface liquid and cloud distributions, and reaches an equilibrium state with limited interhemispheric transport where atmospheric transport is approximately balanced by subsurface transport. The equilibrium state suggests that Ti-

tan's current hemispheric surface liquid asymmetry, favoring methane accumulation in the north, is stable in the modern climate.

The dissertation of Sean Faulk is approved.

Steven Adam Margulis

Jonathan M Aurnou

Seul Gi Moon

Jonathan Lloyd Mitchell, Committee Chair

University of California, Los Angeles

2018

TABLE OF CONTENTS

LIST OF FIGURES

LIST OF TABLES

ACKNOWLEDGMENTS

Of course, I must first thank Jonathan Mitchell, whose unrelenting patience and support has made all this possible. I have also had a number of co-advisors in Simona Bordoni, Seulgi Moon, and Juan Lora, each of whom have had an incredible impact on my learning and growth. I want to also acknowledge and thank Jon Aurnou, Steve Margulis, Chris Milly, Abby Kavner, Spencer Hill, Matt Walker, and Alex Gonzalez for stimulating and encouraging discussions. Each one of these people has taught me a great deal not just about science, but about the nature of science and what it means to be a scientist. I owe them a great deal.

I must also thank all my friends and family, nearly all of whom had no idea what it was I did day-to-day, and yet they were on my side throughout the trials of graduate school. In particular I want to thank my sister for always inspiring me to be the best I can be, and my parents for supporting me in all that I do, no matter what. Thank you.

VITA

2011 B.S. (Humanities and Science), Massachusetts Institute of Technology.

2015 M.S. (Geophysics and Space Physics), UCLA, Los Angeles, California.

2013-2017 Teaching Assistant, Department of Earth, Planetary, and Space Sciences, UCLA.

PUBLICATIONS

Faulk, S., Mitchell, J., Moon, S. & Lora, J. Regional patterns of extreme precipitation on Titan consistent with observed alluvial fan distribution. *Nature Geoscience* **10**, 827 (2017).

Faulk, S., Mitchell, J., Bordoni, S. Effects of rotation rate and seasonal forcing on the ITCZ extent in planetary atmospheres. *Journal of the Atmospheric Sciences* **74**, 665-678 (2017).

CHAPTER 1

Introduction and Background

1.1 Motivations, and thoughts on surface-atmosphere connections

Titan is the focus of this work, but it is not the heart of it. The heart of it is the question of what, fundamentally, forms a planet's climate. Titan's facts—including the fact that it is the largest moon of Saturn, that it rotates sixteen times slower than Earth, that it has a nitrogen-dominated atmosphere bearing a surface pressure one and a half times that of Earth's, that its atmosphere contains a variety of complex hydrocarbons and haze, that its low solar insolation (when combined with the radiative properties of the atmosphere) forces the surface temperature to hover at ∼93 K, near the triple point of methane, allowing for standing bodies of surface liquid and an active hydrological cycle rivaling that of Earth's but with methane as the condensible—should be parsed in the reader's mind as they have been in our work: as inputs into a simulation. A simulation of a blank planet. Titan's fancies and lineaments should be thought of then as manifestations of general planetary and climatic principles. As processes writ large and small. Indeed, if one could, it would serve to forget even the moon's name, to think of it as a blank-faced planetary body subject to physics, and avoid all together the dangers of isolating it as an entity set in its own universe rather than in this one.

Like Earth, Titan is a complex system wherein the workings of the atmosphere—wind, temperature, and precipitation (the latter dominating our interest in this work)—express themselves onto the surface in the form of moisture accumulation and geomorphic work, and in turn, the surface shapes the atmosphere through energy fluxes and topography-controlled forcings. That is to say that the surface and atmosphere are interacting components in a

greater system. We cannot hope to study one without the other. So too, in the spirit of comparative planetology, must we think about Earth and Titan: we cannot hope to study one without the other; if we are to understand the greater system, or paradigm, of planetary climate.

The surface-atmosphere interface provides the setting for an array of moisture transport phenomena that, dynamic and oftentimes mercurial, characterize worlds. Seasonally shifting large-scale circulations, baroclinic storms, local convection and lake evaporation, runoff into river channels and lake networks, infiltration into subsurface aquifers, and phreatic zone flow all occur on Earth and almost definitely on Titan as well. The study of such processes, when combined with their impact on a planet's climate, can be generalized as a planet's hydroclimate. Earth's hydroclimate has been extensively studied, while Titan's, which is perhaps comparably complex, is just beginning to be explored. Roe (2012)[1] summarizes as follows:

> [T]hese complex interrelationships of processes have led to a push for a systems approach to studying Earth, often referred to as Earth System Science. Titan deserves a similar systematic approach. However, the complexity of the Titanian system and the general paucity of data have led most modeling efforts relevant to methane weather to investigate individual phenomena rather than the surface-atmosphere system as a whole. Titan System Science as an approach to studying weather phenomena on Titan is in its infancy.

Our goal in this dissertation is to push 'Titan System Science' one step forward and begin to unmask the surface-atmosphere connections forming the backbone of its hydroclimate. In doing so, we will be able to demystify, or at least contextualize, Earth's complexity and enable further studies of planetary systems, including all those exoplanetary systems no doubt coming as part of the impending explosion of transiting terrestrial planet discoveries (e.g. Ricker et al., 2010)[2]. This introductory chapter reviews the essential observations and planetary frameworks for both the atmosphere (Section 1.2) and surface (Section 1.3) of Titan, and summarizes the development and motivations behind the models used in this work (Section 1.4).

1.2 Atmosphere

1.2.1 Observations

Although the first measurements of Titan's atmosphere were taken by the Voyager 1 mission during a flyby in 1980, we limit our observational discussion primarily to the more recent and more illuminating Cassini spacecraft, which arrived at Saturn in 2004, as well as to concurrent ground-based observations. The Huygens lander measured the local atmospheric composition (specific to 10°S latitude) as it descended to the surface, and reported that the troposphere is composed almost entirely of nitrogen, with methane constituting much of the remainder, at ∼5% below 8 km (Niemann et al., 2005)[3]. The vertical methane profile approximately follows the methane moist adiabat, indicative of a thermodynamically active constituent capable of lifting and condensation that, when combined with the temperature profile (Fulchignoni et al., 2005)[4], could result in clouds (Barth and Rafkin, 2007; Barth and Rafkin, 2010)[5, 6]. Studies suggest that given sufficient moisture, since the troposphere is either convectively unstable or conditionally unstable and able to support convection of saturated parcels (Griffith et al., 2008; Schinder et al., 2011)[7, 8], Titan's troposphere could even nourish convective rainstorms (Tokano et al., 2005; Lorenz et al., 2005; Hueso and Sánchez-Lavega, 2006; Mitchell et al., 2009; Barth and Rafkin, 2010, Rafkin and Barth, 2015)[9, 10, 11, 12, 6, 13].

Indeed, an extensive cloud distribution in both space and time has been observed on Titan, evidencing the moon's substantial methane-based hydrological cycle (see Roe (2012)[1] and Griffith et al. (2014)[14] for in-depth reviews of Titan's weather). Upon first arriving, during the peak of Titan's southern summer, Cassini primarily detected clouds over the south pole (Griffith et al., 2000; Brown et al., 2002; Roe et al., 2002; Bouchez et al., 2005; Schaller et al., 2006a)[15, 16, 17, 18, 19], with less pronounced cloud activity in the southern mid-latitudes (Griffith et al., 2005; Porco et al., 2005; Roe et al., 2005)[20, 21, 22]. The cloud distribution changed, though, as southern summer progressed into northern spring. Polar clouds dissipated (Schaller et al., 2006b)[23], mid-latitude clouds became more persistent (Rodriguez et al., 2009; Brown et al., 2010; Turtle et al., 2011a; Rodriguez et al., 2011)[24,

25, 26, 27], and large storms occurred in the low latitudes (Schaller et al., 2009; Turtle et al., 2011b)[28, 29]. While precipitation has not been directly observed, it has been inferred from surface darkening best explained by dark hydrocarbon liquid rainfall reaching the surface in the wake of a storm (Turtle et al., 2011b)[29].

The changes in cloud distribution in correspondence with the seasonal cycle suggest a connection to the seasonally driven large-scale circulation. On Earth, the seasonally oscillating Hadley cell carries heat and momentum poleward from the equator and converges moisture equatorward at the Intertropical Convergence Zone (ITCZ). The ITCZ is associated with the ascending branch of the Hadley cell and is thus a region of moist uplift and deep convection that migrates seasonally with the maximum insolation, rarely straying far from the equator. Titan exhibits an analogous convergence zone, with the essential difference being that Titan's zone migrates farther off the equator, nearly to the pole, suggesting a global Hadley cell (Mitchell et al., 2006; Roe, 2012)[30, 1]. When Cassini first arrived during the peak of southern summer solstice, Titan's convergence zone was located in the south polar region, explaining the abundance of cloud observations in that region immediately upon the spacecraft's arrival. As southern summer ended, though, polar clouds became less frequent and mid-latitude clouds and even equatorial clouds began to form; and upon this writing in early 2018, as Titan progresses deep into northern summer, clouds have been observed in the northern mid-latitude and polar regions (Turtle et al., 2017)[31], indicating the seasonal convergence zone has relocated almost completely to the opposite hemisphere.

Further evidence of Titan's global Hadley cell can be found in the atmospheric temperature structure. The Hadley cell works to redistribute heat from the equator and thus flattens temperature gradients. Temperature measurements of the troposphere from Cassini radio occultations (Schinder et al., 2011, 2012)[8, 32], surface brightness temperatures (Jennings et al., 2009; Jennings et al., 2016)[33, 34], and near-surface measurements from Voyager 1 (Samuelson et al., 1997)[35] all show weak equator-to-pole temperature gradients of only a few degrees, indicative of the presence of a nearly globe-spanning overturning cell efficiently creating uniform temperatures.

1.2.2 A primer on Hadley Cell theory

The Hadley cell represents a planetary atmosphere's zonal mean meridional mass flux. This thermally direct, meridional overturning cell consists of rising air in the region of greatest insolation and subsiding air poleward. If one considers an axisymmetric circulation wherein frictional eddies are absent, angular momentum of the air transported poleward is conserved. Earth's subtropical jet thus arises from angular momentum conservation, since stronger westerly winds are required at higher latitudes in order to conserve the angular momentum $M = \Omega a^2 cos^2\phi + uacos\phi$. In accordance with thermal wind balance, the Coriolis acceleration on the subtropical jet must be balanced by a meridional gradient in atmospheric temperatures. Thus, a meridional circulation is required to transport heat from the deep tropics to the subtropics and provide the subtropical temperature gradients necessary to sustain the jet. Another way to understand the existence of the circulation is to consider the case without one: in radiative equilibrium, the temperature gradient in the deep tropics is too large to maintain angular-momentum conserving winds in the presence of angular momentum diffusion, thereby violating a condition known as Hide's theorem (Schneider, 2006)[36].

The extent of the meridional circulation is set by global conservation of energy. Held and Hou (1980)[37] developed a theory for steady axisymmetric, nearly inviscid circulations where they assume that the circulation is energetically closed, such that the diabatic heating in the ascending branch balances the diabatic cooling in the descending branch, and that continuity of temperatures exists at the boundaries of the circulation. With these assumptions, they derive a meridional extent for the steady Hadley circulation:

$$\phi_H = (5/3Ro)^{1/2} \tag{1.1}$$

where $Ro = \frac{gH\Delta_H}{\Omega^2 a^2}$ is the thermal Rossby number, H is the scale height, and Δ_H is the pole-to-equator temperature difference. The resulting circulation has nearly uniform temperatures within the circulation and transitions to radiative-convective equilibrium poleward of the circulation extent, which at $\sim 30^\circ$ closely resembles Earth's actual annual-mean Hadley

circulation.

The simple scaling above suggests that given its slower rotation rate and smaller radius, Titan's Hadley cell should be wider than Earth's, in correspondence with a weaker Coriolis force that requires a weaker meridional temperature gradient under thermal wind balance (Mitchell and Lora, 2016)[38]. Indeed, Titan's high Rossby number may force a global circulation, leading to an "all tropics" climate on the moon dominated by the mean meridional circulation (Mitchell et al., 2006)[30].

The theory above neglects the impact of baroclinic eddies, which would affect the circulation extent. A complete theory incorporating macroturbulent eddies and their resulting alterations to the Hadley cell width and strength has yet to be developed, but the simulations presented in this dissertation add to the body of work being done in that effort (Schneider, 2006; Walker and Schneider, 2006; Bordoni and Schneider, 2008; Schneider and Bordoni, 2008; Levine and Schneider, 2015)[36, 39, 40, 41, 42]. Still, the mean meridional circulation appears to dominate the moisture transport in Titan's methane cycle, particularly in the lower and middle latitudes (Lora and Mitchell, 2015)[43]. Mitchell (2012)[44] showed that the TOA radiative imbalance in Titan's lower latitudes is large enough to drive a vigorous methane cycle, despite low solar insolation, with substantial latitudinal heat transport executed primarily by the seasonal component of the circulation during solstitial periods. This heat is transported mainly through latent heat fluxes, drying the lower latitudes and moistening the higher latitudes. Thus, even though Titan's atmosphere has a large thermal inertia that would otherwise mute the seasonal cycle, surface-atmosphere coupling that allows communication between the surface and troposphere through boundary layer latent and sensible energy fluxes allows for a substantial seasonal cycle in Titan's lower atmosphere (Mitchell and Lora, 2016)[38].

The influence of boundary layer forces on the meridional circulation is also unclear. Flow is ultimately driven by a confluence of dynamic forces; and the way those forces interact, producing convergence and precipitation in the wake of flow, deserves attention. While the dominant force balance on Earth is geostrophic, Titan's weaker rotation rate leads to a predominantly cyclostrophic balance (Flasar and Achterberg, 2009)[45] between pressure

gradient and centrifugal forces, though winds may be strong enough in the lower troposphere to produce gradient flow between pressure gradient, centrifugal, and Coriolis forces.

Much of the literature on Earth's ITCZ has focused on thermodynamic controls, mostly separate from the dynamical controls imposed by the large-scale circulation. Precipitation and convergence have been argued to stem predominantly from local temperature and moisture profiles as computed by local moisture and energy budgets (Sobel and Neelin, 2006)[46]. In this way, a number of thermodynamic diagnostics have been linked to the ITCZ: the warmest surface temperatures, for instance, have historically dominated predictions of maximum convergence (such that the warmest sea surface temperatures are collocated with the maximum convergence (Neelin and Held 1987)[47], particularly under weak temperature gradient conditions found often in the tropics and, for that matter, on Titan); moist static energy, which includes the latent energy from moisture in addition to internal heat and potential energy, has also been suggested to coincide with the ITCZ (Privé and Plumb, 2007; Bordoni and Schneider, 2008)[48, 40], though the framework behind this diagnostic is indeed coupled to large-scale circulation theories, making it a hybrid thermodynamic-dynamic control; and the energy flux equator, a measure related to global energy balance (e.g. Kang et al., 2008)[49], has recently explained shifts in the ITCZ due to both tropical and extratropical forcings (Schneider et al., 2014)[50]. Exploring these same controls in a slowly rotating regime, such as that on Titan, will shed light on to their efficacy in driving flow and convergence.

In Chapter 2, we survey atmospheric circulations over varying rotation rates to further test and develop Hadley cell circulation theory and understand the influences of baroclinic eddies, seasonality, boundary layer forces, and thermodynamic controls on moist tropical dynamics, and in particular on the location of the seasonal convergence zone, or ITCZ. Parameter space studies using idealized GCMs are useful for addressing basic principles of atmospheric dynamics and climate given simple planetary parameters. In this way, Titan and Earth can be considered exoplanets, and their climates will be discussed in the context of thermodynamic and dynamic controls on the seasonal circulation.

1.3 Surface

1.3.1 Observations

Though most of the methane on Titan exists in the atmosphere, so much so that if it were all to rain out it would create an ocean approximately five meters deep (Tokano et al., 2006)[51], perhaps the most intriguing facet of Titan's climate is the liquid methane on its surface (Hayes, 2016)[52]. The observed surface liquid (assumed to be predominantly methane, with varying levels of ethane mixed in (Glein and Shock, 2013; Tan et al., 2015; Hayes, 2016; Mastrogiuseppe et al., 2016)[53, 54, 52, 55]) is concentrated almost entirely in Titan's polar regions—a result, to first order, of moisture transported by the global circulation and accompanying seasonal convergence zones discussed in the previous section (though the work of this dissertation underlines potential topographic controls on polar methane buildup—see Chapter 4).

Lake districts as observed by the Cassini radar instrument (Stofan et al., 2007; Hayes et al., 2008)[56, 57] populate the higher latitudes and are particularly prevalent in the north, a fact attributed primarily to Saturn's orbital eccentricity driving Milankovitch-like climate cycles over millennia timescales (Aharonson et al., 2009; Lora et al., 2014; Liu and Schneider, 2016)[58, 59, 60]. In fact, the only substantial surface hydrocarbon reservoir in the southern hemisphere is Ontario Lacus (Turtle et al., 2009; Wall et al., 2010)[61, 62], while the north polar region boasts three maria—Kraken Mare, Ligeia Mare, and Punga Mare—that altogether comprise $\sim$80% of all Titan's liquid-filled surfaces by area (Hayes et al., 2008, Hayes, 2016). Broad depressions suggestive of dry paleoseas (Hayes et al., 2017; Birch et al., 2017a)[63, 64] and potential evaporite deposits, both in the north (Barnes et al., 2011)[65] and in the south outlining shorelines around Ontario Lacus (Barnes et al., 2009)[66], indicate the influence of long-term climatic changes on Titan's surface character. However, the lack of observed evaporite deposits surrounding ancient maria basins in the southern hemisphere is perplexing (Mackenzie et al., 2014)[67]. In addition, though unconfirmed, candidate lakes and paleoseas have also been identified in the lower latitudes (Griffith et al., 2012; Vixie et al., 2015)[68, 69]. Since the lower latitudes are predominantly dry regions

noted for their preponderance of dunes (Lorenz et al., 2006a; Radebaugh et al., 2008; Le Gall et al., 2011)[70, 71, 72], the possible identification of surface liquids in the low latitudes, when combined with the lack of observed evaporite deposits and also the lack of observed surface liquids in the deepest depressions (lower than Ontario Lacus) in the south polar region (Mackenzie et al., 2014; Dhingra et al., 2017)[67, 73], further complicates the picture of Titan's surface-climate connections.

Cassini has illuminated not just standing bodies of liquid, but also, through the radar and Visual and Infrared Mapping Spectrometer (VIMS) instruments, extensive geomorphic features suggestive of fluvial erosion. Of most importance to us in this work is the vast collection of observed dendritic valley networks (Tomasko et al., 2005; Elachi et al., 2005; Porco et al., 2005; Lorenz et al., 2008a; Lunine and Lorenz, 2009; Le Gall et al., 2010; Lopes et al., 2010; Langhans et al., 2012; Burr et al., 2013a)[74, 75, 21, 76, 77, 78, 79, 80, 81] and alluvial fans (Birch et al., 2016; Radebaugh et al., 2016; Cartwright and Burr, 2017)[82, 83, 84]. Dunes and dryness dominate the lowest latitudes, but channel networks have been observed even there, including at the Huygens landing site (Elachi et al., 2005)[75]; indeed, channel networks have been found to exist at all latitudes (Tomasko et al., 2005)[74], though only filled when feeding the higher-latitude maria in the form of river deltas and valleys (Wall et al., 2010; Burr et al., 2013a)[62, 81]. Alluvial fans detected by the radar instrument appear to be concentrated in the mid- to high latitudes, from 50-80°, suggesting the potential for large discharges enabling sediment transport in those regions (Birch et al., 2016)[82]. The mid-latitudes, 30-60°, are noted for the broad regions bright at 5 microns as seen by VIMS (Barnes et al., 2011)[65], and the vast expanses of radar-dark, uniform terrain in SAR known as the undifferentiated plains (Lopes et al., 2010)[79], a geomorphological feature that may be indicative of depositional and/or sedimentary processes of primarily aeolian nature, though fluvial origins cannot be ruled out (Lopes et al., 2016)[85]. At higher latitudes, a relative lack of craters (Wood et al., 2010; Neish and Lorenz, 2012)[86, 87] and depressed surface elevation (Lorenz et al., 2013; Corlies et al., 2017)[88, 89] suggest the existence of extensive "wetlands" regions (Neish and Lorenz, 2014)[90], where fluvial erosion likely plays a large role in modifying craters (Neish et al., 2016)[91].

1.3.2 The intrigue of planetary geomorphology

Our focus above on the regional distribution of geomorphic features is motivated by the hypothesis that regional climate strongly influences regional surface expression. Previous studies have suggested that mechanical erosion of icy bedrock by surface runoff from methane precipitation is a fundamental driver in producing the observed surface features, as opposed to thermal, chemical, and seepage erosion; and erosion rates for specific valley formations have been derived (Perron et al., 2006; Jaumann et al., 2008; Black et al., 2012)[92, 93, 94]. Indeed, the icy bedrock and methane flow parameters have been shown to be favorable for erosion on Titan (Collins et al., 2005; Burr et al., 2006; Litwin et al., 2012) [95, 96, 97]. Inferred minimum precipitation rates needed to mobilize sediment for the Huygens landing site range from 0.5 to 15 mm/hr (Perron et al., 2006)[92], but these rates are higher than averaged precipitation rates from general circulation model (GCM) simulations, which typically exhibit average rainfall rates that range from 0.05 to 0.5 mm/hr and rarely reach 10 mm/hr (Schneider et al., 2012; Lora et al., 2015; Mitchell and Lora, 2016; Newman et al., 2016)[98, 99, 38, 100]. It has been suggested that precipitation rates from individual, large outbursts can be more intense, at both low latitudes (Schneider et al., 2012)[98] and high latitudes (Newman et al., 2016)[100], indicating a dependence on model configuration.

The intimate connection between landscape morphology and climate has been established on Earth (Perron, 2017)[101]. Precipitation in particular alters landscapes in a variety of ways, from adjusting river profiles (Whipple and Tucker, 1999; Seybold et al., 2017)[102, 103], to incising channels (Molnar et al., 2006; Dibiase and Whipple, 2011; Ferrier et al., 2013)[104, 105, 106], to initiating sedimentary transport that results in conspicuous deposit features such as alluvial fans (Blair and McPherson, 1994; Borga et al., 2014; Cook et al., 2015; D'Arcy et al., 2017)[107, 108, 109, 110]. Furthermore, terrestrial studies on geomorphology have emphasized the importance of precipitation and discharge *variability* on fluvial erosion processes, showing that rare but extreme precipitation events with high magnitudes can erode more efficiently than stable precipitation (Wolman and Miller, 1960; Tucker and Bras, 2000; Dibiase and Whipple, 2011)[111, 112, 105].

Given the above, a planetary surface—the dynamic interface upon which the atmosphere and hydrosphere act—serves as a record of climatic events through the lens of geomorphic features, thus enabling interpretations of climate via surface observations. Titan then presents a unique opportunity to test terrestrial geomorphic processes and theory in an exotic planetary setting with entirely different materials. Indeed, just as newly discovered landscapes in Africa, Asia, Australia, and North America ignited the field of geomorphology in the late 19th and early 20th centuries, images of planetary surfaces in our current spacecraft era have reignited geomorphologic study a century later (Baker, 1984)[113]. Extensive comparative planetary geomorphology has been predominantly mediated through the investigation of impact craters and large-scale volcanic features on the Moon, Venus, Mars, and several icy satellites, whereas the comparative study of hydrologically-linked features such as debris flows, flood channels, and other mechanically eroded surfaces has been limited to only Mars—the landscape of which retains remnants of its ancient, wetter climate (Milton, 1973; Baker and Milton, 1974; Craddock and Howard, 2002; Moore and Howard, 2005; Hynek et al., 2010; Jacobsen and Burr, 2016)[114, 115, 116, 117, 118, 119]. Detailed images retrieved by the Cassini mission, however, present Titan as another body through which to understand hydroclimatic connections with geomorphology (Moore et al., 2014; Birch et al., 2017b)[120, 121]—an investigation that has only just begun given the recency of geomorphic discoveries on the moon, particularly the alluvial fans.

Other factors likely control landscape evolution on Titan, including tectonics (Burr et al., 2013b; Black et al., 2017)[122, 123], lithology (Cartwright and Burr, 2017)[84], and purported cryovolcanism (Lopes et al., 2013)[124], but we focus in this work on precipitation: not just because studies suggest it is a dominant driver of surface modification but also because it relates back to our interest in Titan's seasonal cycle. Sedimentary features on Earth, namely fluvial megafans, have been shown to be geographically distributed in correspondence with seasonal monsoons (Leier et al., 2005)[125] and influenced by monsoonal strength (Gibling et al., 2005)[126]. Similar correspondences on Titan would indicate a strong association between geomorphic work and seasonality on planetary bodies, further clarifying the role of climate in shaping planetary surfaces. Although we know that in general on Titan the

low latitudes are dry and the high latitudes are wet, the spatial and temporal character of rainfall frequency, intensity, and variability have not yet been quantified, nor have they been compared to observed surface features. Specifically, the range of magnitudes of storms at all latitudes, the occurrence rate of storms large enough to initiate significant erosion, and the overall hydroclimatic character of the mid-latitudes, plus the combined influence of these factors on geomorphic features, remain unclear. In Chapter 3 of this dissertation, we address these questions and argue that, indeed, surface-atmosphere connections on Titan also exist in the realm of geomorphology. We show a strong correlation between the regional distribution of alluvial fans and the regional distribution of intense (and likely baroclinic) storms, indicating precipitation's clear expression onto the surface.

1.3.3 Subsurface implications

Methane in Titan's stratosphere is being constantly, irreversibly destroyed by photolysis, after which hydrogen escapes and carbon polymerizes into the complex hydrocarbons that form its distinctive haze. Studies suggest that the photochemical lifetime of methane in Titan's atmosphere would be only 10–100 million years (Yung et al., 1984; Atreya et al., 2006)[127, 128], meaning that we are either observing Titan at a very special time in its evolution, or, more likely, the surface replenishes the atmosphere as part of a stable methane cycle. Atmospheric methane exceeds observable surface (predominantly lacustrine) methane by approximately an order of magnitude (Lorenz et al., 2008b)[129], however, necessitating an as yet unknown source to feed the atmosphere and maintain equilibrium over geologic timescales. Cryovolcanic release of methane gas trapped in interior clathrates (Atreya et al., 2006; Tobie et al., 2006)[128, 130] is one hypothesis, but here we limit our investigation to the more accessible (and more modellable, at least within the context of current GCMs) subsurface methane hypothesized to saturate the ground and be available for evaporation perhaps just inches below the surface, analogous to groundwater on Earth.

Though no direct evidence for subsurface methane exists, there have been several observations that strongly suggest its presence. The Huygens probe landed in a dark, flat area

believed to be a dry riverbed and returned clear images of rounded "ice" boulders (Lebreton et al., 2005; Tomasko et al., 2005)[131, 74]. Subsequent analysis determined that the probe landed on terrain with the consistency of wet sand, damp with liquid methane, rather than on a dry, fine-grained surface (Zarnecki et al., 2005; Lorenz et al., 2006b)[132, 133], indicating the possibility of subsurface methane. In addition, for any given drainage basin in the northern lake districts, empty lake floors have been observed to typically be at higher elevations than nearby filled lakes, substantiating claims of local hydraulic connectivity by way of a regional methane aquifer or "methane table" (Hayes et al., 2008; Hayes, 2016; Hayes et al., 2017)[57, 52, 63]. Furthermore, subsurface fluids have been suggested to explain Titan's mountain ridge morphology indicative of contractional tectonism—structures that would otherwise require unfeasibly large stresses to form in ice (Liu et al., 2016)[134].

These observations, combined with near-surface humidity measurements indicating more surface liquid coverage than is presently observed in the lakes (Ádámkovics et al., 2016; Lora and Ádámkovics, 2017)[135, 136], make the case for a potentially substantial subsurface methane reservoir connected to the global methane cycle. Indeed, the "wetlands" version of the Titan Atmosphere Model (TAM; Lora et al., 2015)[99], hereafter referred to as TAM wetlands, is one of the GCMs most capable of reproducing Titan's observed hydrologic cycle (and the one used for Titan simulations in this dissertation) in large part because it imposes extensive and deep reservoirs of methane in the high latitudes, enabling evaporative recharge of the atmosphere from a reservoir much greater than that of the observed lakes and seas (Lora and Mitchell, 2015)[43]. In Chapter 4, we present updates to this model wherein we add surface hydrology components, including overland surface flow and a global subsurface methane table connected to the atmosphere via evaporation, in order to reproduce a similarly successful meteorological cycle as TAM wetlands but with more realistic physics.

1.4 Model development

Idealized climate models are well-suited to investigating general principles of planetary climate. Oftentimes, overarching themes are lost amid the complexity of modern Earth GCMs

that are tuned to capture very specific elements of Earth's climate. The power of idealized models becomes particularly pronounced when considering planetary science questions. Lacking detailed observations, we can leverage simple models of planetary bodies such as Venus, Mars, and Titan to understand fundamental processes. In this section, we briefly review the predecessors of the models used in this dissertation, clarify our models' place in the hierarchy of idealized model development, and conclude the chapter by outlining the remainder of the dissertation.

1.4.1 Previous Titan models

Efforts to understand Titan's meteorological cycle and the spatial and temporal distribution of observed clouds and surface liquids have primarily been carried out through constructing GCMs. Axisymmetric models coinciding with the earliest Cassini observations successfully produced the basic dichotomy of Titan's surface, i.e. dry low latitudes and wet high latitudes, with the large-scale circulation transporting methane towards the poles and drying the low latitudes (Mitchell et al., 2006; Rannou et al., 2006; Mitchell, 2008)[30, 137, 138]. Models using "aquaplanet" configurations with a slab ocean of unlimited liquid available for evaporation showed that high-latitude precipitation was clearly linked to the availability of local surface methane (Mitchell et al., 2006; Rannou et al., 2006; Mitchell, 2008; Lora et al., 2015; Newman et al., 2016)[30, 137, 138, 43, 100]. However, aquaplanet runs robustly produce far more precipitation than is observed, typically exhibiting a zonal precipitation band not unlike Earth's ITCZ (perhaps unsurprisingly given Earth's essentially global ocean). Such consistent seasonal cloud cover is incongruent with Titan's observed cloud distribution, which features more sporadic cloud activity in the low latitudes and mid-latitudes.

Recent 3D models with further developed surface schemes and boundary conditions have improved at reproducing the observed cloud distribution, particularly the low-latitude and mid-latitude clouds (Schneider et al., 2012; Lora et al., 2015; Lora and Mitchell, 2015; Mitchell and Lora, 2016; Newman et al., 2016)[98, 99, 43, 38, 100]. To replace the aquaplanet setup, these models employed a "bucket model" with a limited methane reservoir

such that methane accumulates in each grid cell as calculated by the difference between local precipitation and local evaporation. However, each bucket could be infinitely deep, and no spillover occurred from one bucket to the next. Schneider et al. (2012)[98] added a diffusive horizontal transport to represent surface and subsurface flow, which is suggested to contribute to low-latitude mid-latitude storm occurrence; but the horizontal transport does not adequately account for the influence of topography in driving methane flow, rendering it physically implausible. TAM wetlands (Lora and Mitchell, 2015)[43], introduced briefly in the previous section, produced low-latitude and mid-latitude clouds by imposing deep surface liquid reservoirs poleward of 60° and infiltration equatorward of 45° to reduce methane availability in the lower latitudes. It was originally motivated by observations of crater scarcity in the polar lowlands that was interpreted as evidence for extensive wetlands regions there (Neish and Lorenz, 2014)[90]. More recent measurements of surface temperatures (Jennings et al., 2016)[34] and near-surface relative humidity values (Lora and Ádámkovics, 2017)[136] betray the presence of additional polar methane reservoirs other than those observed in lakes and seas, further arguing for the existence of wetlands regions.

No GCM to date, though, implements physically reasonable parameterizations of surface hydrology, particularly subsurface storage and methane flow as determined by topography. Methane evidently accumulates in the polar regions, but the extent to which the lowland topography in the high latitudes contributes to this accumulation and the resulting methane cycle is unknown. Horvath et al. (2016)[139] began to address the role of surface hydrology by modeling surface and subsurface flow in Titan's north polar region, showing that subsurface flow and choice of permeability values are crucial towards reproducing the observed lakes. However, the model used precipitation and evaporation values from averaged GCM outputs, precluding surface-atmosphere coupling. A full GCM with surface and subsurface flow coupled to the global atmospheric circulation is thus necessary to address the subtleties of Titan's global surface liquid transport.

1.4.2 Titan Atmospheric Model (TAM)

A majority of the work presented in this dissertation is founded on the Titan Atmospheric Model (TAM), originally reported in the literature by Lora et al. (2015)[99]. TAM is a fully three-dimensional GCM borne from the Geophysical Fluid Dynamics Laboratory's (GFDL) Flexible Modeling System (FMS) infrastructure that utilizes the FMS spectral dynamical core to solve the primitive equations. As presented in Lora et al. (2015), the model successfully reproduces Titan's observed temperature profile and atmospheric superrotation, two constraints that previous models struggled to simulate. While our focus in this dissertation is on the troposphere, using a model that adequately resolves the stratosphere and is benchmarked against critical stratospheric observations lends credence to our tropospheric analysis. Since TAM shares the same lineage as the model used in Chapter 2 and serves as the foundation for the models used in Chapter 3 and Chapter 4, we devote some space here to give a brief description of the core physics components of the GCM, retained in the models used in Chapter 3 and Chapter 4. Full descriptions of the original model's component physics modules are available in Lora et al. (2015)[99].

1.4.2.1 Moist processes

All condensation is assumed to be liquid, rendering parameterization of ice condensation, detailed microphysics, and the ice-liquid transition unnecessary in our model. The effects of clouds are also ignored in the radiative transfer. Methane saturation vapor pressure is calculated over a 90/10 CH_4/N_2 liquid using the Clausius-Clapeyron equation, and the effects of ethane on methane vapor pressure are ignored.

Precipitation in TAM has two components: large-scale condensation and quasi-equilibrium moist convection. In large-scale condensation (LSC), precipitation occurs (methane condenses) when the relative humidity at a given pressure level exceeds saturation; the resulting condensed methane is allowed to re-evaporate into the atmosphere as it falls (the entire column must be fully saturated for rain to fall to the ground). For convection, we employ the Betts-Miller convection scheme (Frierson et al., 2007)[140] where precipitation rates are

calculated from vertical profiles of temperature and humidity, and then, over a specified timescale, temperature is relaxed to the moist adiabat and moisture is relaxed to a specified relative humidity with respect to the moist adiabat. In this dissertation, we set the relaxation time and the reference relative humidity to 2 hours and 80%, respectively. The scheme assumes quasi-equilbirum (QE), wherein: 1) the boundary layer moist static energy is connected to the free tropospheric temperature, 2) precipitation and relative humidity are well correlated, and 3) moisture is available for relatively short timescales (less than a day). Studies have shown that such conditions are typically present in Earth's tropics, where convection is dominant (Brown and Bretherton, 1997; Bretherton et al., 2004)[141, 142].

This convection scheme is largely insensitive to the relaxation time (Frierson et al., 2007)[140]. Its simplicity of only two specified parameters makes it ideal for modeling planetary atmospheres (e.g. Mitchell, 2006)[30] while also being computationally efficient. Other convection schemes have difficulty simulating precipitation distributions within the ITCZ, which is of critical importance to us given our interest in seasonal moisture transport.

1.4.2.2 Boundary layer diffusion

The Richardson number is measure of buoyancy, given as the ratio of potential to kinetic energy, and determines both the height of the boundary layer and the diffusion coefficients within it (as well as the drag coefficients at the surface; see following subsection). Once the Richardson number exceeds some prescribed critical Richardson number Ri_c, there is no drag, and so the boundary layer depth is set to the height where the bulk Richardson number exceeds Ri_c. For the boundary layer, the bulk Richardson number is given as $\frac{gz[\theta_v(z)-\theta_v(z_a)]/\theta_v(z_a)}{|v(z)|^2}$, where θ_v is the virtual potential temperature and z_a is the height of the lowest model level (the bulk Richardson number for the surface is calculated the same way, except for z values between zero and z_a). As the Richardson number increases, so does buoyant stability. A larger critical Richardson number would allow for increased convection within the boundary layer.

A constant-flux surface layer exists up to a specified fraction f_b, one-tenth in TAM, of

the boundary layer depth. The stable mixing cutoff occurs at the level where the bulk Richardson number exceeds 1 (i.e., Ri_c equals 1). The unstable mixing cutoff occurs at the level of neutral buoyancy for surface parcels. Turbulent diffusion coefficients K for heat, moisture, and momentum are calculated as a function of height z within the boundary layer of depth h, and according to Monin-Obukhov stability functions $\Phi(z)$ such that:

$$K(z) = \begin{cases} \dfrac{\kappa u_\star z}{\Phi(z)}, & \text{for } z < f_b h \\ \dfrac{\kappa u_\star z}{\Phi(z)}[1 - \dfrac{z - f_b h}{(1 - f_b)h}]^2, & \text{for } f_b h \leq z < h \end{cases} \tag{1.2}$$

where κ is the von Karman constant and $u_\star$ is the surface friction velocity, or the velocity at the lowest model level. The stability function $\Phi(z)$ is a similarity function determined by Monin-Obukhov similarity theory that relates fluxes to mean profile gradients of wind and buoyancy in the surface layer. The bulk Richardson number can be rewritten in terms of the stability functions in order to attain friction velocity and buoyancy scales, and proceed to calculate the turbulent diffusion coefficients above and the drag coefficients below, as from standard FMS code.

1.4.2.3 Surface-atmosphere fluxes

Surface fluxes of momentum, sensible heat, and latent heat enable communication with the atmosphere. They are calculated by standard bulk aerodynamic formulae, such that fluxes are proportional to the differences between surface level and lowest model level winds, potential temperature, and water vapor, respectively. Therefore, the fluxes for momentum, sensible heat, and evaporation are:

$$M = C\rho_a v_a(v_a) \tag{1.3}$$

$$S = C\rho_a c_p v_a(\Theta_a - \Theta_s) \tag{1.4}$$

$$E = C\rho_a v_a(q_a - q_s^\star) \tag{1.5}$$

where C is the drag coefficient, c_p is the heat capacity, Θ_s is the surface potential temperature, $q_s^\star$ is the saturation specific humidity at the surface temperature, and q_a, v_a, Θ_a, and ρ_a are the specific humidity, wind, potential temperature, and density at the lowest model level. Note that surface horizontal winds are set to zero, and the difference in vertical velocity, or the gustiness, is set to 0.1 m/s.

Drag coefficients C are determined from Monin-Obukhov similarity, dependent on the height of the surface model level z_a, the Richardson number at that lowest model level Ri_a, and the surface roughness length z_0, which is 0.5 cm in our simulations, such that:

$$C = \begin{cases} \dfrac{\kappa^2}{[\ln(z_a/z_0)]^2}, & \text{for } \mathrm{Ri}_a < 0 \\ \dfrac{\kappa^2(1-\mathrm{Ri}_a/\mathrm{Ri}_c)^2}{[\ln(z_a/z_0)]^2}, & \text{for } 0 < \mathrm{Ri}_a < \mathrm{Ri}_c \\ 0, & \text{for } \mathrm{Ri}_a > \mathrm{Ri}_c \end{cases} \tag{1.6}$$

Thus, if the surface is unstable, the drag coefficient does not depend on the Richardson number; whereas if the surface is stable, the drag coefficient reduces steadily as the Richardson number increases, indicating greater stability, and eventually approaching zero once the critical Richardson number is reached.

1.4.2.4 Surface temperature

Ground temperature is calculated using a simple soil model that performs heat conduction through an arbitrary number of soil layers. As boundary conditions, the heat flux is zero at the bottom of the soil column and H at the surface due to the contributions from radiation and the energy fluxes described above, such that:

$$H = F_{SW} - F_{LW} - S - L_v E \tag{1.7}$$

where F_{SW} is the net shortwave radiation absorbed by the top layer, F_{LW} is the net longwave radiation emitted by the top layer, S is the sensible heat flux from the ground,

and L_vE is the latent heat flux from the ground. Ground temperature is solved numerically using the Crank-Nicolson method.

1.4.2.5 Radiation

We employ nongray, multiple scattering, plane-parallel two-stream approximations in order to compute the solar-wavelength (<4.5 μm) and thermal infrared (>4.5 μm) fluxes. The algorithm computes the radiative transfer of a vertically inhomogeneous atmosphere in an accurate and computationally efficient manner, where each layer is defined by absorbing and scattering constituents determined by extinction optical depths, asymmetry parameters, single scattering albedos, and forward scattering fractions (Toon et al., 1989)[143]. Seasonal and diurnal cycles, as well as the effect from Saturn's eccentricity, are included into the insolation calculation.

Methane opacities at wavelengths less than 1.6 μm are derived from absorption coefficients measured by the Descent Imager/Spectral Radiometer (DISR) on Huygens (Tomasko et al., 2008a)[144]. Correlated k coefficients from HITRAN data are used to calculate methane opacities between 1.6 and 4.5 μm (Rothman et al., 2009)[145], opacities due to collision induced absorption (CIA) from N_2, CH_4, and H_2 pairs (Richard et al., 2012)[146], and molecular absorption from C_2H_2, C_2H_4, C_2H_6, and HCN (Rothman et al., 1999)[147], with exponential sum fits to pressure- and temperature-dependent transmissions. Profiles of methane (Niemann et al., 2005)[3] and stratospheric molecular species (Vinatier et al., 2007)[148] are fixed to those measured by Huygens (globally assumed) and Cassini Composite Infrared Spectra (CIRS) spectra, respectively.

Haze optical parameters in the shortwave range are set to those measured by DISR (Tomasko et al., 2008b)[149]. The haze distribution is assumed to be horizontally homogenous, and optical depth values not measured by DISR (those larger than 1.6 μm) are extrapolated using power law fits. We assume that haze in the thermal infrared is perfectly absorbing (i.e. the scattering albedo is zero). Optical depths are derived from extinction coefficients given by Cassini/CIRS spectra (Anderson and Samuelson, 2011; Vinatier et al.,

2012)[150, 151], with values for wavenumbers larger than 1500 cm^{-1} interpolated using a power law fit between CIRS and DISR data.

1.4.3 Our idealized models

Each of the three main chapters of this dissertation use a different idealized model. In Chapter 2, we use a moist aquaplanet GCM with gray radiation, wherein the radiative fluxes are only a function of temperature, thereby eliminating radiative feedbacks (Frierson et al., 2006)[152]. The moist processes, boundary layer diffusion, and surface fluxes are computed as described above for TAM. This simplified terrestrial model therefore presents a useful tool that can be applied to any planetary setting for studying the interplay between seasonal insolation, moisture effects, and the large-scale dynamics. Building off of the dry model with Newtonian cooling developed as a benchmark for GCM dynamical core comparisons (Held and Suarez, 1994)[153], Frierson et al. (2006)[152] included an explicit boundary layer model, replaced Newtonian cooling with gray radiation, and added a slab ocean of specified heat capacity as the lower boundary condition. The model was developed with flexibility in mind, such that each component could be sequentially added to form a full atmospheric GCM, thus allowing for the analysis of singular components. Moist convection is parameterized using the Betts-Miller scheme, which adjusts temperature to a moist adiabat and moisture to a specified relative humidity with respect to the moist adiabat over a specified timescale (Frierson, 2007)[140]. This scheme too promotes flexibility, given that it only depends on two parameters: the relative humidity to which moisture adjusts and the timescale over which the relaxation occurs. Since neither of these are tuned to Earth, the scheme can be applied to other planetary atmospheres, and indeed, as described above, the same scheme is used in our Titan models (Lora et al., 2015)[99]. The modular and flexible nature of the model enables us to use it to study a wide range of climates, including those of Earth-like planets with slower rotation rates (see Chapter 2).

In Chapter 3, we use the TAM wetlands model (Lora and Mitchell, 2015)[43] to assess the nature of intense, presumably baroclinic storms and their impact on the surface. Then

in Chapter 4, we present a new version of TAM by adding surface runoff and subsurface reservoir schemes that self-consistently reproduce the wetlands configuration in a physically realistic manner: by routing precipitated methane poleward into local topographic depressions and trapping low-latitude methane in subsurface stores deep beneath the surface. This model represents the latest in the Titan GCM hierarchy, and is also built with modularity and flexibility in mind, in that the surface hydrology scheme is decomposed into runoff, infiltration, groundmethane evaporation, and subsurface flow components, each of which can be toggled to assess their relative influences on the global methane cycle. Reproducing our results from Chapter 3 with the model from Chapter 4 demonstrates the powerful role of surface hydrology in Titan's methane cycle, particularly regarding the regional distribution of baroclinic storms. In addition, given Titan's unconstrained surface properties, none of these hydrology components are specifically tuned to Titan and can therefore be applied to any planetary system with a hydrologic cycle, further illustrating the model's capability in representing terrestrial systems in general.

Throughout this dissertation, the dual attention on Titan and Earth simultaneously distinguishes and interfuses them. One can interpret the work of the following chapter as applying Titan's ITCZ onto an Earth-like climate, and the work of the latter chapters as applying Earth's surface processes and baroclinicity onto a Titan-like climate. Indeed, it is through the work of displacing known processes to another environment that real knowledge is unearthed. The various thermodynamic and dynamic controls proposed for Earth's ITCZ may or may not be applicable in a more slowly rotating regime (Chapter 2, published as Faulk et al. (2017a)[154]). The considerable geomorphic work done by intense and (oftentimes) baroclinic storms on Earth's rocky surface may or may not exist on an icy satellite with methane rain (Chapter 3, published as Faulk et al. (2017b)[155]). And the intricate surface hydrology components of Earth's hydroclimate may or may not be important in a climate seemingly dominated by large-scale atmospheric transport (Chapter 4, in prep to be submitted May 2018). It is the work of this dissertation to answer these questions, and in doing so, reify our understanding of the surface-atmosphere connections dynamizing terrestrial climates.

CHAPTER 2

Seasonal Rain in Planetary Atmospheres

The following is adapted from Faulk et al. (2017a)[154], now in press.

2.1 Introduction

One of the most prominent features of Earth's large-scale atmospheric circulation in low latitudes is the intertropical convergence zone, or the ITCZ (Waliser and Gautier, 1993)[156]. Associated with the ascending branch of the Hadley cell, the ITCZ is the region of moist uplift, and thus of high precipitation and deep convection, occurring where the low-level winds of the two cells converge. During summer, this convergence zone migrates off the equator into the summer hemisphere, up to 10° in oceanic regions and occasionally as far as 30° in the case of the Asian summer monsoon (Yihui and Chan, 2005)[157].

The mechanisms that control the ITCZ remain unclear. Ideally, convergence occurs over the warmest surface waters. Indeed, in the northeast Pacific ocean, the ITCZ remains north of the equator throughout the entire year, coinciding largely with high sea surface temperatures (SSTs), which do not follow maximal insolation during northern winter (Janowiak et al., 1995)[158]. However, previous observations show that the ITCZ does not always coincide with the SST maximum and corresponding local sea level pressure minimum (Ramage, 1974; Sadler, 1975)[159, 160]. In light of such observations, and given the importance of moisture transport to tropical communities, considerable attention has been paid in the literature towards identifying and understanding controls on the ITCZ (Waliser and Somerville, 1994; Sobel and Neelin, 2006; Schneider et al., 2014)[161, 46, 50]. Most of this work can be roughly divided into two theories for understanding the ITCZ: one based on thermodynamics and

the other on momentum dynamics.

2.1.1 Thermodynamic theory

Thermodynamic theories posit that convergence and precipitation are determined by local vertical temperature and moisture profiles governed by the moisture budget and surface and radiative fluxes (Sobel and Neelin, 2006)[46]. When used in conjuction with the "weak temperature gradient" (WTG) approximation (Sobel et al., 2001)[162], some such theories successfully reconstruct tropical convergence and tend to predict maximum convergence and rainfall over the warmest surface temperatures (Neelin and Held, 1987; Raymond, 2000; Sobel and Bretherton, 2000)[47, 163, 164]. When applied to convergence zones associated with zonally averaged overturning circulations that conserve angular momentum (Lindzen and Hou, 1988)[165] and coupled to quasi-equilibrium theories of moist convection (Arakawa and Schubert, 1974; Emanuel et al., 1994; Nie et al., 2010)[166, 167, 168], such theories argue that the ITCZ, defined here and throughout this paper as the latitude of maximum zonal mean precipitation, lies just equatorward of the maximum low-level moist static energy (Emanuel, 1995; Privé and Plumb, 2007; Bordoni and Schnedier, 2008)[169, 48, 40].

However, the ITCZ has also been shown to respond strongly to extratropical thermal forcings, with shifts of the ITCZ into (away from) a relatively warmed (cooled) hemisphere, indicating that forcings remote from precipitation maxima can influence the tropical circulation and convergence zones (Chiang and Bitz, 2005; Broccoli et al., 2006)[170, 171]. The vertically integrated atmospheric energy budget has been invoked to explain ITCZ shifts in response to remote forcing and has led to the development of another diagnostic, the energy flux equator (EFE), which is the latitude at which the zonal mean moist static energy (MSE) meridional flux vanishes (Kang et al., 2008)[49]. In recent studies focused on global energy transports, the EFE has been shown to be well correlated with the ITCZ's poleward excursion into the summer hemisphere, and the energetic framework in general has proved useful for understanding the ITCZ and its migrations on different timescales (Kang et al., 2008; Kang et al., 2009; Chiang and Friedman, 2012; Frierson and

Hwang, 2012; Donohoe et al., 2013; Frierson et al., 2013; Bischoff and Schneider, 2014; Schneider et al., 2014; Adam et al., 2016; Bischoff and Schneider, 2016; Shekhar and Boos, 2016)[49, 172, 173, 174, 175, 176, 177, 50, 178, 179, 180].

2.1.2 Dynamic theory

Dynamic theories use the boundary layer momentum budget to determine winds and hence convergence, arguing that convection is driven primarily by boundary layer (BL) momentum dynamics (Lindzen and Nigam, 1987; Waliser and Somerville, 1994; Tomas and Webster, 1997; Pauluis, 2004)[181, 161, 182, 183]. Perhaps the most influential of these studies, Lindzen and Nigam (1987)[181] showed that the pressure gradients associated with even the small surface temperature gradients of the tropics have a substantial impact on low-level flow and convergence. Their model, built on tropical SST gradients, adequately reproduces the observed tropical convergence, though the model's assumptions have been debated. Back and Bretherton (2009)[184] address such concerns by testing and expanding upon Lindzen and Nigam (1987)[181], showing that SST gradients in reanalysis data are indeed consistent with BL convergence, which in turn causes deep convection. Along a similar vein, Tomas and Webster (1997)[182] found that in regions where the surface cross-equatorial sea level pressure gradient is weak, convection tends to coincide with the maximum SST, but in regions with a substantial cross-equatorial pressure gradient convection tends to lie equatorward of the maximum SST, also suggesting the importance of temperature *gradients*, as opposed to maxima, in driving the flow. Subsequent studies develop a theory to determine the location of the ITCZ based on the cross-equatorial pressure gradient, which drives anticyclonic vorticity advection across the equator to render the system inertially unstable (Tomas and Webster, 1997; Tomas et al., 1999; Toma and Webster, 2010)[182, 185, 186]. Thus, convergence and divergence are shown to be separated at the latitude where the zonal mean absolute vorticity is equal to zero. Additionally, the role of rotation in "forcing" the ITCZ towards the equator has been put forth by Chao (2000)[187] and Chao and Chen (2001)[188], wherein two "forces" critical to monsoon onset are described as in balance: one, associated with Earth's rotation, towards the equator, and the other towards the SST peak.

Classical axisymmetric theory for tropical circulation based on angular momentum conservation can also be classified as dynamical (Held and Hou, 1980)[37]. Though not predictive of the ITCZ location, these arguments do constrain the poleward extent of the Hadley cell to depend on planetary parameters such as rotation rate and radius. Studies have also highlighted the influence of eddy momentum fluxes on the Hadley circulation by studying wave-mean flow interactions (Pfeffer, 1981; Becker et al., 1997)[189, 190], the response of Earth's Hadley circulation to seasonal transitions (Walker and Schneider, 2005; Bordoni and Schneider, 2008; Schneider and Bordoni, 2008; Merlis et al., 2013)[191, 40, 41, 192], and the extent of the annual-mean Hadley circulation over a range of planetary parameters (Walker and Schneider, 2006; Levine and Schneider, 2011)[39, 193]. Indeed, it has been suggested that the annual-mean Hadley circulation width may be affected by extratropical baroclinic eddies that limit its poleward extent (Schneider, 2006; Levine and Schneider, 2015)[36, 42].

2.1.3 Generalizing theories of tropical circulation

In our above classification of theories, we acknowledge that neither group is exclusively either thermodynamical or dynamical. Convective quasi-equilibrium (CQE) theory, for example, is often used in conjunction with the WTG approximation in tropical circulation regimes. By this, it is assumed that gravity waves efficiently communicate convective heating throughout the domain, and thereby maintain a mean state with vanishingly small horizontal temperature gradients in the free troposphere. By this process, convection self-organizes to the maximum of low-level MSE and is suppressed elsewhere. Because of the WTG assumption, CQE theories of the ITCZ might actually be considered a hybrid of thermodynamics and dynamics. Furthermore, classical axisymmetric theory relies on energy conservation constraints to arrive at a scaling for the Hadley cell width, so it too may be considered a thermodynamic-dynamic hybrid.

Thus, CQE theory for the location of convergence is broadly connected, and in some ways analogous, to analytical dynamical theory based on angular momentum conservation and top-of-atmosphere (TOA) energy balance (Held and Hou, 1980; Lindzen and Hou, 1988;

Satoh, 1994; Caballero et al., 2008)[37, 165, 194, 195] as well as analytical thermodynamic theory for the location of an overturning circulation in a radiative-convective atmosphere based on a critical subcloud moist entropy curvature (Plumb and Hou, 1992; Emanuel, 1995)[196, 169]. These analytical theories predict the extent of the Hadley cell, which we note must be distinguished from the location of the ITCZ itself. Indeed, with foresight of our results, this distinction may be particularly important in the context of other terrestrial planets.

Regions of seasonal convergence and ascent associated with the Hadley cell analogous to Earth's ITCZ exist on other planetary bodies, namely Mars (Haberle et al., 1993; Lewis, 2003)[197, 198] and Titan, where the ascent region migrates significantly off the equator during summer solstice and nearly reaches the summer pole (Mitchell et al., 2006; Bouchez and Brown, 2005; Porco et al., 2005)[30, 18, 21]. Many parameter space studies using general circulation models (Williams, 1988; Navarra and Boccaletti, 2002; Walker and Schneider, 2006; Mitchell and Vallis, 2010; Mitchell et al., 2014; Pinto and Mitchell, 2014; Kaspi and Showman, 2015)[199, 200, 39, 201, 202, 203, 204] show that slowly rotating planets exhibit expanded Hadley cells and effectively become "all-tropics" planets similar in circulation structure to Titan (Mitchell et al., 2006)[30], consistent with classical axisymmetric theory that predicts expanding Hadley cell widths with decreasing rotation rate and/or radius (Held and Hou, 1980)[37].

But no parameter space studies have been done using a moist general circulation model (GCM) with a seasonal cycle. We claim such experiments deserve investigation since the large-scale circulation is known to be sensitive to the addition of a seasonal cycle, which induces a cross-equatorial circulation and upper-level easterlies in the tropics and can lead to seasonal shifts in the Hadley cell's dominant angular momentum budget (Bordoni and Schneider, 2008; Schneider and Bordoni, 2008)[40, 41]. Additionally, moisture greatly impacts the zonally averaged large-scale circulation due to the effects of latent heat on static stability and meridional temperature gradients (Frierson et al., 2006; Frierson, 2008)[152, 205]. We aim here to determine how sensitive the large-scale circulation is to slower rotation rates in the presence of moisture and a seasonal cycle. Furthermore, much of the work discussed above

is relevant for near-equatorial ITCZs, where the influence of rotation and free-tropospheric temperature gradients are generally weak, but it thus remains unclear how the ITCZ behaves at higher latitudes where these assumptions break down.

We examine potential controls on the ITCZ's movement using a moist Earth GCM of varying seasonal forcing and rotation rate. We evaluate previous predictors for the ITCZ—namely the maximum low-level MSE, Hadley cell extent, and EFE—as well as angular-momentum conserving theories of the Hadley cell's poleward extent, in a wide parameter space of rotation rates and seasonal forcing. In addition, we assess the interaction of BL dynamics with the large-scale circulation. As a result, our work evaluates both thermodynamic and dynamic arguments for the ITCZ's position in perpetually solstitial and slowly rotating seasonal large-scale circulations. In section 2.2, we describe the model and experimental setup. In section 2.3, we focus on the unique eternal solstice case at Earth's rotation rate and evaluate relevant CQE theories. In section 2.4, we analyze the general circulation of our rotation rate experiments. Then in section 2.5, we present analysis of the BL dynamics and radiative energy balance for all experiments.

2.2 Methods

We use the moist idealized three-dimensional GCM described in Frierson et al. (2006)[152] and Frierson (2007)[140] based on the Geophysical Fluid Dynamics Laboratory (GFDL) spectral dynamical core, but with two major changes: 1) the addition of a seasonal cycle, and 2) long-wave optical depths that do not depend on latitude.

Radiative heating and cooling are represented by gray radiative transfer, in which radiative fluxes are only a function of temperature, thus eliminating water vapor feedback. There is no diurnal cycle. The convection parameterization is a simplified Betts-Miller scheme, described fully in Frierson (2007)[140]. The scheme relaxes the temperature and moisture profiles of convectively unstable columns to a moist adiabat with a specified relative humidity (70% in these simulations) over a fixed relaxation time (2 hours). Standard drag laws are used to calculate surface fluxes, with drag coefficients determined by a simplified

Monin-Obukhov scheme. The BL scheme is a standard K-profile scheme with diffusivities consistent with the simplified Monin-Obukhov theory (see Chapter 1). The lower boundary is a zonally symmetric slab mixed layer ocean with a constant depth of 10 m in the control case, corresponding to a heat capacity C of 1 $\times 10^7$ J m^{-2} K^{-1} and a thermal inertia timescale τ_f $\sim$20 days, where $\tau_f = \frac{C}{4\sigma\overline{T}^3}$ and $\overline{T} = 285$ K (Mitchell et al., 2014)[202]. Thus, sea surface temperatures are prognostic and adjust to ensure the surface energy budget is closed in the time mean.

We implement the seasonally varying top-of-atmosphere (TOA) insolation prescription from Hartmann (1994)[206, pp. 347-349], wherein the declination angle is approximated by a Fourier series that provides an empirical fit to Earth's current insolation. The prescription accounts for Earth's eccentricity.

The latitude-dependent optical depth of the original model was suited for an equinoctial framework and is thus inappropriate for our seasonal framework where bands of precipitation and humidity fluctuate in latitude over the course of a year. In our model, the prescribed optical depth is independent of latitude, becoming a function only of pressure with a linear component, describing the effect of well-mixed greenhouse gases, and a quartic component, capturing the effect of water vapor confined to the lower troposphere. Parameters of the pressure-dependent optical depth are same as in Frierson et al. (2006)[152], except the surface value of optical depth $\tau_0 = \frac{1}{2}(\tau_{0e} + \tau_{0p})$, where τ_{0e} and τ_{0p} represent the equator and pole, respectively.

The model uses the primitive equations with T42 spectral resolution and 25 unevenly spaced vertical levels, with greater resolution in the BL. We conduct two primary sets of simulations: 1) we reduce the frequency of the seasonal cycle down to the extreme case where the planet is in eternal solstice, with all other parameters kept Earth-like (default parameters as in Frierson et al. (2006)[152]), done to observe ITCZ behavior over the longer timescales of fixed insolation; and 2) we adjust the rotation rate of an Earth-like planet from 4 times larger than Earth's value down to 32 times smaller than Earth's value, with all parameters other than rotation rate (insolation, radius, gravity, etc.) kept Earth-like and the insolation cycle kept fixed.

All simulations are run for ten years. Values for the eternal solstice simulation are averaged over the final year (nine years of spin-up). Values for the seasonal cases are composited over the last eight years (two years of spin-up). All solstitial time averages for each year of the seasonal cases are taken during a 40-day period centered around the time of maximum zonally-averaged northern hemisphere precipitation.

2.3 Evaluating thermodynamic mechanisms via the eternal solstice case

A thermodynamic theory for the location of the convergence zone is based on the assumptions of a moist adiabatic vertical thermodynamic profile in statistical equilibrium, i.e. CQE, and an angular momentum-conserving meridional circulation that constrains free-tropospheric temperature gradients to be weak. CQE thus connects upper tropopheric temperature to low-level MSE and, when coupled with dynamical circulation theory, argues that the maximum zonal mean precipitation should occur just equatorward of the latitude of maximum zonal mean subcloud MSE (Emanuel et al., 1994; Privé and Plumb, 2007)[167, 48]. The low-level, zonal mean MSE $[m] = c_p[T] + [\Phi] + L_v[q]$, where the brackets indicate zonal mean, is strongly correlated with surface temperature over a saturated surface, as in our aquaplanet simulations. Examining the ITCZ in the eternal solstice experiment provides further insight into the CQE argument by effectively eliminating energetic adjustment timescales that might otherwise conflate seasonal effects.

The top left panel of Fig. 2.1 shows the zonal mean precipitation for the eternal solstice case at Earth's rotation rate. Maximum zonal and time mean MSE in this case is located at the summer pole (Fig. 2.2, top panel; vertical green line). The ITCZ, though, remains at low latitudes. Indeed, the maximum zonal and time mean precipitation occurs at approximately the same latitude for both the seasonal and eternal solstice case, around 20–25°N. This is seemingly at odds with CQE arguments. However, the thermal stratification set by moist convection assumed by CQE can only be communicated effectively by gravity waves in the tropics, where WTG holds. At the pole in the eternal solstice case, WTG is not a good

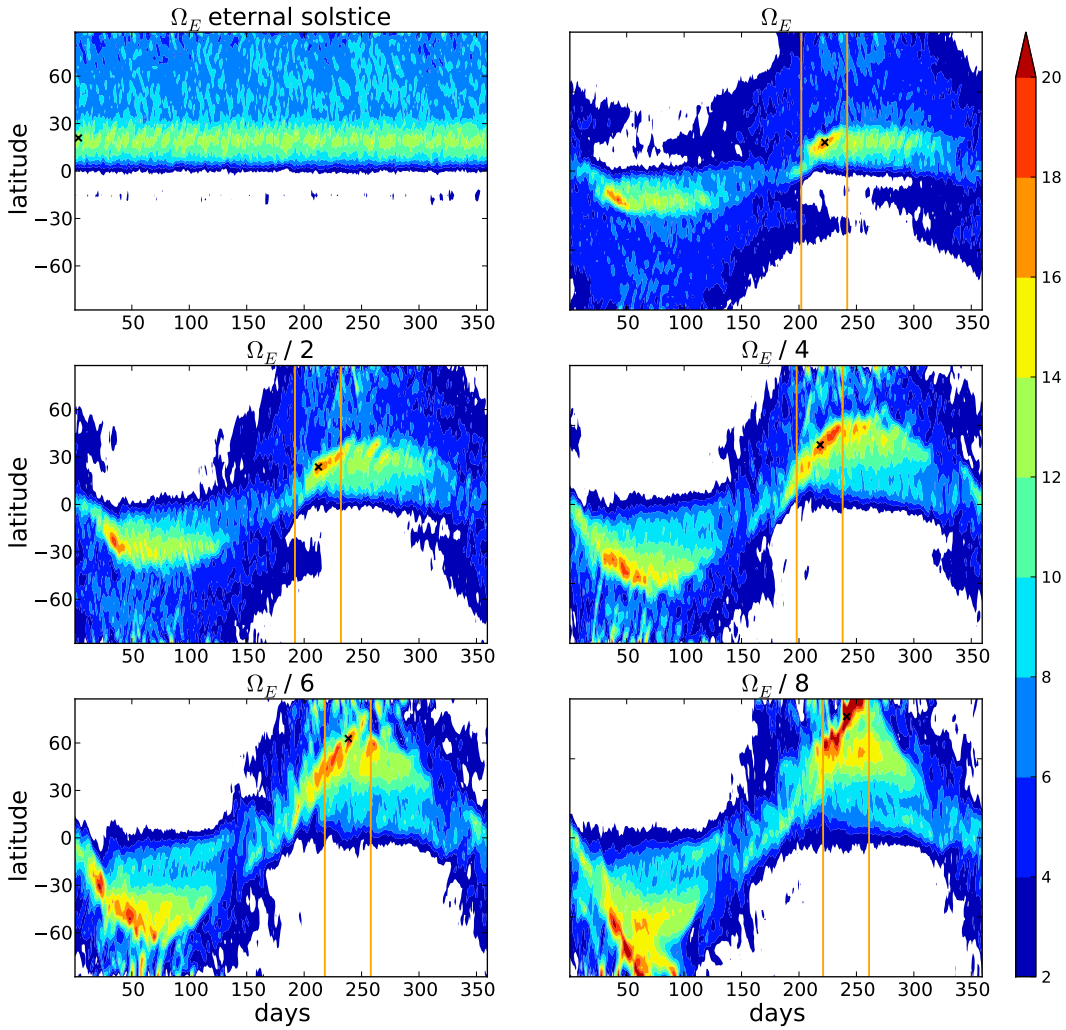

Figure 2.1: **Precipitation structure**. Zonal mean precipitation (mm/day) for all cases: the eternal solstice simulation and five seasonal cases of varying rotation rate. Orange vertical lines in the seasonal cases indicate time over which solstitial time averages are taken and represent the 40-day period between twenty days before the time of maximum zonal mean northern hemisphere precipitation (black cross) and twenty days after that time.

approximation and hence in this case, low-level MSE and the ITCZ can be greatly separated.

Alternatively, the latitudinal separation between a polar MSE maximum and a subtropical ITCZ may be understood through the theory of Emanuel (1995)[169], which, extending the arguments of Plumb and Hou (1992)[196] to a moist convective atmosphere, states that a cross-equatorial Hadley circulation needs to exist (in place of a radiative equilibrium response) when the curvature of the subcloud moist entropy exceeds a critical value. To test the criticality condition, we run a radiative-convective eternal solstice simulation at Earth's rotation rate and calculate the critical curvature as in Eq. 10 of Emanuel (1995)[169]. In the top panel of Fig. 2.2, we show both sides of this equation: the subcloud moist entropy curvature of the radiative-convective simulation (solid line) and the critical curvature (dotted line) for Earth's rotation rate. Fig. 2.2 clearly shows that a circulation is necessary equatorward of their intersection at $\sim$20°.

Thus, importantly, the critical condition is consistent with the existence of a low-latitude circulation in our (dynamically equilibrated) eternal solstice case, despite zonal mean MSE maximizing at the pole (Fig. 2.2, top panel; vertical green line). The ITCZ of the dynamically equilibrated eternal solstice simulation (Fig. 2.2, top panel; vertical blue line) occurs just equatorward of the intersection given by the radiative-convective critical condition, consistent with the above arguments. Additionally, the subcloud moist entropy curvature of the dynamically equilibrated state (Fig. 2.2, top panel; dashed line) largely overlaps that of the radiative-convective case in the subcritical extratropics, while the latitude at which it meets the critical condition is $\sim 10^\circ$ equatorward of that for the radiative-convective case. To demonstrate the similarities between these arguments and the angular momentum conserving arguments of Held and Hou (1980)[37], we include the TOA energy balance for the eternal solstice case in the bottom panels of Fig. 2.2, which we will return to in section 2.5.1.

For varying rotation rates, regions where entropy gradients are supercritical extend farther poleward as rotation rate decreases; as shown in section 2.4, the corresponding Hadley circulations however expand to an even greater degree. Using critical curvatures calculated from the moist entropy distributions of the simulations themselves yields slightly better predictions of the circulation extent, but the results are complicated by two factors: 1) the

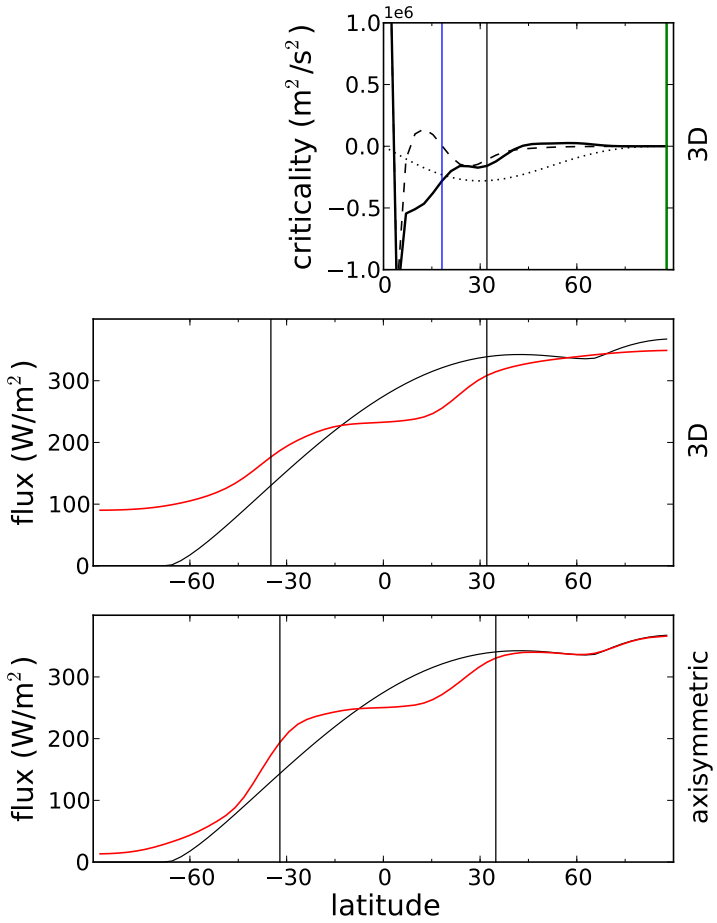

Figure 2.2: **Assessing the critical condition for subtropical convection**. Top) Critical condition as from Emanuel (1995)[169]. Solid line gives the curvature calculated from the subcloud moist entropy distribution of the radiative-convective eternal solstice experiment according to $\frac{\partial}{\partial\phi}[\frac{cos^3\phi}{sin\phi}(T_s - T_t)\frac{\partial s_b}{\partial\phi}]$, where s_b is the moist entropy taken at $\sigma = 0.85$ and T_t is the temperature at $\sigma = 0.20$. Dashed line gives the curvature calculated from the equilibrated subcloud moist entropy distribution of the eternal solstice simulation at Earth's rotation rate. The dotted line gives the critical curvature, $-4\Omega^2 a^2 cos^3\phi sin\phi$. Vertical blue line and green line represent latitude of maximum $\overline{[P]}$ and latitude of maximum $\overline{[MSE]}$ in the equilibrated eternal solstice simulation, respectively. Vertical black lines indicate northern and southern extents of winter Hadley cell of the equilibrated eternal solstice simulation, where Hadley cell extent is defined as the latitude where the streamfunction, taken at the pressure level of its maximum value, reaches 2% of that maximum value. Middle, Bottom) Insolation (black) and zonal and time mean OLR (red) for the equilibrated eternal solstice simulation (middle) and an axisymmetric eternal solstice simulation (bottom), both at Earth's rotation rate. Vertical black lines are Hadley cell extents as defined in top panel.

circulation reconfigures the subcloud moist entropy distribution significantly from the conditions assumed in deriving the criticality; and 2) the criticality condition predicts the presence or absence of a circulation and thus is a predictor of the Hadley cell extent, rather than the ITCZ. Hence, this criticality argument cannot be easily translated into either a predictor or a quantitative diagnostic of the ITCZ position for our simulations. Despite these limitations, further exploration of the critical curvature condition as applied to the ITCZ of varying climates seems a worthwhile avenue for future work.

The eternal solstice simulation at Earth's rotation rate also addresses the impact of heat capacity, which has been shown to affect the ITCZ's movement (Fein and Stephens, 1987; Xie, 2004; Pierrehumbert, 2005; Bordoni and Schneider, 2008; Abbot and Pierrehumbert, 2010; Donohoe et al., 2014)[207, 208, 209, 40, 210, 211]. Maximum insolation in the eternal solstice case is fixed at the pole for ten years, much longer than the timescale for atmospheric adjustments, and still the precipitation maximum lies at low latitudes. Thus, it appears that reducing the timescale for atmospheric adjustments even further would not have any impact on the ITCZ migration. Indeed, we run simulations of varying *surface* heat capacities and find that there is little change in the position of the ITCZ as the heat capacity is decreased beyond the control (not shown). In addition, a lack of baroclinic activity in the extratropics of the eternal solstice case suggests baroclinic instability, through influences on the summer Hadley cell, plays no role in limiting the ITCZ's poleward migration during solstice in our simulations (confirmed by axisymmetric runs).

The subtropical ITCZ in the eternal solstice case, when combined with results that atmospheric and lower-boundary thermal inertia cannot push an ITCZ to the pole, suggests that planetary parameters must be important for ITCZ migrations in other planetary settings such as Mars and Titan. We therefore explore the influence of decreasing rotation rate in the next section.

2.4 Rotation rate experiments

Here we run Earth-like simulations for varying rotation rates to explore the conditions under which the ITCZ can seasonally migrate poleward. This is roughly equivalent to varying radius since both parameters similarly impact Hadley cell width (Held and Hou, 1980)[37]. From Fig. 2.1, the ITCZ moves farther off the equator towards the summer pole with each decrease in rotation rate, consistent with the expanding annual-mean Hadley cell for slower rotation rates found in previous studies. We run simulations with rotation rates down to 32 times smaller than Earth's, but they are not shown because their circulations are similar in structure to that of the $\Omega/\Omega_E = \frac{1}{8}$ case. Similarly, the $\Omega/\Omega_E = 2$ and $\Omega/\Omega_E = 4$ cases are not shown due to their circulation structures largely resembling that of the control case, though their ITCZs are indeed closer to the equator than the control (see Fig. 2.5).

For $\Omega/\Omega_E \leq \frac{1}{8}$, the planet enters a regime where the winter Hadley cell becomes global, precluding any significantly farther migration with larger decreases in rotation. Note that local maxima in MSE exist at the pole during solstice in all cases (not shown), consistent with the small "patches" of polar precipitation separated from the main ITCZ band in the quickly rotating cases. Indeed for $\Omega/\Omega_E \leq \frac{1}{8}$, a transient maximum in zonal mean precipitation exists at the summer pole (Fig. 2.1). This polar maximum is however separate from the ITCZ, which is the precipitation maximum at lower latitudes associated with the region of strongest convergence in the ascending branch of the Hadley cell ($\sim$60°N in the $\Omega/\Omega_E = \frac{1}{8}$ case).

The right columns of Fig. 2.3 and Fig. 2.4 show the zonally averaged meridional circulation and angular momentum contours during solstice for all rotation cases. Consistent with the precipitation, the cross-equatorial Hadley cell expands farther poleward for each decrease in rotation rate. Additionally, the summer cell is negligible when compared to the cross-equatorial winter cell for all simulations during the averaged solstitial time period. The right columns of Fig. 2.3 and Fig. 2.4 also show zonal mean precipitation averaged over the solstitial time period, demonstrating the association between the ITCZ and the Hadley cell structure. In aquaplanet simulations of Earth with negligible surface thermal inertia,

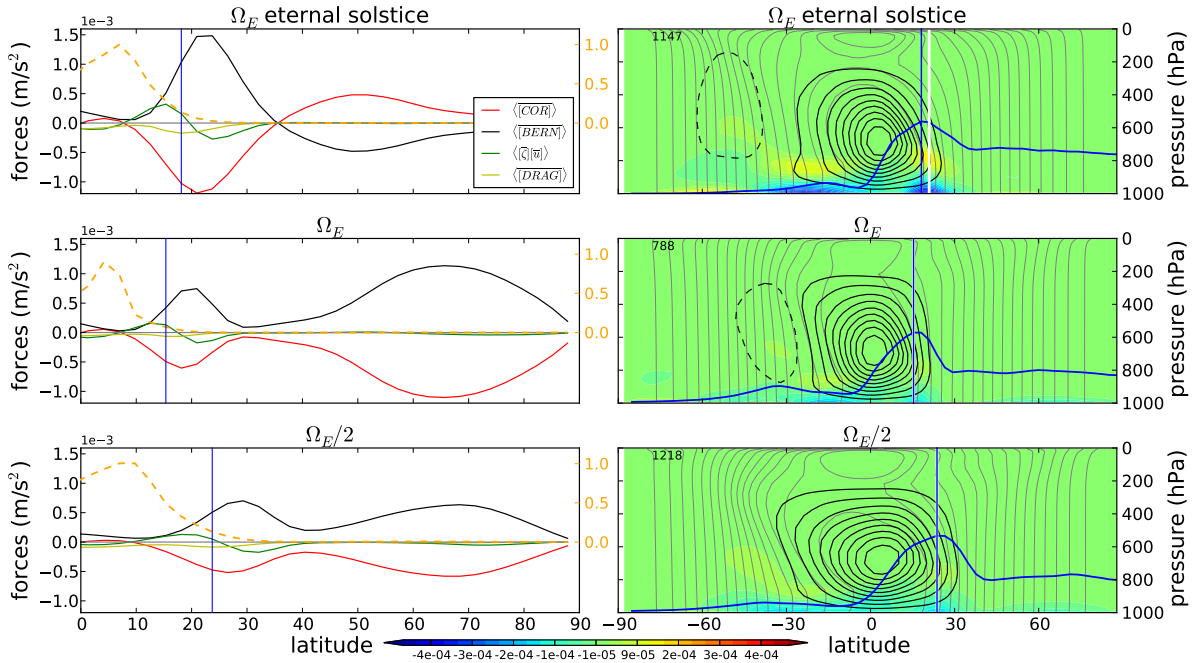

Figure 2.3: **Circulation and boundary layer structures for quickly rotating cases**. Left) Summer hemisphere forces on left y-axis, with positive values denoting a northward force and where $BERN$, COR, and $DRAG$ correspond to the Bernoulli gradient, Coriolis, and frictional forces. Each force is diagnosed directly from simulation. Values of G, from Schneider and Bordoni (2008)[41], are on right y-axis. Vertical blue line represents the latitude of maximum $\overline{[P]}$. Vertical integration taken from the surface to $\sigma = 0.85$. Solstitial time averages taken over period shown in Fig. 2.1. Right) Zonally and solstitially averaged streamfunction, angular momentum, drag, and precipitation. Streamfunction contours (black, solid lines counter-clockwise) are 10% of maximum, printed in top left corner in 10^9 kg/s. Grey contours are angular momentum contours ($\Omega a^2/17$ interval). Drag force (color contours) in m/s^2. Precipitation $\overline{[P]}$ in blue, units not shown. Solstitial time averages taken over period shown in Fig. 2.1. Vertical white line represents latitude of maximum vertically integrated BL drag force. Vertical blue line represents latitude of maximum $\overline{[P]}$ as in left column.

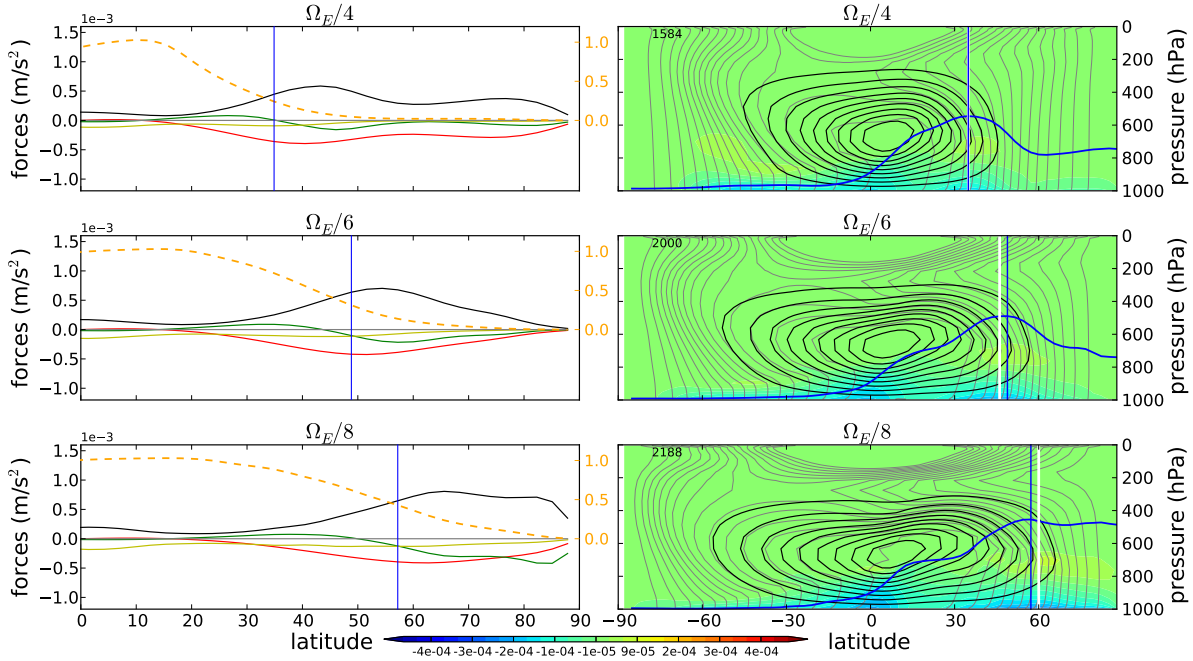

Figure 2.4: **Circulation and boundary layer structures for slowly rotating cases**. Same as Fig. 2.3, but for more slowly rotating cases.

as the seasonal cycle transitions from equinox to solstice—representing monsoon onset over land-dominated regions such as the Asian monsoon region—the winter Hadley cell strengthens and its ascending upper branch becomes more angular momentum-conserving (center row in Fig. 2.3), echoing previous studies (Lindzen and Hou, 1988; Bordoni and Schneider, 2008; Schneider and Bordoni, 2008)[165, 40, 41]. At solstice, upper-level easterlies shield the circulation from energy-containing midlatitude eddies and the eddy momentum flux divergence is weak, thus allowing streamlines to follow angular momentum contours in most of the upper branch of the cross-equatorial winter cell. We observe similar solstitial dynamics as the rotation rate is decreased in our simulations: streamlines in the ascending region of all cases generally follow angular momentum contours; and in all cases a region of upper-level easterlies (not shown) is maintained by the winter circulation, which continues to expand latitudinally with decreasing rotation rate down to $\Omega/\Omega_E = \frac{1}{8}$, where the circulation finally becomes global.

Thus, a regime change occurs after $\Omega/\Omega_E = \frac{1}{8}$, wherein three conditions hold for planets with that rotation rate and slower: 1) the winter cross-equatorial cell extends from pole to pole and has a latitudinally wide region of updraft as opposed to the meridionally narrow

ascent region seen in the more quickly rotating cases, 2) eddy momentum flux divergence is weak at all latitudes, and 3) the ITCZ does not move past ∼60-70° (Fig. 2.4, bottom right panel; vertical blue line) despite the circulation becoming global, though a shorter-lived precipitation maximum is observed at the summer pole. A similar regime change was noted in the non-seasonal experiments of Walker and Schneider (2006)[39], wherein the upper branches of the circulations for slowly rotating planets were nearly angular momentum-conserving around the latitude of the Hadley streamfunction extremum.

2.4.1 Predictors for the ITCZ

Here we evaluate relevant predictors for the ITCZ, namely the Hadley cell extent, the maximum low-level MSE, and the EFE. As in the previous section, the zonally averaged low-level MSE $\overline{[m]}$ is taken at 850 hPa, with the overbar denoting solstitial average. The Hadley cell extent ϕ_H is defined as the latitude where the cross-equatorial streamfunction, taken at the pressure level of its maximum value, reaches 5% of that maximum value in the summer hemisphere (Walker and Schneider, 2006)[39]. Finally, the EFE defined in Kang et al. (2008)[49] as where the energy flux $F = \langle\overline{[mv]}\rangle$ reaches zero, with the angled brackets denoting vertical integration. However, since F doesn't vanish until the pole for $\Omega/\Omega_E = \frac{1}{2}$ and slower during solstice, here we define the EFE as the latitude where the flux F reaches 5% of its maximum value, similar to the Hadley cell extent definition. Fig. 2.5 shows these predictors, each normalized to the maximum zonally and solstitially averaged precipitation (the ITCZ), for all rotation cases. It also shows the latitude where the function $G = 0.5$, with G defined in Schneider and Bordoni (2008)[41]. We return to this predictor in section 2.5.2.

The MSE maximum, Hadley cell extent, and EFE occur poleward of the latitude of the ITCZ for all cases. These three values are generally well correlated (particularly at faster rotation rates). Indeed, the Hadley cell extent and EFE, physically related to one another (and, by definition, nearly equivalent), are approximately collocated for each rotation rate. It is also clear from Fig. 2.5 that the ITCZ is associated with the ascending branch of the cross-equatorial winter Hadley cell but generally lies equatorward of its edge. However,

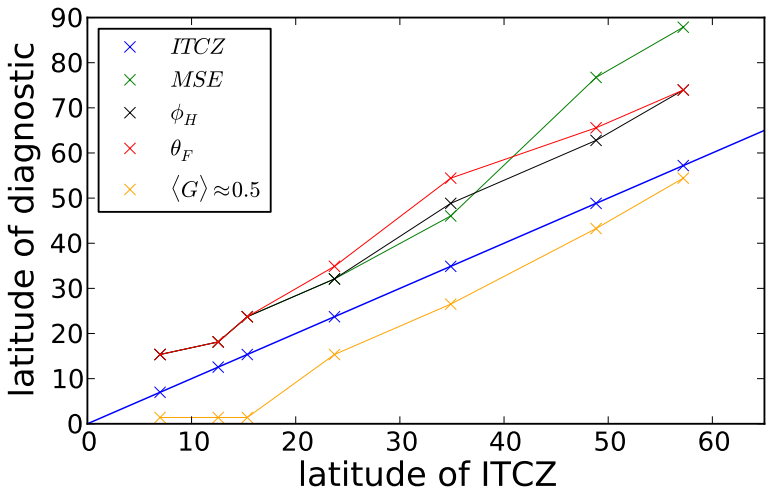

Figure 2.5: **ITCZ diagnostics**. Zonal and time mean maximum low-level MSE (green), Hadley cell extent (black), EFE (red), and latitude where $\langle G \rangle \approx 0.5$ (orange) as compared to the ITCZ (blue) for different rotation cases. Blue line is 1:1. From left to right, rotation rates Ω/Ω_E are: 4, 2, 1, $\frac{1}{2}$, $\frac{1}{4}$, $\frac{1}{6}$, $\frac{1}{8}$.

the distance of separation between the ITCZ and the winter Hadley cell extent appears to *increase* with decreasing rotation rate. Once the circulation enters the slowly rotating regime, the ITCZ remains approximately at ∼60° while the Hadley cell extent remains at ∼75-80°. We also note the larger discrepancy between the latitude of maximum MSE and the Hadley cell extent in the $\Omega/\Omega_E = \frac{1}{6}$ and $\Omega/\Omega_E = \frac{1}{8}$ cases. This is consistent with the transient polar convection being separated from the large-scale circulation in these cases—a feature also observed in GCM models of Titan's atmosphere (Mitchell and Lora, 2016)[38].

That the maximum precipitation is slightly equatorward of the maximum MSE during solstice on Earth has been noted in theory, models, and observations (Privé and Plumb, 2007; Bordoni and Schneider, 2008)[48, 40]. Small discrepancies between the EFE and the ITCZ in Earth settings have also been observed in idealized models and reanalysis data (Kang et al., 2008; Bischoff and Schneider, 2014; Bischoff and Schneider, 2016; Adam et al., 2016)[49, 177, 179, 178], emphasizing the need for a comprehensive theory of the ITCZ position that couples considerations of both the energy balance and the angular momentum balance, particularly in strongly off-equatorial regimes. In the next section, we work towards developing an understanding of the position of the ITCZ based on BL dynamics and TOA energy balance.

2.5 Evaluating dynamical mechanisms

The flow that leads to the ITCZ is part of the lower branch of the cross-equatorial winter Hadley cell. Using the case of northern summer solstice as an example, this flow is the northward BL flow between the equator and the northern edge of the winter cell in the summer hemisphere. The edge of the winter cell itself is where the flow vanishes, at a latitude analogous to the EFE or the maximum MSE, and can be determined by TOA energy balance (Held and Hou, 1980; Lindzen and Hou, 1988; Satoh, 1994; Caballero et al., 2008)[37, 165, 194, 195]. Meridional forces in the BL, primarily the northward pressure gradient force and southward Coriolis force, govern the zonal mean flow. However, while eddy momentum flux divergence and vertical advection are very small in the BL, nonlinear advective forces are not and so the flow is not completely in geostrophic balance. The pressure gradient, Coriolis, and nonlinear forces combine into a northward force that balances the southward drag. Since the flow must vanish farther poleward at the Hadley cell edge—and indeed all the forces must vanish there, except for in the slowly rotating regime where they cannot vanish before reaching the pole—there is a flow transition that must occur that leads to the ITCZ. Our simulations demonstrate this mechanism and also provide a scaling for the latitude of the ITCZ's poleward excursion with rotation rate.

2.5.1 TOA energy balance

The mechanism behind the ITCZ, as it appears from our simulations, is intimately tied to previous work done by Held and Hou (1980)[37] and in particular by Caballero et al. (2008)[195], who applied the energy balance arguments of Held and Hou (1980)[37] to the solstitial circulation in order to determine the extent of the cross-equatorial winter Hadley cell into the summer hemisphere. The simulated cross-equatorial circulations for all rotation rates approach the angular momentum-conserving solution, in which the potential temperature in the free troposphere adjusts through thermal wind balance to the angular momentum-conserving winds. Together with energy conservation constraints, i.e. the energy budget is closed within the Hadley cell and there is temperature continuity with the radiative-

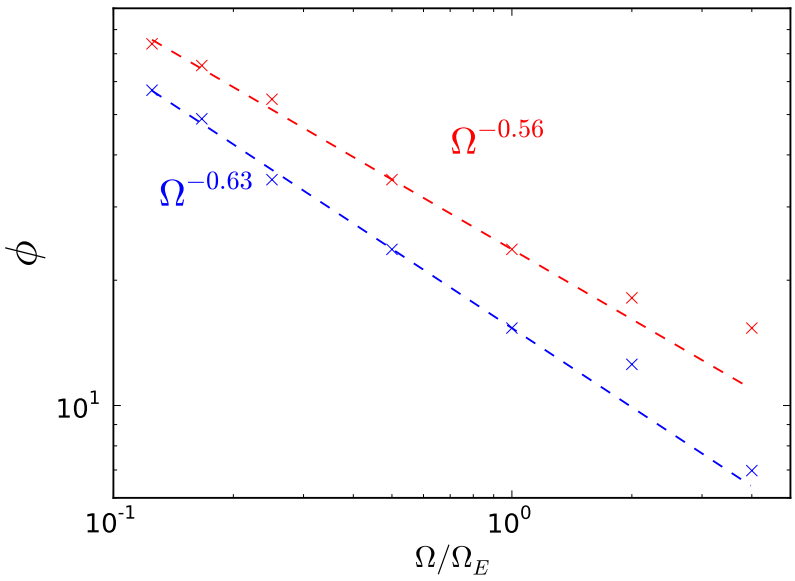

Figure 2.6: **Scalings with rotation rate**. Rotation rate versus latitudes of ITCZ (blue) and EFE (red). Dashed lines represent scaling fits to cases with rotation rate $\Omega/\Omega_E = \frac{1}{8}$ and greater (including $\Omega/\Omega_E = 2$ and $\Omega/\Omega_E = 4$) for both values (color corresponds to color of crosses).

convective equilibrium profile at the cell's poleward boundary, these angular momentum-conserving arguments can be used to determine the latitude of the ascending branch of the winter Hadley cell, corresponding to where the energy flux and boundary layer forces vanish just poleward of the ITCZ position, as described above.

Held and Hou (1980)[37] find the Hadley cell extent to be dependent on the thermal Rossby number such that $\phi_H \propto (Ro)^{1/2}$ for $Ro = \frac{gH\Delta_H}{\Omega^2 a^2}$, where H is the tropopause height and Δ_H is the pole-to-equator radiative-convective equilibrium temperature difference. Caballero et al. (2008)[195] applied similar arguments to seasonal insolation and found that the solstitial Hadley cell extent followed a different power law: $\phi_H \propto (Ro)^{1/3}$. Fig. 2.6 shows the scalings of the ITCZ and the EFE with rotation rate. Cases slower than $\Omega/\Omega_E = \frac{1}{8}$ were not included in the scaling because the ITCZ's progression with rotation rate is limited by the pole beyond that point, i.e. once the Hadley cell is global, it remains so for slower rotation rates.

Since Ro scales as Ω^{-2}, the solstitial Hadley extent as determined by Caballero et al. (2008)[195] scales as $\Omega^{-2/3}$, and Fig. 2.6 shows a similar scaling in our simulations—both for the energy flux equator and the latitude of the ITCZ itself—despite the fact that Caballero

et al. (2008)[195] used dry axisymmetric theory. This may be associated with the dynamic characteristics of solstice in an aquaplanet simulation: during solstice, the upper branch of the winter Hadley cell is approximately angular momentum-conserving at the latitude of ascent, with local Rossby numbers $Ro \geq 0.6$, signifying the relatively weak impact of eddy momentum flux divergence (Bordoni and Schneider, 2008; Schneider and Bordoni, 2008)[40, 41], thereby approximating axisymmetric conditions. As a caveat to the similarities just described, we should note that the power laws of Held and Hou (1980)[37] and Caballero et al. (2008)[195] employ the small-angle approximation, which is most likely inappropriate for our most slowly rotating cases.

TOA energy balance further illuminates the low-latitude ascent in the eternal solstice case despite temperatures maximizing in that simulation at the pole. Aforementioned energy conservation constraints argue for the Hadley cell edge to coincide with the intersection of the insolation profile and zonal mean outgoing longwave radiation (OLR). The zonal mean OLR, SST, and low-level MSE all exhibit approximately the same meridional profile in our eternal solstice simulation, maximizing at the pole, but the OLR intersects with the insolation at a latitude just less than $\sim 60^\circ$ (see Fig. 2.2, middle panel). Note from the bottom panel of Fig. 2.2 that we additionally run an axisymmetric eternal solstice case, which gives a slightly better estimate of the winter Hadley cell extent using TOA energy balance arguments given the absence of baroclinic eddies that diverge energy out of the subtropics.

The above arguments, however, apply specifically to the Hadley cell extent rather than the ITCZ. The latitudinal separation between the ITCZ and predictors related to the Hadley cell, which can be quite large in some of our rotation rate experiments, suggests the importance of the BL momentum budget, since precipitation is collocated with lower-level convergence and BL forces drive lower-level flow.

2.5.2 Boundary layer dynamics

Following Schneider and Bordoni (2008)[41], the BL steady-state momentum equations with drag represented as Rayleigh drag with damping coefficient ϵ are:

$$-(f+\overline{\zeta})\overline{v} \approx -\epsilon\overline{u} \tag{2.1}$$

$$(f+\overline{\zeta})\overline{u} + \frac{\partial \overline{B}}{\partial y} \approx -\epsilon\overline{v} \tag{2.2}$$

where $\overline{B} = \overline{\Phi} + (\overline{u}^2 + \overline{v}^2)/2$ is the mean barotropic Bernoulli function with geopotential Φ and the overbar again denotes the time mean. Formulating the momentum equation this way means that the Bernoulli gradient accounts for the pressure gradient force as well as nonlinear contributions unaccounted for by the $\overline{\zeta}\overline{u}$ term. Aside from approximating turbulent drag as Rayleigh drag, the other assumptions made here are that contributions from eddy momentum flux divergence and vertical advection are negligible, and indeed in our simulations those terms are about an order of magnitude smaller than the retained Coriolis, Bernoulli gradient, drag, and $\overline{\zeta}\overline{u}$ terms (We include the Rayleigh drag approximation here because it is used in the calculation of G later in this section, but the drag force plotted in Fig. 2.3 and Fig. 2.4 is diagnosed directly from the model, calculated by horizontal diffusion).

Fig. 2.3 and Fig. 2.4 give a summary of these forces for each rotation case during northern summer solstice and the eternal solstice case, with all values vertically integrated over the BL. We define the BL as ending at 850 hPa, though note that for the more slowly rotating cases, the lower branch of the circulation reaches the free troposphere. For all cases, the ITCZ is well correlated with the latitude of maximum BL drag. Indeed, in the eternal solstice case, where CQE arguments relating the ITCZ to maximum MSE appear inapplicable, the ITCZ and latitude of maximum drag are exactly collocated. From the right column of Fig. 2.3 and Fig. 2.4, it is evident that for each case the ITCZ is located in the BL region of maximum southward drag, a region just equatorward of the edge of the winter Hadley cell.

As rotation slows and the convergence zone widens, the convergence zone force balance changes from primarily geostrophic balance to something closer to cyclostrophic balance, with the nonlinear $\overline{\zeta}\overline{u}$ force becoming a dominant contributor to balancing the Bernoulli gradient force. Also in the slowly rotating cases, regions of strong meridional drag exist at equatorial latitudes. Corresponding secondary maxima of precipitation (see Fig. 2.3 and Fig.

2.4) and vertical velocity (not shown) occur in these regions, but they are located ∼10-15° downstream of the maximum drag. Pauluis (2004)[183] describes the dynamics of a similar secondary precipitation maximum near the equator in axisymmetric cross-equatorial Hadley circulations. The downstream displacement of this secondary precipitation maximum in our simulations (∼10-15°N) relative to that seen in the axisymmetric simulations of Pauluis (2004)[183] might be indicative of the increasing role of nonlinear terms in the BL momentum budget as rotation rate is decreased.

The left columns of Fig. 2.3 and Fig. 2.4 show that the same approximate force balance holds for each case. Convergence occurs as the flow transitions from a BL balance primarily between the Bernoulli gradient force and friction to a BL balance primarily between the Bernoulli gradient force and the Coriolis force, a transition zone previously defined and described in Schneider and Bordoni (2008)[41] via the nondimensional function $G = \frac{\epsilon^2}{\epsilon^2+(f+\overline{[\zeta]})^2}$ (Fig. 2.3 and Fig. 2.4, left column; dashed orange line). We calculate G using $\epsilon = C_d(\overline{[u]}^2 + \overline{[v]}^2)^{1/2}/H_0$, with C_d being the surface drag coefficient of momentum and H_0 being the height of the BL (Lindzen and Nigam, 1987)[181]. Schneider and Bordoni (2008)[41] approximate the ITCZ as the region where $G \approx 0.5$, a descriptor that is not collocated but still correlated with the ITCZ in our simulations (see Fig. 2.5). The transition zone occurs over a larger latitudinal range as rotation rate decreases, consistent with the widening winter Hadley cell and more extensive regions of convergence and precipitation in those cases. Where the Bernoulli gradient force and friction are balanced equatorward of the ITCZ, the zonal and time mean absolute vorticity $\overline{[\eta]}$ is approximately zero in every case (not shown). This is consistent with the work of Tomas and Webster (1997)[182], in which the $\overline{[\eta]} = 0$ latitude demarcates between divergence and convergence, with divergence equatorward of that latitude and convergence associated with inertial instability—producing the ITCZ—poleward of that latitude.

It is also apparent from the left column of Fig. 2.3 and Fig. 2.4 that the ITCZ is associated with the maximum northward Bernoulli gradient force, consistent with the ITCZ being well correlated with the maximum MSE gradient in all cases (not shown) given that temperature gradients determine pressure gradients, which have been argued to drive the con-

vergence zone low-level flow (Lindzen and Nigam, 1987; Tomas and Webster, 1997; Pauluis, 2004; Back and Bretherton, 2009)[181, 182, 183, 184]. However, due to the increasing relevance of nonlinear advective forces (namely the $\overline{\zeta}\overline{u}$ force) as the ITCZ moves farther from the equator in the more slowly rotating cases, the linear theories of Lindzen and Nigam (1987)[181] and Back and Bretherton (2009)[184] cannot be applied here, as they predict an ITCZ too far poleward in all but our control simulation. Indeed, the significance of the $\overline{\zeta}\overline{u}$ force implies that classic Ekman theory arguments describing flow—wherein the balance of forces is primarily between the pressure gradient force, the Coriolis force, and turbulent drag—are inappropriate when considering solstitial convergence zone dynamics. According to Ekman theory, uplift maximizes where geostrophic vorticity maximizes, but in every one of our simulations geostrophic vorticity maximizes well poleward of the ITCZ during solstice (not shown), underlining the unsuitability of Ekman theory in solstitial situations and the importance of nonlinearity in determining the BL maximum convergence—a relationship also noted by Tomas et al. (1999)[185].

2.6 Summary and conclusions

We conduct a suite of experiments to test various controls on the seasonal excursions of the ITCZ using an idealized, aquaplanet Earth GCM. We slow down the rotation rate of an otherwise Earth-like planet to examine the ITCZ as it migrates farther off the equator, and we additionally run an eternal solstice experiment. Our noteworthy conclusions from these experiments are:

- Classic ITCZ predictors, namely maximum MSE, Hadley cell extent, and EFE, are generally collocated with each other, but robustly lie poleward of the latitude of the ITCZ in our simulations, with the distance of separation *increasing* as the ITCZ moves farther from the equator. TOA energy balance, based on the axisymmetric theory of Held and Hou (1980)[37], determines the latitude of these predictors, i.e. the latitude poleward of the ITCZ where the flow vanishes.

- The ITCZ is closely associated with maximum BL drag and Bernoulli gradient. Other precipitation maxima are correlated with regions of significant BL drag and Bernoulli gradient as well, including the transient precipitation maximum that appears at the summer pole for rotation rates $\Omega/\Omega_E \leq \frac{1}{8}$. This maximum, however, is distinct from the ITCZ associated with the ascending branch of the Hadley circulation.

- The scalings of the ITCZ and EFE with rotation rate in our experiments are in good agreement with the dry axisymmetric $\Omega^{-2/3}$ scaling developed by Caballero et al. (2008)[195].

- The eternal solstice experiment demonstrates that the ITCZ is not always closely coupled with maximum zonal mean MSE. This can occur because at Earth's rotation rate temperature gradients are constrained to be small only at lower latitudes and can instead be balanced through thermal wind at high latitudes. In this respect, while some convection can occur in the region of maximal MSE at the pole, the thermal stratification set by convection cannot be communicated elsewhere and cannot lead to a supercritical high-latitude MSE distribution.

Based on the ITCZ's behavior across a range of rotation rates and seasonal forcings, the conclusions above present a framework for understanding the location of the ITCZ based on energy balance and BL dynamics. Future work is necessary to fully expose the details of the underlying dynamics at play and develop a comprehensive theory for the ITCZ location.

Such relationships are important when thinking about analogous systems of seasonal convergence on other planets. Our results suggest that it is perhaps planetary parameters associated with the angular momentum budget, i.e. the rotation rate and/or radius, that are primarily responsible for Titan's and Mars's far-reaching convergence zones, rather than their low surface heat capacities, for instance. Indeed, the atmospheric circulations of the $\Omega/\Omega_E = \frac{1}{8}$ case and slower, which have intense polar precipitation and a global Hadley cell, are not too dissimilar from that of Titan, which itself has a rotation rate approximately one sixteenth of Earth's and a radius one third of Earth's. While we are not yet able to predict the poleward migration of the ITCZ given only planetary parameters, the axisymmetric scaling

of Caballero et al. (2008)[195] seems to be quite accurate when applied to our simulations, even though they are moist and eddy-permitting. It is left for future work to further develop our diagnostic ITCZ understanding into a more prognostic theory that can be applied to any terrestrial planet with seasonally migrating convergence zones.

CHAPTER 3

Climatic Control of Geomorphic Features on Titan

The following is adapted from Faulk et al. (2017b)[155], now in press.

3.1 Introduction

Latitudinal variations in geomorphic features observed on Titan—from extensive fluvial features at all latitudes (Lorenz et al., 2008a; Langhans et al., 2012; Burr et al., 2013a)[76, 80, 81], to dissected and mottled terrain in the low and mid-latitudes (Moore et al., 2014)[120], alluvial fans concentrated in the mid- to high latitudes (Birch et al., 2016; Radebaugh et al., 2016; Cartwright and Burr, 2017)[82, 83, 84], and lake districts (Hayes, 2016)[52] and a relative lack of craters near the pole (Wood et al., 2010; Neish and Lorenz, 2014; Neish et al., 2016)[86, 90, 91]—suggest corresponding variations in climate, tectonics, or lithology. Given the relatively poorly characterized tectonic and lithologic environments on Titan, the established role of climate in shaping planetary surfaces (Moore and Howard, 2005; Ferrier et al., 2013; Perron, 2017)[117, 106, 101], and the abundant evidence for mechanical erosion and sediment transport by methane precipitation and fluid flow on Titan's surface (Burr et al., 2006; Perron et al., 2006; Jaumann et al., 2008; Litwin et al., 2012; Black et al., 2012)[96, 92, 93, 97, 94], we focus here on climatic controls, namely regionally-varying precipitation patterns that can shed light on localized erosion rates (Perron et al., 2006; Jaumann et al., 2008; Black et al., 2012)[92, 93, 94]. Precipitation and resulting discharge variability are important for shaping terrestrial geomorphology since rare but high-magnitude precipitation events initiate flash floods and debris flows that generally erode more efficiently than persistent low-magnitude precipitation and leave geomorphic signatures in the form of fans

(Blair and McPherson, 1994; Leier et al., 2005; Molnar et al., 2006; Dibiase and Whipple, 2011; Borga et al., 2014; D'Arcy et al., 2017)[107, 125, 104, 105, 108, 110]. Terrestrial fluvial megafans for instance have been linked to seasonal discharges and are most prevalent in latitudinal belts that fringe tropical climate zones, suggesting the influence of climatic patterns on alluvial fan formation (Leier et al., 2005; Gibling et al., 2005)[125, 126]. Titan's rare rainstorms have been hypothesized to be violent based on thermodynamics and convection models (Lorenz et al., 2005; Barth and Rafkin, 2010; Rafkin and Barth, 2015)[10, 6, 13], and may therefore provide the potential for considerable geomorphic work in the form of runoff. General circulation models (GCMs) of Titan's atmosphere have characterized Titan's meteorology through the perspective of seasonally- and zonally-averaged precipitation, showing that the seasonal circulation transports methane to the summer pole (Mitchell et al., 2006; Schneier et al., 2012; Lora et al., 2015; Newman et al., 2016; Mitchell and Lora, 2016)[30, 98, 99, 100, 38]. Lost in the averages, however, are the magnitudes and frequencies of rare but extreme precipitation events that may exceed thresholds for sediment transport and erosion (Perron et al., 2006; Jaumann et al., 2008; Black et al., 2012; Neish et al., 2016)[92, 93, 94, 91], incise channels (Molnar et al., 2006; Dibiase and Whipple, 2011; Burr et al., 2013a; Poggiali et al., 2016)[104, 105, 81, 212], or trigger large sediment flows down topographic gradients to produce sedimentary deposits like alluvial fans as in terrestrial settings (Blair and McPherson, 1994; Leier et al., 2005; Arzani, 2012; D'Arcy et al., 2017)[107, 125, 213, 110].

3.2 Methods

We simulate precipitation using the Titan Atmospheric Model (TAM; Lora et al., 2015)[99] with a wetlands configuration, wherein inexhaustible methane reservoirs are imposed poleward of 60° and infiltration equatorward of 45° (Lora and Mitchell, 2015)[43]. Such a surface liquid distribution is motivated by hypothesized "wetlands" or lake districts at the lower elevation polar regions (Neish and Lorenz, 2014)[90]. This model configuration has enabled the GCM to realistically simulate many of the observed features of Titan's atmosphere, includ-

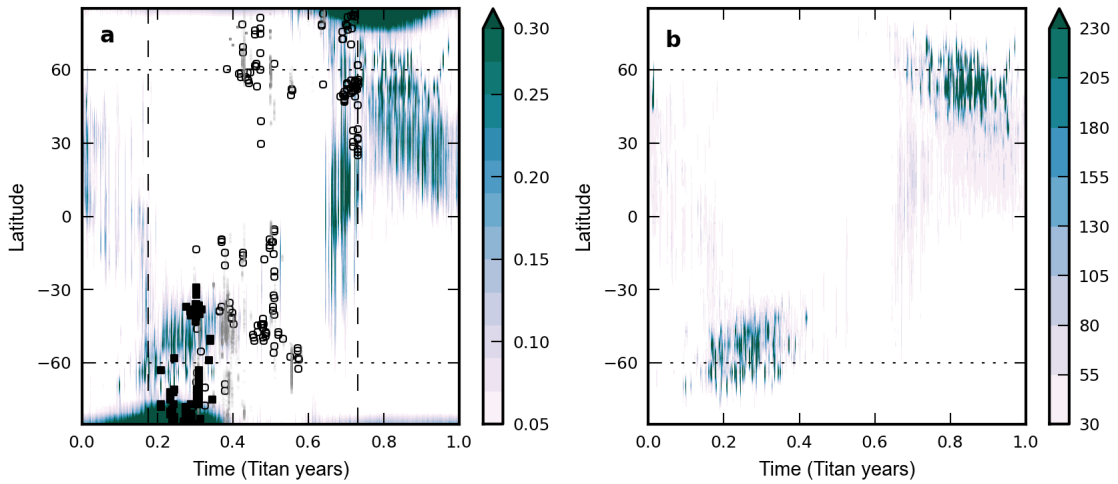

Figure 3.1: **Seasonal methane precipitation**. a) Zonally averaged precipitation (mm d^{-1}) composited over 50 Titan years of the TAM wetlands simulation used in this study, compared to tropospheric cloud locations (Roe et al., 2005; Bouchez and Brown, 2005; Schaller et al., 2006; Rodriguez et al., 2011; Turtle et al., 2011b; Turtle et al., 2017)[22, 18, 19, 27, 29, 31] as observed by ISS (black circles), VIMS (gray circles), and ground-based telescopes (filled black squares). Vertical dashed lines depict observational period extending from the beginning of ground-based observations (Bouchez and Brown, 2005)[18] in December 2001 to approximately May 2017. b) Maximum zonal maximum precipitation (mm d^{-1}) over 50 Titan years of the TAM wetlands simulation used in this study. Wetlands edges are shown by horizontal dotted lines in both panels.

ing the mid-latitude cloud distribution and the paucity of low-latitude clouds during equinox (Mitchell and Lora, 2016)[38](Fig. 3.1a).

3.2.1 TAM details

The TAM GCM solves the primitive equations using a spectral dynamical core. It employs a full non-gray radiative transfer scheme that leverages atmospheric data from Cassini-Huygens, simplified moist convection and saturation vapor pressure schemes (see Chapter 1), and a "bucket" hydrology model wherein surface methane is replenished by precipitation and available to evaporate above a minimum value but is not transported horizontally (Lora and Mitchell, 2015)[43]. Our model is identical to that used by Lora and Mitchell (2015), except for the inclusion of an updated saturation vapor pressure scheme (Lora and Ádámkovics, 2017)[136]. We run the GCM for 50 Titan years (after the atmosphere has already spun up to an equilibrium state, which takes approximately 70 Titan years) at T21 resolution (64 longitude by 32 latitude grid, giving a roughly 5° horizontal resolution) and with 32 unevenly

spaced vertical layers (Lora et al., 2015)[99]. The control wetlands simulations were run with a timestep of 600 seconds, whereas all subsequent sensitivity simulations used a timestep of 900 seconds. Precipitation events are calculated for each output period (approximately 10 Earth days) and each grid cell, and we do not average zonally or over seasonal timescales. This results in a total of 110.08 million precipitation events over 50 Titan years.

3.2.2 Probability density and exceedance probability calculations

Calculation of probability density functions begins with a histogram of every precipitation event (using 1 mm d^{-1} bins up to 1000 mm d^{-1}) in time and longitude at a given latitude. For each latitude, we normalize the number of precipitation events by the latitude to account for the fact that higher latitudes have smaller surface area. Since precipitation values are not affected by spatial averaging biases, we do not normalize the magnitude itself. We instead weight the *counts*, or number, of precipitation events of a certain value by multiplying them by $\cos(\phi)$, where ϕ is latitude. We do this for each of the four latitudes in a given latitude bin and sum the weighted counts to produce a modified precipitation histogram for a given latitude bin. We then divide the histogram by the sum of weighted counts, normalized by the bin length (1 mm d^{-1} in this case), to attain a probability density. This ensures that the integral of the probability density function multiplied by the bin length equals unity for each latitude bin.

Exceedance probability P is calculated as $P = \frac{r}{1+n}$ (Rossi et al., 2016)[214], where r is the rank of the precipitation event (the largest storm has a rank of 1) and n is the number of output periods (53750 for 50 Titan years). Thus, the exceedance probability gives the probability of exceeding a given precipitation value over one output period (Dibiase and Whipple, 2011; Rossi et al., 2016)[105, 214]. The exceedance probability associated with a recurrence interval of 50 Titan years is therefore equal to 1/53750, or ∼1.8e-5, which is by definition the exceedance probability of the maximum precipitation event to occur over that time. We construct exceedance probability profiles for each grid cell. To plot an exceedance probability curve representative of one particular latitude bin, we take the average

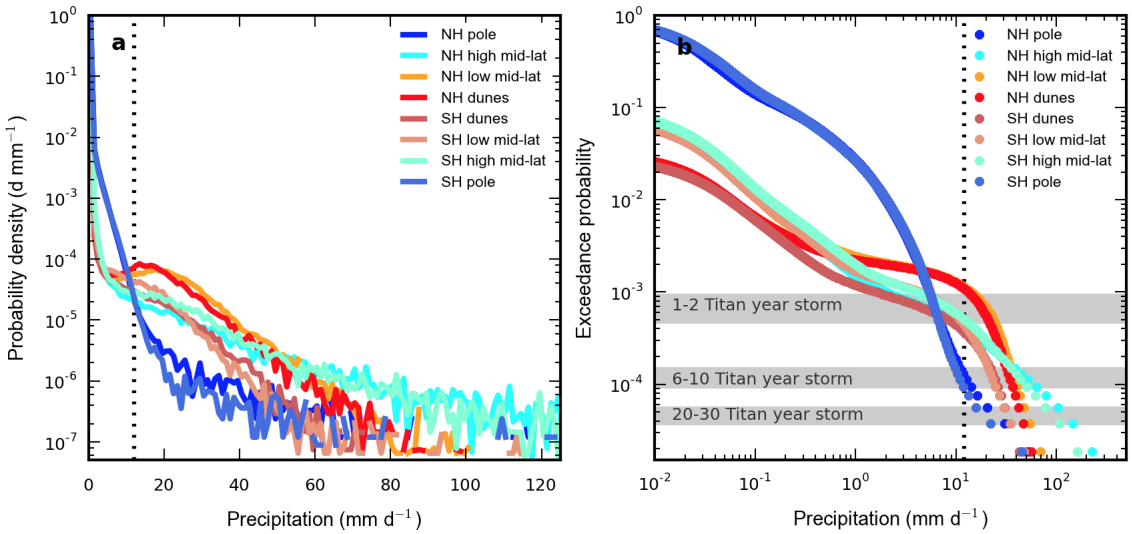

Figure 3.2: **Titan's precipitation statistics**. a) Probability density functions (d mm^{-1}) for precipitation rates (mm d^{-1}) within each latitude bin. Profiles include precipitation rates from every output period and every grid point in the given latitude bin. b) Representative exceedance probabilities (unitless) within each latitude bin taken by averaging precipitation rates for a given exceedance probability. Shaded regions represent associated recurrence intervals. Vertical dotted line in both panels shows minimum precipitation rate (12 mm d^{-1}) estimated for erosion (Perron et al., 2006)[92].

precipitation magnitude of all grid cells within the bin for a given exceedance probability.

Based on 50 Titan years of simulations (one Titan year is ∼29.5 Earth years), we examine the spatial distribution of precipitation events by separating the data into eight distinct latitude bins, referring to them from here on as the dunes (0-22.5°), low mid-latitudes (22.5-45°), high mid-latitudes (45-67.5°), and poles (67.5-90°). Probability density functions (Fig. 3.2a) are calculated using every precipitation event within a given latitude bin (normalized by cosine of latitude to account for smaller polar surface area). Exceedance probability curves (Fig. 3.2b)—cumulative distribution functions that give the probability over a given timescale of exceeding certain precipitation values—are calculated using standard rank-frequency analysis (Dibiase and Whipple, 2011; Rossi et al., 2016)[105, 214]. The inverse of the exceedance probability for a precipitation event gives that event's approximate recurrence interval—in units of model output periods (which are 10 Earth days)—thus quantifying storm frequency.

To calculate the maximum zonal maximum precipitation in Fig. 3.1b, we consider a given time of the year and latitude and take the zonal maximum for each of the 50 Titan years of the simulation. Of those 50 values, we take the maximum again to construct the

contours. The outputted precipitation values from TAM are per unit area (converted from kg m^{-2} s^{-1} to mm d^{-1} using the liquid density of methane) and therefore not affected by biases in spatial averaging, i.e. the fact that grids at higher latitudes have smaller areas. The temporal resolution of our model output, however, does affect precipitation magnitudes in that averaging over 10 Earth days can diminish the apparent intensity of storms with durations much shorter than this interval. Thus in this sense, our outputted precipitation magnitudes can be interpreted as relatively conservative estimates.

3.3 Quantifying regional precipitation magnitudes and frequencies

The zonal mean precipitation of our simulations (Fig. 3.1a; Fig. 3.3a) reflects Titan's dominantly dry climate with seasonal precipitation activity in the mid-latitude and polar regions (Mitchell and Lora, 2016)[38], in good agreement with the timing and location of observed clouds. Our model successfully captures the sporadic nature of cloud activity and its cessation in northern spring (Fig. 3.1a), in contrast to the continuous band of precipitation reported by previous models (Mitchell et al., 2006; Schneider et al., 2012)[30, 98]. Although total precipitation is largest over the poles, maximum precipitation intensities peak in the mid-latitudes, near the boundary of the wetlands (Fig. 3.1b). Probability density functions show that low-magnitude precipitation (0-10 mm d^{-1}) is particularly persistent in the polar regions, medium-magnitude precipitation (10-50 mm d^{-1}) just within the minimum range of erosion (Perron et al., 2006)[92] (Fig. 3.2, vertical dotted line) is most prevalent in the northern hemisphere (NH) dunes and NH low mid-latitudes, and high-magnitude precipitation (>50 mm d^{-1}) occurs primarily in the high mid-latitudes of both hemispheres and rarely elsewhere. The most extreme storms ($\sim$100 mm d^{-1}) occur almost exclusively in the high mid-latitudes and have recurrence intervals of 20-30 Titan years (Fig. 3.2b).

To connect precipitation to potential erosion, we use the value calculated by Perron et al. (2006)[92], which estimates the minimum precipitation rate required for sediment transport and subsequent erosion at the Huygens landing site on Titan. The calculation of

this minimum precipitation rate is based on the relationships between precipitation, open-channel flow, and the threshold of sediment transport (Perron et al., 2006)[92], and therefore uses information of observed grain sizes and geomorphology (e.g., channel geometry, channel slope, drainage area) of nearby fluvial networks. Thus, the estimate from Perron et al. (2006)[92] is specific to the Huygens landing site. Differences in geomorphic parameters likely lead to different sediment transport thresholds and therefore different precipitation estimates.

Still, the ground observation data from the Huygens landing site, where centimeter-sized grains are dominant based on Huygens DISR images, best represent our knowledge of Titan's erosional threshold. Indeed, similarly sized grains have also been inferred from high radar brightness values of channel features in Xanadu (Le Gall et al., 2010)[78]. We therefore use a similar range of values from the Perron et al. (2006) study (12-360 mm d^{-1} for 1-10 cm grain sizes) to define low (less than 10 mm d^{-1}), medium (10-50 mm d^{-1}, just within the minimum range of erosion), and high (greater than 50 mm d^{-1}) magnitude precipitation events in our study, reiterating that 12 mm d^{-1} is the *minimum* rate necessary for erosion and that local erosion across Titan may require values closer to $\sim$360 mm d^{-1}. However, the observed global coverage of fluvial features combined with the results of our study (values exceeding 350 mm d^{-1} only occur in the high mid-latitudes in our simulations) suggest that a majority of Titan's mechanical erosion is connected to precipitation events of considerably lower magnitude than $\sim$360 mm d^{-1}.

3.4 Precipitation and geomorphic connections

Of available geomorphic observations, perhaps the best indicators of infrequent but extreme storms on Titan that we can leverage to contextualize our results are alluvial fans identified with Cassini's Synthetic Aperture Radar (SAR) instrument (Birch et al., 2016; Radebaugh et al., 2016; Cartwright and Burr, 2017)[82, 83, 84]. Non-hydrologic factors such as sediment size, material properties, and topography may also affect alluvial fan formation, but sedimentary deposits, particularly large ones, are likely associated with intense precipitation

that initiates transport and deposition of large amounts of materials (Blair and McPherson, 1994; Moore and Howard, 2005; Arzani, 2012; Borga et al., 2014; Mather et al., 2016; D'Arcy et al., 2017)[107, 117, 213, 108, 215, 110].

We use alluvial fans identified by Cassini's Synthetic Aperture Radar (SAR) instrument (Birch et al., 2016; Radebaugh et al., 2016; Cartwright and Burr, 2017)[82, 83, 84] for comparisons to precipitation statistics. For each latitude bin of ten degrees, we collect the number of alluvial fans identified and divide by the surface area, normalized by latitude and by coverage area, to attain the fan density, as in Birch et al. (2016)[82]. The black bars in Fig. 3.3 and all subsequent figures showing fan density represent the fans identified by a single source (Birch et al. (2016)[82], since it provides the most extensive coverage) to avoid inconsistencies over fan identification mechanisms across studies. The grey extensions of these bars represent the additional fans identified by Radebaugh et al. (2016)[83] and Cartwright and Burr (2017)[84]. Significant overlap across these three studies exists, but for each study there were fans identified that were left unidentified by the other two. Birch et al. (2016)[82] reported the most extensive global coverage of fans. In addition to these fans, Radebaugh et al. (2016)[83] discussed the Mezzoramia fan system in the high southern mid-latitudes, and Cartwright and Burr (2017)[84] noted three fans in the high northern latitudes. Additionally, Radebaugh et al. (2016)[83] and Cartwright and Burr (2017)[84] identified seven fans in the Elivagar Flumina fan system, which Birch et al. (2016)[82] counted as only one.

A large majority of the fans observed, and therefore used in our analysis, were identified using Cassini's Synthetic Aperture Radar (SAR) instrument, which provided images at a resolution of up to $\sim$300 m, thus eliminating recognition of fans smaller than $\sim$9 km^2 (assuming a frame size of 10 x 10 pixels; Birch et al. (2016)[82]). Fans from Birch et al. (2016)[82] were identified with varying degrees of certainty depending on whether they exhibited characteristics common to terrestrial alluvial fans. These characteristics included triangular morphology, SAR-brightness, topographic relief, and observable channel sources. Fans with all four of these characteristics were classified as "most certain" and those with three of the four characteristics as "highly certain." Of the 82 fans identified in that study,

58 were either "most certain" or "highly certain" to be alluvial fans. And of those, the distribution still exhibits peaks in the mid-latitude regions, with the 24 fans "requiring additional data" (those lacking more than one of the four characteristics) spread relatively uniformly in latitude.

3.4.1 Alluvial fans as climate records

Cartwright and Burr (2017)[84] found that high latitude alluvial fan features resemble terrestrial deposits from sheetfloods, showing characteristics similar to fluid-gravity flow deposits with well-sorted and/or fine-grained sediments and downfan fining, while low latitude alluvial fan features resemble debris flows. This is contrary to the authors' prediction that fine-grained sediments in the high latitudes would reduce permeability, increase pore pressure, and likely promote debris flow initiation (Iverson, 2005)[216]. Possible explanations for the observed meridional distribution of alluvial fans found by the authors include potential meridional changes in radar signal processes, sediment and bedrock characteristics, and/or surface processes. Interestingly, the observed distribution—of alluvial fans formed by sheetfloods in the high latitudes and by debris flows in the low latitudes—is qualitatively consistent with the results of our study: high magnitude discharge/precipitation events in the higher latitudes would produce a higher percentage of fluid relative to sediment in the resulting flow, likely forming sheetfloods. The fans identified most definitively as sheetfloods are found at 68-69°N, a region on the boundary between the high mid-latitude and polar zones of our study and potentially subject to extreme precipitation and variability given our results (see Fig. 3.1b, Fig. 3.3). Thus, meridional changes in climate provide a plausible alternative explanation for the distribution and types of alluvial fans. One other explanation offered by the authors is that the observed depositional features are not actually alluvial fans, but distributary fluvial systems instead. Nevertheless, even if these features are indeed distributary fluvial systems, they would still serve our purpose as potential indicators of extreme storms and variability based on terrestrial analogs (Gibling et al., 2005; Davidson et al., 2013)[126, 217].

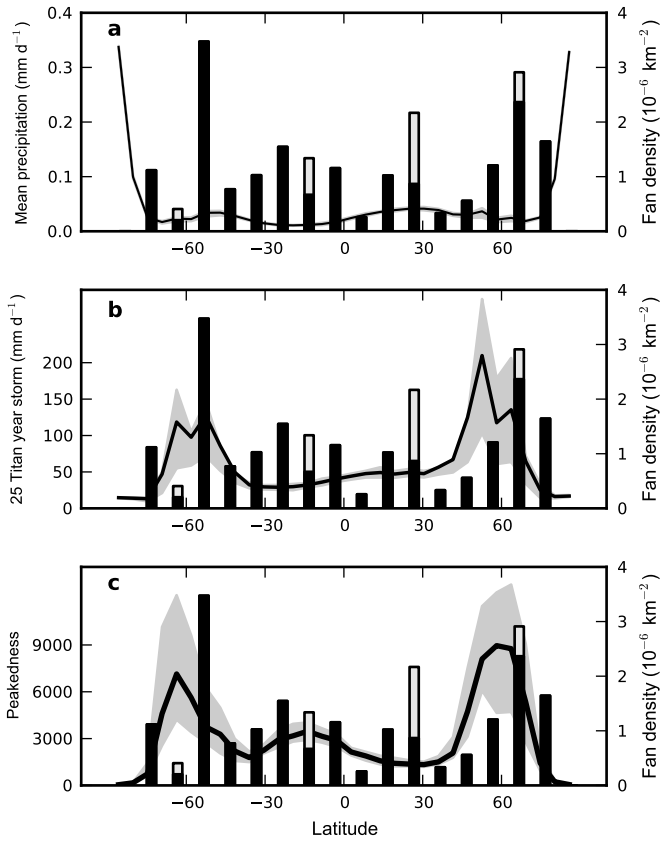

Figure 3.3: **Rainfall compared to alluvial fans**. a) Temporally and zonally averaged precipitation (solid, mm d^{-1}) over the full 50 Titan year simulation, b) zonally averaged magnitude (bolded, mm d^{-1}) of 25 Titan year storms, and c) zonally averaged peakedness (heavily bolded, unitless) with maximum and zonal average taken over the full 50 Titan year simulation. Observed alluvial fan density distribution (black bars from Birch et al. (2016)[82], additional light bars from Radebaugh et al. (2016)[83] and Cartwright and Burr (2017)[84]), in number of fans per 10^6 km^2, on the right y-axis for each panel. Each profile (including mean precipitation) is shaded between the 25th and 75th percentile of the zonal averaging.

Titan's sediment characteristics and availability, and their resulting impact on geomorphic work, are poorly constrained. Organic haze particles are presumed to settle onto the surface at all latitudes (Raulin et al., 2012; Hörst, 2017)[218, 219], but latitudinal variations in surface material properties are likely. Vast sand seas (Lorenz et al., 2006a)[70] and cobble deposits (Tomasko et al., 2005; Le Gall et al., 2010)[74, 78] dominate the lower latitudes, providing abundant particles for mobilization. Crenulated—or dissected and mountainous—terrain is also prominent in the lower latitudes where mountainous regions composed of water ice may provide the cobbled materials necessary for transport and incision. Such features are noticeably absent from the higher latitudes, which exhibit more fine-grained, clay-like sediment primarily composed of organic products (Hayes, 2016; Birch et al., 2017; Cornet et al., 2015)[52, 121, 220]. These latitudinal differences in surface material properties could impact the formation mechanisms of sedimentary deposits and influence their observable morphology and characteristics (Cartwright and Burr, 2017)[84].

However, sedimentary deposits such as alluvial fans still require fluid flow to initiate sediment entrainment and transport. On Titan, this fluid must come from methane precipitation—thus, to a considerable extent, precipitation should influence the generation of these features. Examples from the terrestrial geomorphology literature support the connection between alluvial fans and extreme precipitation events (Blair and McPherson, 1994)[107], wherein large sedimentary deposits are often associated with high magnitude discharge events (Arzani, 2012; Borga et al., 2014)[213, 108]. Considering the resolving capacity of the instrument, alluvial fans on Titan observed by SAR are likely biased to be large as well. Additionally, terrestrial debris flow initiation has been linked to storm intensity rather than average rainfall rates, illuminating the sensitivity of sedimentary deposits to climate changes (D'Arcy et al., 2017)[110]. Inherent in our study is the uncertainty that fan formation mechanisms in terrestrial settings would translate to Titan. Given, though, the geomorphological similarity between the two worlds, as well as the unclear interaction between precipitation and sedimentology on Titan's surface, we take the simplest route and assume mechanistic similarity as well. Thus, although we cannot completely rule out the potential impact of other meridional variations, we propose meridional variations in climate as the most likely driving force

behind the distribution of depositional features on Titan.

3.4.2 Rainstorm frequency and variability

Large terrestrial fans can result from floods recurring on average every few centuries (Beaty, 1970)[221], and typically result from deposition over thousand- and million-year timescales (Mather et al., 2016)[215]. Although we are unable to run simulations for such long times, we find in our simulations that the latitudinal variation of rainfall intensity from storms with recurrence intervals of 25 Titan years (the approximate recurrence interval of the extreme $\sim$100 mm d^{-1} storms in the high mid-latitudes; see Fig. 3.2b) correlates well with alluvial fan density (Fig. 3.3b) compiled from Birch et al. (2016)[82], Radebaugh et al. (2016)[83], and Cartwright and Burr (2017)[84], with peaks in the high mid-latitudes of both hemispheres.

In addition to precipitation magnitude, we also examine the regional patterns of climatic variability. A previous study showed that terrestrial megafans tend to be observed globally in areas with high values of discharge variability, which is thought to promote channel instability and avulsion (Leier et al., 2005)[125], processes that are reasonably assumed to be present on Titan given the presence of channelized flow (Lorenz et al., 2008a; Langhans et al., 2012; Burr et al., 2013a; Burr et al., 2013b)[76, 80, 81, 122] and indications of flood events (Jaumann et al., 2008; Wall et al., 2010; Turtle et al., 2011b)[93, 62, 29]. To quantify climatic variability, we follow the approach of Leier et al. (2005)[125] and calculate the peakedness, a proxy for variability, in each grid cell as the ratio of maximum to zonal mean precipitation over the 50 Titan year simulation. We find that zonal peakedness is highest in the high mid-latitudes, approximately where observed alluvial fans are most concentrated (Fig. 3.3c). A secondary maximum in peakedness in the SH low latitudes corresponds with a local rise in the alluvial fan density in that region. Such a correlation suggests that the opposing local rise in alluvial fan density in the NH low latitudes reflects precipitation-induced geomorphic work from an earlier climate epoch with an opposite orbital configuration (Aharonson et al., 2009; Lora et al., 2014)[58, 59] (note, however, that the fans between 20-30°N all come from one location, Elivagar Flumina, and fan identification varies across different studies).

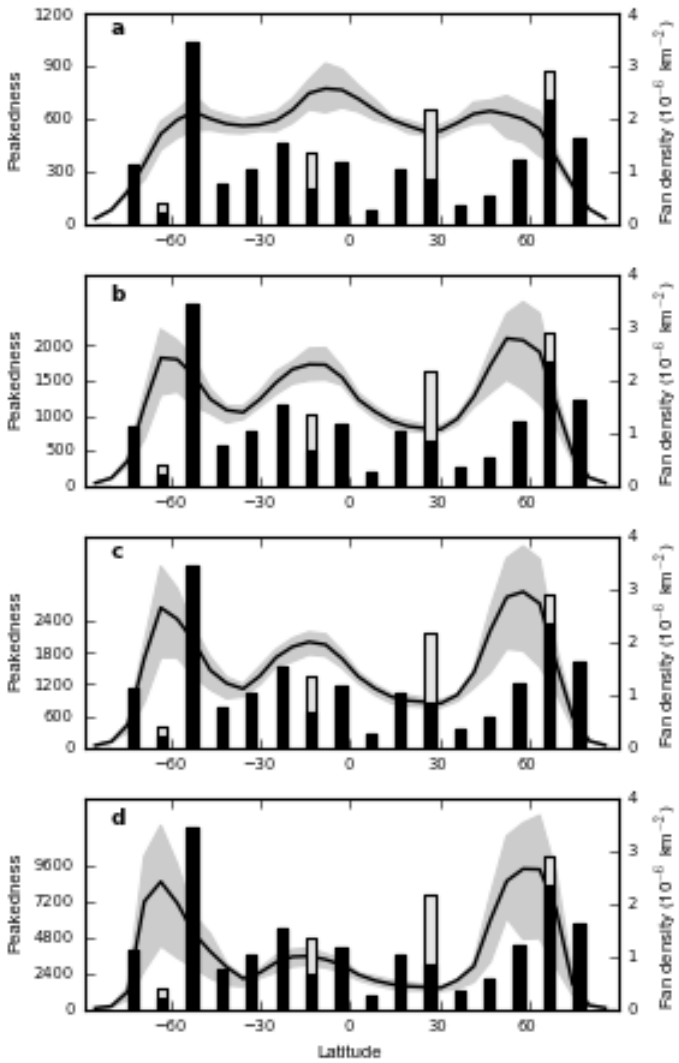

Figure 3.4: **Peakedness timescale sensitivity**. Zonally averaged peakedness profiles (solid lines; shaded between 25th and 75th percentile) for maximum and zonal average taken over, from top to bottom: a) 1 Titan year, b) 5 Titan years, c) 10 Titan years, and d) 50 Titan years, on the left y-axis of each panel. Observed alluvial fan density distribution (Birch et al., 2016; Radebaugh et al., 2016; Cartwright and Burr, 2017)[82, 83, 84](bars), in number of fans per 10^6 km^2, is plotted on the right y-axis of each panel. Note the differences in peakedness scale for different timescales.

We calculate peakedness as the maximum precipitation event at a given grid point divided by the temporally and zonally averaged precipitation at that latitude over the full 50 Titan years of the simulation. Zonal peakedness profiles are sensitive to the timescale over which the average and maximum are taken (Fig. 3.4). In particular, as the average and maximum are taken over shorter timescales, peakedness increases at the equator due to the growing importance of seasonal rainstorms to the average precipitation signal and the reduced chance of extreme storms occurring. Such sensitivity to timescale suggests the potential role of inter-annual variability in Titan's hydrological cycle, an aspect of Titan's climate that remains largely unexplored. Still, despite such variability, the peakedness profile peaks in the high mid-latitudes and correlates well with the observed distribution of alluvial fans even for the relatively short timescale of five Titan years.

Zonal profiles of storm intensities for several given recurrence intervals (Fig. 3.5) also show better correlations to the observed alluvial fan distribution for rarer, larger storms. Alluvial fans are observed using Cassini Synthetic Aperture Radar (SAR) data, which provide images at a resolution of up to ∼300 m, thus eliminating recognition of fans smaller than ∼9 km^2 (Birch et al., 2016)[82]. We note that large alluvial fans are likely formed over longer timescales than our simulation, perhaps on the order of a million years (Mather et al., 2016)[215]. Considering computation times, it is impossible to run simulations for similar lengths of time. Nevertheless, our purpose is to evaluate the latitudinal dependence of extreme events—and their potential connections to large sediment depositional features—for which our simulation lengths are appropriate.

In the lower latitudes, variability is weaker and major storms capable of transporting larger grain sizes (> 50 mm d^{-1}) occur less frequently than in the high mid-latitudes (Figs. 3.2, 3.3), whereas storms capable of transporting smaller grain sizes (10-50 mm d^{-1}) occur more frequently in the lower latitudes than anywhere else (Fig. 3.2). Depending on erosional thresholds, inefficient fluvial erosion and transport in low-latitude regions may account for lower alluvial fan concentrations, as well as limited dissection of cratered terrain (Wood et al., 2010; Neish and Lorenz, 2014; Moore et al., 2014)[86, 90, 120] and the production of coarse gravel deposits that further inhibit erosion (Howard et al., 2016; Birch et al., 2016)[222, 82].

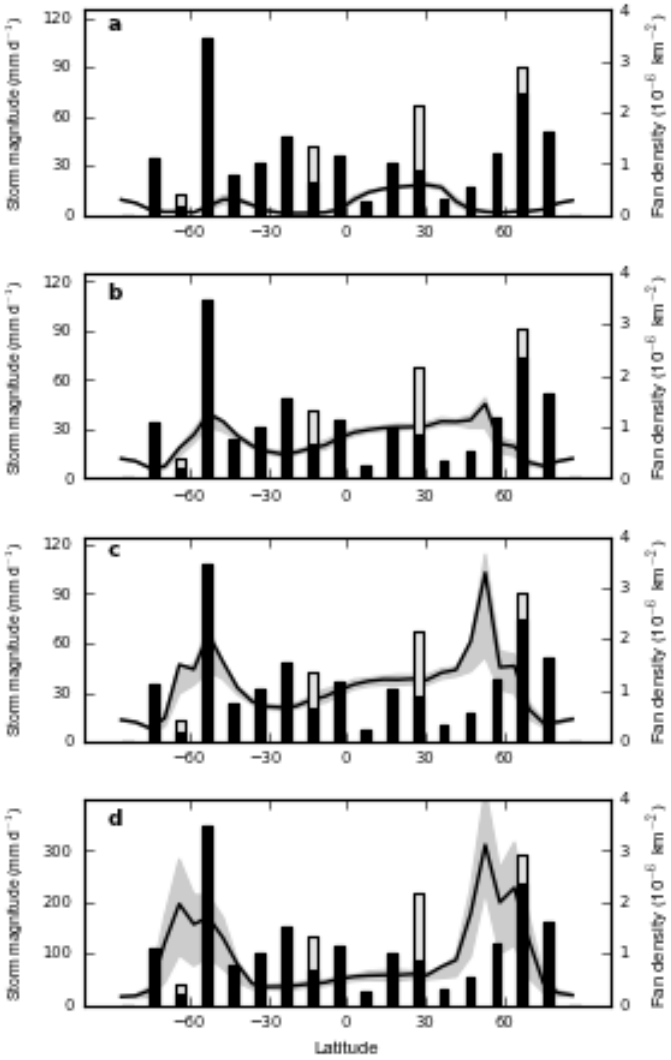

Figure 3.5: **Additional storm frequency comparisons to alluvial fans**. Zonally averaged storm magnitude profiles (solid lines; shaded between 25th and 75th percentile) for a recurrence interval of, from top to bottom: a) 1 Titan year, b) 5 Titan years, c) 10 Titan years, and d) 50 Titan years, on the left y-axis of each panel. Observed alluvial fan density distribution (Birch et al., 2016; Radebaugh et al., 2016; Cartwright and Burr, 2017)[82, 83, 84](bars), in number of fans per 10^6 km^2, is plotted on the right y-axis of each panel. Note the difference in storm magnitude scale for the bottom panel.

Titan's low latitudes are often characterized as dry and convectively stable with few storms, implying that equatorial fluvial features (Lorenz et al., 2008a; Langhans et al., 2012; Burr et al., 2013a)[76, 80, 81] likely produced by mechanical erosion and sediment transport due to channelized flows (Perron et al., 2006)[92], were formed during a wetter past climate (Griffith et al., 2008; Griffith et al., 2009)[7, 223]. However, large storms have been observed in the tropics (Schaller et al., 2009; Turtle et al., 2011b)[28, 29], and suggested in previous models (Schneider et al., 2012)[98]. Our results suggest that the observed equatorial surface features *can* form in Titan's present climate. Medium-magnitude precipitation necessary for transport of small grain sizes (>10 mm d^{-1}) occurs in the NH low latitudes approximately every Titan year (Fig. 3.2b, top shaded region), suggesting a seasonal driver. Thus, the NH low latitude precipitation may be the monsoon-like outpourings of Titan's intertropical convergence zone (ITCZ), though this same precipitation signal is more rare in the SH low latitudes, where exceedance probability for ∼10 mm d^{-1} precipitation is ∼40% that in the NH low latitudes (Fig. 3.2b).

The low-latitude precipitation asymmetry in our simulations is due to Titan's orbital parameters since simulations with zero orbital eccentricity produce hemispheric symmetry in the low-latitude precipitation signal (see next section). Geomorphological observations so far do not indicate significant low-latitude hemispheric differences in the density of fluvial features (Lorenz et al., 2008a; Langhans et al., 2012; Burr et al., 2013a)[76, 80, 81], though crenulated terrains appear to be more common in the southern low latitudes. The low-latitude surface morphology in general appears well-preserved (Wood et al., 2010; Moore et al., 2014)[86, 120] and able to retain surface features carved during previous climate epochs. As such, though heavier storms capable of erosion occur more often in the NH low latitudes in Titan's current climate configuration, the same storms may have incised the SH low latitudes during a previous orbital configuration (Aharonson et al., 2009; Lora et al., 2014)[58, 59], though the timescale of landscape evolution on Titan given our precipitation statistics is left for future work. In the higher latitudes, climate changes due to Milankovitch cycles appear to have little effect on the location of high magnitude storms, as shown by the zero orbital eccentricity simulations.

3.4.3 Stretched exponential distribution function

We perform an additional characterization of storm variability by fitting the exceedance probability curves using the stretched exponential distribution (Wilson and Toumi, 2005; Rossi et al., 2016)[224, 214], which provides a flexible and fundamental model for typical rainfall distributions, with the scale parameter (r_0) as a measure of probability and the shape parameter (c) as a measure of variability of extreme precipitation events.

We fit the high-magnitude precipitation tails of the exceedance probability curves to the stretched exponential distribution function, $P = exp[-(\frac{r}{r_0})^c]$, where r is the precipitation distribution, and r_0 and c are the scale and shape parameters, respectively. We linearize the stretched exponential distribution function by taking the natural log of the precipitation distribution twice, and then find the slope and y-intercept of the linear regression, corresponding to c and $-c * ln(r_0)$ respectively, using least squares (Rossi et al., 2016)[214]. We use the 12 mm d^{-1} erosion estimate (Perron et al., 2006)[92] to demarcate the beginning of this high-magnitude precipitation tail.

Fig. 3.6 shows the stretched exponential distribution function fits for each representative exceedance probability curve. The scale parameter r_0, a measure of probability, can be obtained from the y-intercept of the fitted stretched exponential distribution function via $r_0 = exp[-y_0/c]$, where y_0 is the y-intercept. The shape parameter c is a nondimensional measure of variability—lower values indicate a flatter line and thus higher variability. For each latitude bin, the shaded region indicates the spread of precipitation rates for a given exceedance probability. Overall, the spread is quite small, with the only substantial variation occurring for low-magnitude precipitation in the polar regions, as expected given that the bulk of Titan's total precipitation occurs in those regions.

The shape parameter formulation of variability, in agreement with the peakedness measure, demonstrates high variability (i.e. low fitted shape parameters) in the high mid-latitudes, while additionally showing high variability in the polar regions (Table 3.1). High polar variability in this formulation results from the stretched exponential distribution measure of variability considering only the high-magnitude precipitation, whereas the peakedness

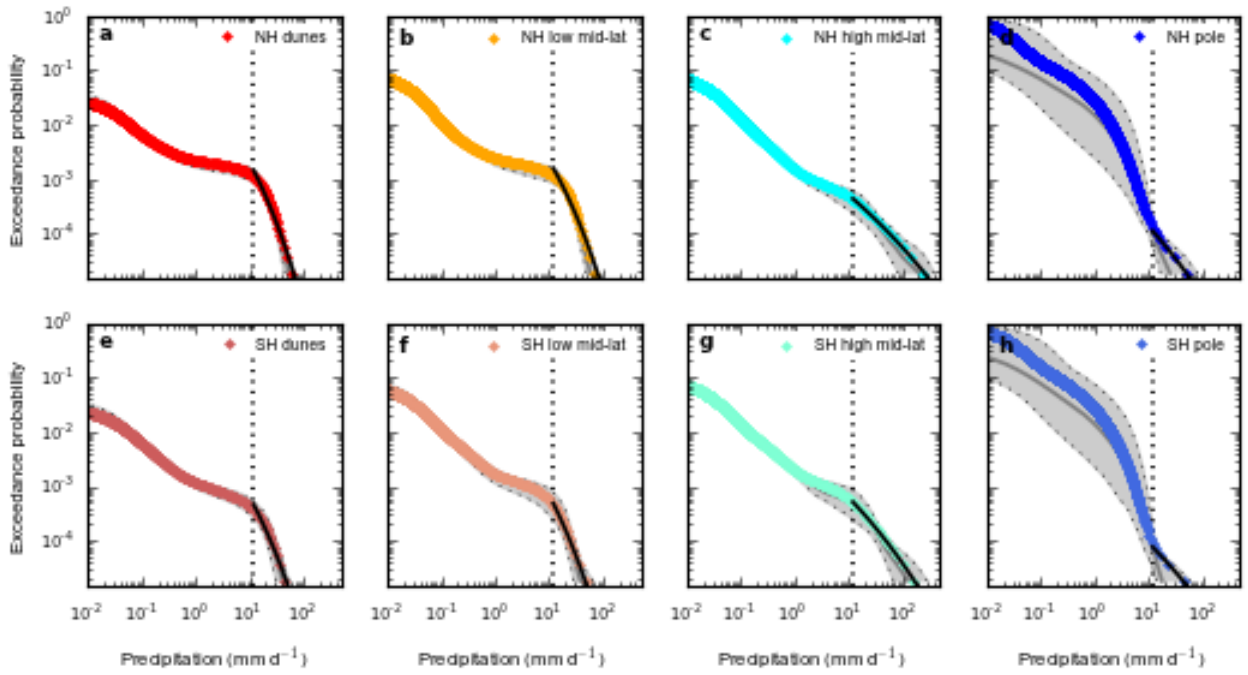

Figure 3.6: **Individual regional exceedance probability curves**. Stretched exponential distribution function fits (black line) to representative exceedance probability curves (as in Fig. 3.2) for extreme precipitation (>12 mm d^{-1}; vertical dotted line (Perron et al., 2006)[92]) in each region. Colored circles indicate average precipitation magnitudes of cells within latitude bin for given exceedance probabilities. Gray shaded regions bracketed by dotted lines indicate spread (between 15th and 85th percentiles) of precipitation magnitudes for given exceedance probabilities. Dark grey line indicates median of precipitation magnitudes for given exceedance probabilties.

		0-22.5°	22.5-45°	45-67.5°	67.5-90°
r_0	NH	0.02	0.01	1.2e-7	2.2e-7
	SH	3.6e-3	0.01	5.6e-6	1.1e-8
c	NH	0.30	0.28	0.11	0.12
	SH	0.25	0.26	0.14	0.11

Table 3.1: **Stretched exponential distribution parameters**. Fitted scale (r_0, mm d^{-1}) and shape (c, unitless) parameters for each latitude bin. Low scale parameter values indicate low probability. Low shape parameter values indicate high variability.

measure considers the full precipitation range. Similarly high variabilities in high-magnitude precipitation events in the high mid-latitudes and polar regions indicate that similar dynamic mechanisms, namely baroclinic instabilities (Lora and Mitchell, 2015)[43], act to provide these rare, variable, high-magnitude storms in both regions, though the storms are not as intense or frequent in the polar regions (Fig. 3.2). Comparing Titan's variability to Earth's, typical c values for terrestrial precipitation are $\sim \frac{2}{3}$ (Wilson and Toumi, 2005)[224], while c values in our simulations do not exceed $\frac{1}{3}$. Such a comparison suggests that Titan's overall climate variability is higher than Earth's, in agreement with Titan's potential for more violent storms (Lorenz et al., 2005)[10].

The stretched exponential distribution function confirms the results of the peakedness calculations, namely that variability is high in the high mid-latitudes, and enables a simplistic comparison of precipitation variability between Earth and Titan. Future work can shed further light on the hydrologic differences between planetary atmospheres, particularly those impacted by climate changes.

3.5 Sensitivity simulations

To test the sensitivity of our results to surface liquid conditions, orbital insolation forcings, and their resulting feedbacks, we run three additional experiments hereafter referred to as the aquaplanet, reduced wetlands, and zero orbital eccentricity experiments. The aquaplanet model is initialized with a global methane ocean $\sim$500 m in depth, with all other physics kept the same. The reduced wetlands case is initialized with the same state as the control wetlands case except with the imposed wetlands extending poleward of 70°. Lastly, the zero orbital eccentricity experiment is initialized with the same state as the control wetlands case, but with the eccentricity set to zero, thereby changing the insolation forcing.

To facilitate comparison to the control wetlands simulation (with wetlands boundary at 60° and Titan's present-day orbital eccentricity), we run our supplementary aquaplanet, reduced wetlands, and zero orbital eccentricity experiments for 50 Titan years (after the model has already equilibrated). We construct probability density functions and exceedance

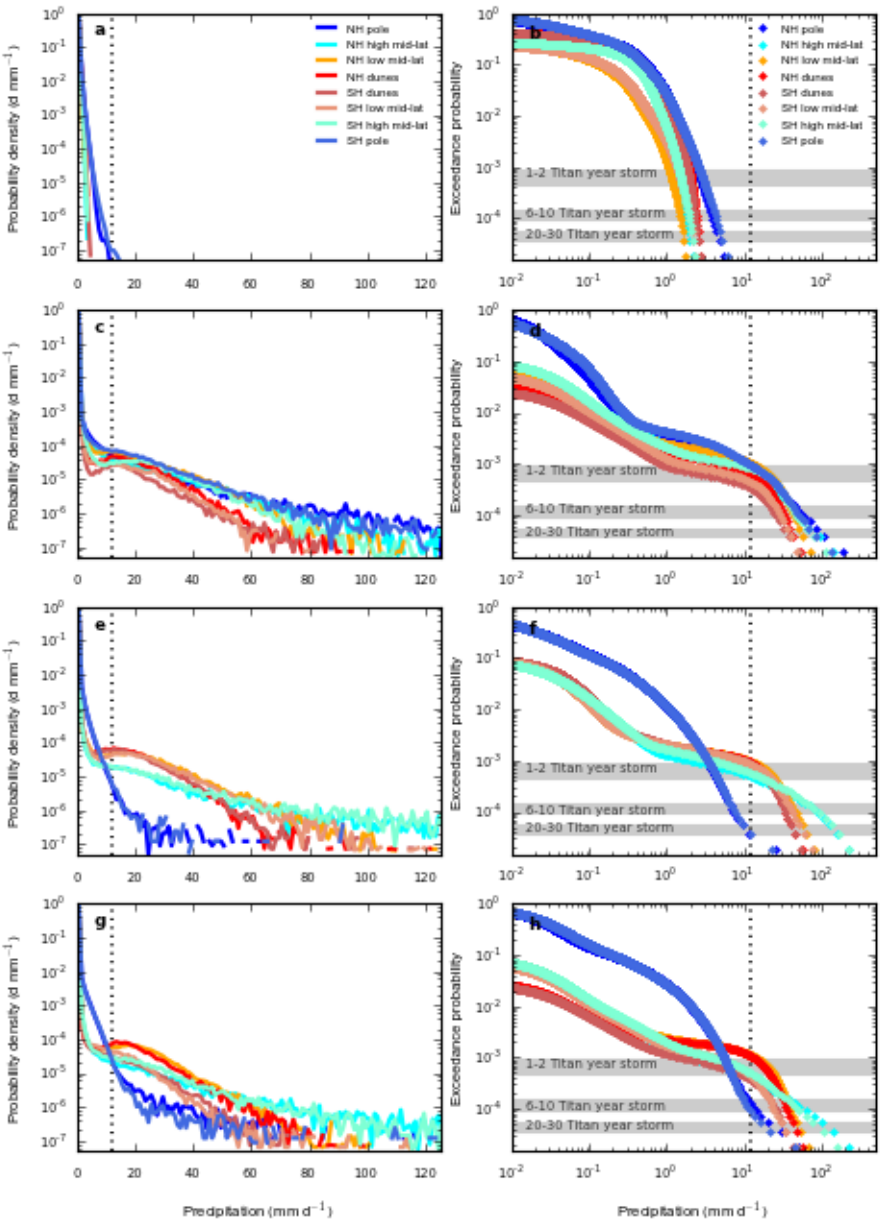

Figure 3.7: **Precipitation statistics for sensitivity experiments**. Probability density functions and exceedance probability curves, as in Fig. 3.2 of main text, for 50 Titan years of the: a,b) aquaplanet simulation, c,d) reduced wetlands simulation, e,f) zero orbital eccentricity simulation, and g,h) control wetlands simulation. Vertical dotted line in all panels again represents minimum precipitation rate estimated for erosion (Perron et al., 2006)[92].

probability curves as for the control simulation (Fig. 3.2) for each sensitivity experiment to produce Fig. 3.7.

3.5.1 Aquaplanet simulation

The aquaplanet case exhibits a markedly different hydroclimate from the wetlands case, including much weaker precipitation rates, seemingly little regional variation in precipitation statistics, and the most intense precipitation in the poles (Fig. 3.7). The peakedness profile of the aquaplanet case exhibits mid-latitude peaks similar to those in the wetlands case but farther equatorward, at $\sim 30^\circ$ (Fig. 3.8). Thus, even in the aquaplanet case, relatively strong storms occur in the mid-latitudes. These storms are much weaker than in the wetlands cases, and are not as strong as storms at the poles, but they are still large relative to the mean precipitation in the mid-latitude regions, thus producing the observed peakedness maxima. However, the peakedness values themselves are very small compared to the wetlands cases (Fig. 3.8).

3.5.2 Reduced wetlands simulation

We test the sensitivity of our results to reducing the latitudinal extent of wetlands, moving the boundary to 70°. In these simulations, there is a corresponding poleward shift in each hemisphere of the region of maximum zonal maximum precipitation (Fig. 3.9), with the most intense storms occurring in the vicinity of the wetlands boundary (as was the case for the control simulations with the 60° boundary; see Fig. 3.1b and Fig. 3.3c). Fig. 3.7 demonstrates the poleward transition of the extreme precipitation region as the wetlands become more restricted, with the polar and high mid-latitude profiles overlapping for large precipitation values. However, the region of greatest peakedness values remains close to 60° in the reduced wetlands simulation, as it was in the control case (Fig. 3.8). The SH low latitude peakedness peak is significantly larger (relative to the mid-latitude peaks) in the reduced wetlands case than in the control case (Fig. 3.8). The reason for this deserves further study, but it is noteworthy that peakedness values in the mid-latitudes are lower

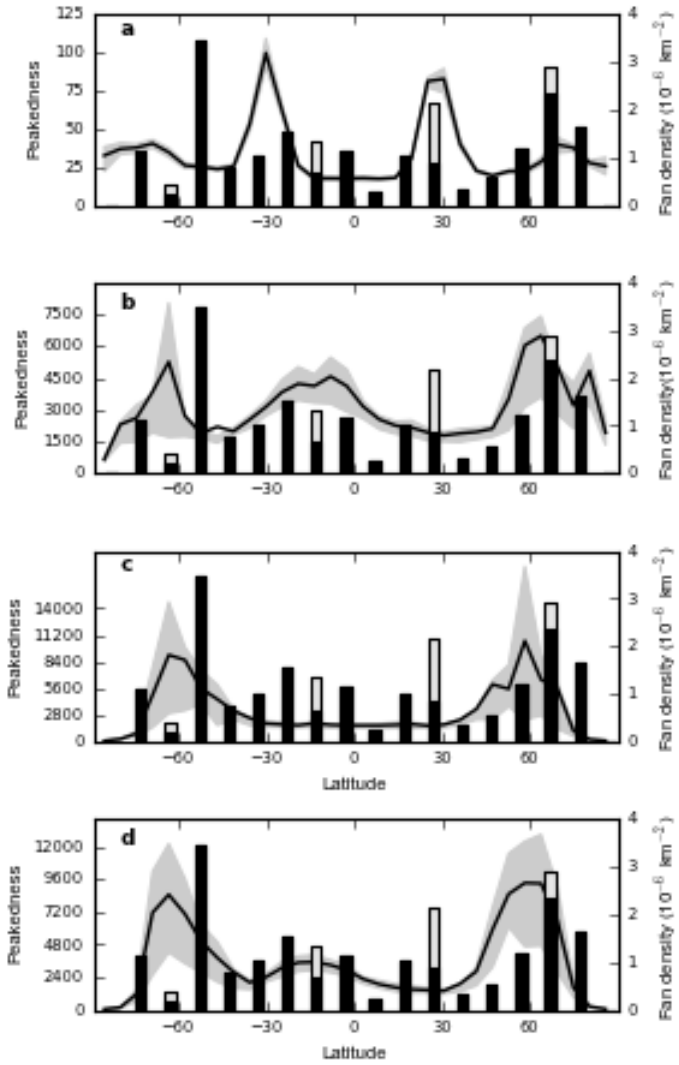

Figure 3.8: **Peakedness for sensitivity experiments**. Zonally averaged peakedness profiles (solid lines; shaded between 25th and 75th percentile) for maximum and zonal average taken over 50 Titan years for, from top to bottom: a) the aquaplanet case, b) the wetlands case with boundary at 70°, c) the zero orbital eccentricity case with boundary at 60°, and d) the control wetlands case with boundary at 60°. Observed alluvial fan density distribution (Birch et al., 2016; Radebaugh et al., 2016; Cartwright and Burr, 2017)[82, 83, 84](bars), in number of fans per 10^6 km^2, is plotted on the right y-axis of each panel. Note the differences in peakedness scale between all cases.

in the reduced wetlands case than in the control case, whereas peakedness values in the SH low latitudes of both simulations are comparable. Intense storms still occur near and equatorward of 60° in the reduced wetlands case and are of comparable strength to those in the control case (Figs. 3.7, 3.9).

Thus, when combined with the mid-latitude peaks in peakedness in the aquaplanet case (Fig. 3.8), the reduced wetlands simulation suggests that there is a preferred region of baroclinicity in the 50-70° region regardless of the specific location of the wetlands boundary. Indeed, a previous general circulation model study using a dry model suggested that weak storms in the high mid-latitudes on Titan are baroclinic (Lebonnois et al., 2012)[225]. The baroclinicity in our model is perhaps locally enhanced by the wetlands boundary (Mitchell and Lora, 2016)[38], which sharpens the temperature gradients that drive baroclinic storms due to the abrupt change between dry ground and reservoirs of abundant surface liquid subject to evaporative cooling. But the fundamental aspects of our results, i.e. extreme storms and high variability in the mid-latitudes correlated with the alluvial fan distributions, are independent of the exact location of the wetlands boundary.

While the region of extreme mid-latitude storms shifts in correspondence with the wetlands boundary, there is abundant evidence to suggest that Titan's polar regions are a unique environment significantly different from the low and mid-latitudes, and that the wetlands boundary in our idealized simulations should be near 60° and not too far equatorward or poleward of this latitude. Noticeable changes in the sedimentological environment (Cornet et al., 2015; Birch et al., 2017b; Malaska et al., 2016)[220, 121, 226], elevation (Lorenz et al., 2013)[88], surface temperature (Jennings et al., 2016)[34], near-surface humidity (Lora and Ádámkovics, 2017)[136], and crater distribution (Neish and Lorenz, 2014)[90] around 60° suggest that much of the terrain poleward of this latitude on Titan is saturated with methane. Additionally, Titan's largest sea, Kraken Mare, extends down to ∼55-60°N; and lake units in the north are observed primarily poleward of 65°N with very few observations equatorward of that latitude (Stofan et al., 2007; Hayes, 2016)[56, 52], and have been argued to be hydraulically connected (Hayes et al., 2008; Hayes et al., 2017)[57, 63]. Setting axisymmetric, inexhaustible methane reservoirs poleward of any latitude (in addition to enforcing

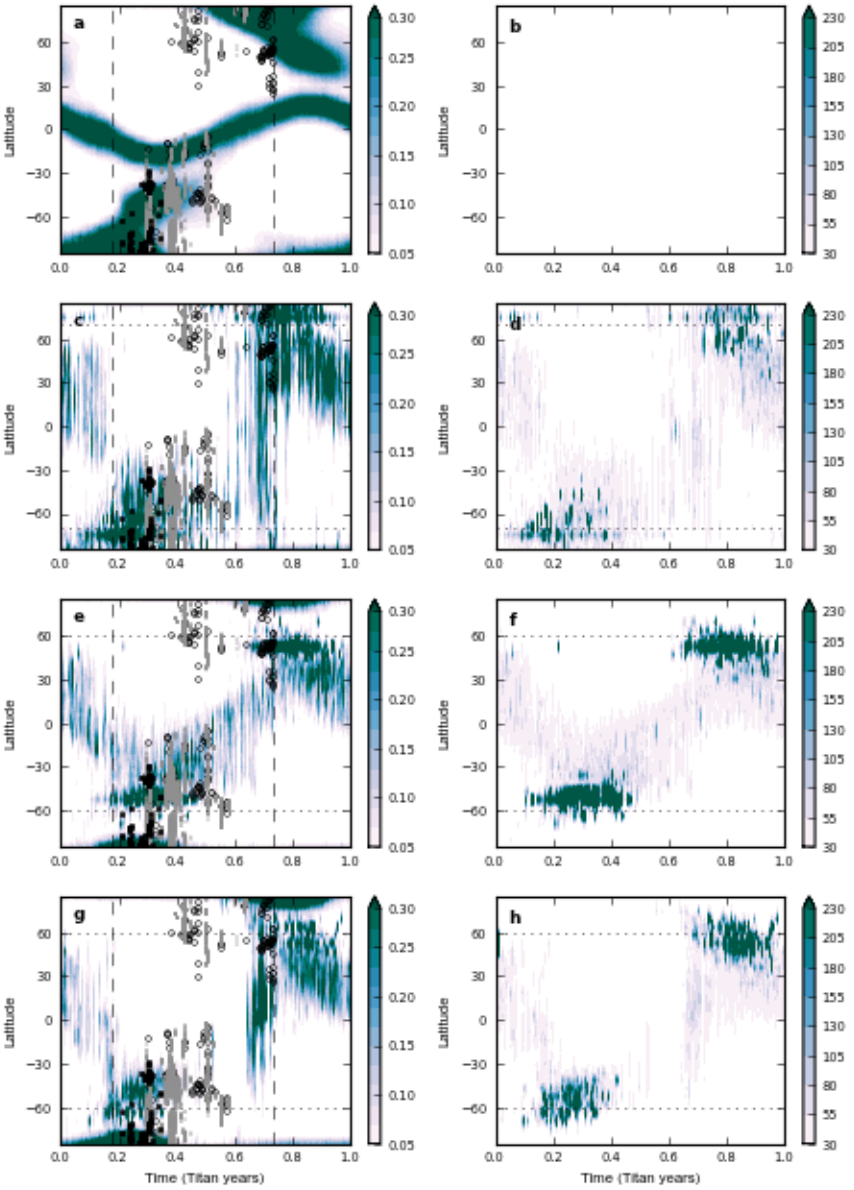

Figure 3.9: **Seasonal methane precipitation for sensitivity experiments**. Zonal and maximum zonal maximum precipitation, as in Fig. 3.1 of main text, for 50 Titan years of the: a,b) aquaplanet simulation, c,d) reduced wetlands simulation, e,f) zero orbital eccentricity simulation, and g,h) control wetlands simulation. Horizontal dotted lines represent wetlands boundaries, while vertical dashed lines represent the era of Titan cloud observations.

infiltration equatorward of the mid-latitudes) makes our simulations idealized, but the 60° boundary is the most justified given observations of Titan's polar regions to date.

3.5.3 Zero orbital eccentricity simulation

In the last additional experiment, we test the sensitivity of our results to variable climate configurations by running the wetlands simulation (with a 60° boundary) with zero orbital eccentricity. We find that the high-magnitude mid-latitude storms still exist in the zero orbital eccentricity experiment (Figs. 3.7, 3.9) and overall the regional precipitation patterns look similar, with substantial low-magnitude precipitation occurring at the poles and medium-magnitude precipitation in the dunes and low latitudes. Additionally, the zonal peakedness profile exhibits the same mid-latitude peaks as under the control insolation forcing, and, as expected, displays symmetry in the low latitudes (Fig. 3.8). This indicates that climate change over long timescales, due to the eccentricity, obliquity, and precession perturbations that comprise Milankovitch cycles, does not substantially affect our findings. In the climate configuration used in this study, wherein southern summer is stronger (as it is for present-day Titan, as described in Aharonson et al. (2009)[58] and Lora et al. (2014)[59]), the distribution of high-magnitude precipitation events in the high mid-latitudes is essentially symmetric about the equator. Thus, even under the varying insolation forcings of Titan's paleoclimate, mid-latitude storms remain intense and provide the potential for considerable geomorphic work, such as that necessary to create alluvial fans through deposition over millions of years.

In summary, when considering all the additional experiments, our results—specifically correlations with observed clouds and alluvial fans—are common to the wetlands configuration and are robust within that configuration. The aquaplanet setting simulates a continuous band of zonal precipitation throughout the year (Mitchell and Lora, 2016)[38] (Fig. 3.9) not seen in cloud observations (Roe, 2012)[1], and additionally does not drive storms capable of erosion (Fig. 3.7). Within the wetlands configuration, meanwhile, the existence of extreme mid-latitude storms is insensitive to climate forcings and is only moderately impacted by

adjustments to the wetlands boundary (Figs. 3.7, 3.8, 3.9).

3.6 Baroclinic storms

The rare, variable, high-magnitude storms in the high mid-latitudes are likely caused by baroclinic instabilities driven by temperature gradients across the wetlands boundary (Lora and Mitchell, 2015)[43]. Indeed, NE-SW tilted specific humidity anomalies indicate propagating near-surface storm fronts in the high mid-latitudes (Fig. 3.10). Evaporative cooling of surface liquids poleward of 60° enhances surface temperature gradients across the wetlands boundaries, which provide the energy for these baroclinic storms (Lora and Mitchell, 2015; Mitchell and Lora, 2016)[43, 38]. Comparing Titan to Earth, we find that Titan's precipitation variability is overall higher than Earth's (see previous subsection on stretched exponential distribution function), in agreement with Titan's potential for more violent storms and with potential implications for a more humidified greenhouse Earth (Lorenz et al., 2005)[10].

To investigate the nature of extreme baroclinic storms in the mid-latitudes, we restarted the TAM wetlands simulation with 1-Earth-day output periods (rather than 10 Earth days), beginning 8000 Earth days into the 50th Titan year and ran for 1000 Earth days. This period of time approximately covers the height of northern summer solstice. A time series of nonzero precipitation events during a large storm event covering multiple grid cells within this time period (Fig. 3.10a) shows that an average precipitation up to 600-700 mm d^{-1} can occur during a single 1-Earth-day output period.

The precipitation event shown in Fig. 3.10 is typical of the intense high mid-latitude storms in our model. These can last on the order of tens of Earth days and accumulate nearly a meter of methane per day during that time. In addition, they can extend across several grid spaces, as shown by the contour in Fig. 3.10b. These methane accumulation rates and substantial storm parameters are comparable to previous calculations (Lorenz et al., 2005)[10] and consistent with observations (Tokano et al., 2006)[51] that the atmospheric column on Titan contains several meters of methane. Results from simulations of local

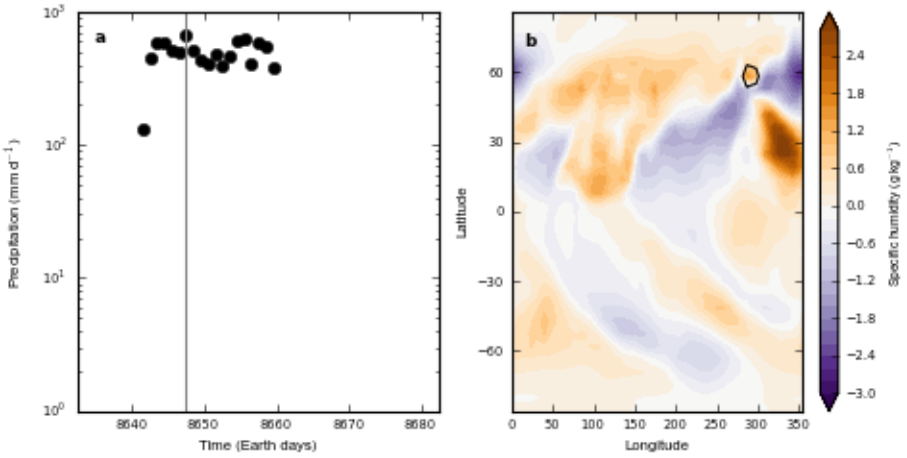

Figure 3.10: **Connection between extreme precipitation and baroclinic storm front**. a) Time series of nonzero precipitation events at 60°N during northern summer of the 50th Titan year of the TAM wetlands simulation restarted with 1-Earth-day output periods. Vertical grey line indicates time during which snapshot on right panel was taken. b) Snapshot of the low-level zonally asymmetric component of specific humidity (g/kg) during northern summer solstice of the 50th Titan year of the TAM wetlands simulation. The black contour shows the line of 100 mm d^{-1} precipitation, where precipitation inside the contour is greater than 100 mm d^{-1}.

deep convective storms on Titan (Barth and Rafkin, 2010; Rafkin and Barth, 2015)[6, 13] also demonstrate comparable methane accumulation rates. At their most extreme, under certain wind and temperature conditions, these simulated storms can be long-lived (>24 hours), propagate over 1000 kilometers (about the length of several grids in our model), and rain out over 100 meters of methane (Rafkin and Barth, 2015)[13]. More conservative estimates (Hueso and Sánchez-Lavega, 2006; Barth and Rafkin, 2007)[11, 5] of storm methane accumulation are closer to 100 kg m^{-2}, which is less than a quarter of a meter in columnar height, but are still of the same order of magnitude as our results.

3.7 Implications for climate-surface feedbacks and conclusions

To summarize, precipitation data from TAM "aquaplanet" simulations, i.e. initialized with a global methane ocean, do not show the same strong correlations with observed clouds and geomorphologic landforms as the climatic patterns from our wetlands simulations. In particular, aquaplanet simulations lack high-magnitude mid-latitude storms, exhibit minimal differences in regional storm variabilities, and produce low rainfall magnitudes and frequen-

cies inconsistent with global fluvial erosion (Figs. 3.7, 3.8). On the other hand, wetlands simulations robustly produce high-magnitude baroclinic storms and variability peaks in the high mid-latitudes—with only slight dependencies on the latitude of the wetlands boundaries (Figs. 3.7, 3.8, 3.9)—consistent with the observed alluvial fan distribution. Thus, when compared to aquaplanet settings, the wetlands surface liquid configuration used in this study is more congruent with observations and illustrative of Titan's regionally-varying hydroclimate.

Ongoing model development to incorporate topography and surface hydrology, which is idealized in these simulations, will shed further light on moisture transport processes and surface connections. The roles of Titan's unconstrained surface composition and processes in sedimentary transport and deposition, however, remain unclear. Potentially thick megaregolith and aeolian deposition at lower latitudes (Howard et al., 2016; Birch et al., 2016; Cartwright and Burr, 2017)[222, 82, 84] and soluble, karstic material near the poles (Cornet et al., 2015)[220] may prove inhibitory to fan formation, independent of hydrologic factors. The extent to which surface material properties are themselves tied to local hydroclimate is also unclear—sedimentary material in the polar regions, for example, could stem from the abundance of liquid methane there (Hayes, 2016; Birch et al., 2017b)[52, 121], imposing a dynamic between climate and sedimentology that would influence the geomorphology in complex ways.

Despite these uncertainties and the current model's limitations, our regional estimates for storm magnitude, frequency, and variability strongly correlate with observed distributions of surface features, provide a better understanding of Titan's regionally-varying hydroclimate, and suggest that active geomorphic work is ongoing in Titan's present climate. Further and more detailed observation of geomorphic features, combined with continued precipitation analysis from models, will potentially reveal new archives of Titan's paleoclimate, with implications for comparative planetology given the similar geomorphic responses to climate-driven changes on other terrestrial bodies such as Earth and early Mars.

CHAPTER 4

Surface Hydrology on Titan

The following is in prep to be submitted to *Nature Communications*, *Icarus*, *JGR*, or a similar journal in May 2018.

4.1 Introduction

Terrestrial land models incorporating surface hydrology prescriptions are proven tools for understanding hydroclimatic relationships and water-resource impacts (e.g. Manabe, 1969; Chen and Dudhia, 2001, etc.)[227, 228]. When coupled to general circulation models (GCMs) of the atmosphere, these land models can more accurately describe the fate of regional rainfall, which may runoff into drainage basins or infiltrate into subsurface aquifers. Tropical rain on Earth saturates equatorial latitudes, for instance, and rivers generally drain from higher elevation continental interiors into the ocean. Planetary surfaces other than Earth are noticeably impacted by surface hydrology as well: Mars exhibits widespread valley networks indicative of a wetter past, with a global topography dominated by ancient lowlands and the Tharsis volcanic rise (e.g. Smith et al., 1999)[229]; Titan bears extensive fluvial and lacustrine features, with a global topography defined by low-latitude highlands and polar lowlands (e.g. Lorenz et al., 2013)[88]; even Venus and Pluto show signatures of topographically-controlled volcanic (Ford and Pettengill, 1992; Smrekar et al., 2010)[230, 231] or glacial flow (e.g. Moore et al., 2016)[232]. On Mars and Titan, large-scale topography drives drainage patterns more so than on Earth (Black et al., 2017)[123], which is heavily shaped by small-scale tectonic changes that divert rivers (Willett et al., 2014)[233]. Our climatic understanding of planetary bodies such as Mars and Titan would therefore benefit from land

models coupled to GCMs at coarse resolutions that capture large-scale topographic structure and the resulting large-scale climate dynamics.

Titan's hydroclimate appears especially driven by large-scale topography given the coincidence of active drainage (Wall et al., 2010; Langhans et al., 2012; Burr et al., 2013a)[62, 80, 81], erosional modification (Neish and Lorenz, 2014; Neish et al., 2016)[90, 91] and stable lacustrine features (Stofan et al., 2007; Hayes et al., 2008; Hayes, 2016)[56, 57, 52] in the low-lying polar regions. Persistent solstitial cloud activity (Roe et al., 2002; Bouchez and Brown, 2005; Porco et al., 2005)[17, 18, 21] and substantial near-surface humidity levels (Lora and Ádámkovics, 2017)[136] concentrated at the poles further indicate a broadly dichotomous world split into two climate zones, namely the dry low latitudes and moist high latitudes (Mitchell and Lora, 2016)[38]. GCMs have successfully reproduced this basic climatic structure, showing that the atmospheric circulation dries out the low latitudes and transports methane poleward (Rannou et al., 2006; Mitchell et al., 2006; Mitchell, 2008; Schneider et al., 2012; Lora et al., 2015; Newman et al., 2016)[137, 30, 138, 98, 99, 100], but the extent to which surface hydrology contributes to or alters such transport is unclear. None of the above GCMs employ a physically realistic representation of surface hydrology that would account for overland flow, as suggested by evidence of erosion and sediment transport from fluid runoff following precipitation events (Perron et al., 2006; Jaumann et al. 2008; Black et al., 2012; Birch et al., 2016; Faulk et al., 2017b)[92, 93, 94, 82, 155], or for subsurface interactions, as suggested by putative shoreline changes and surface alterations (Hayes et al., 2011; Turtle et al., 2011b; Turtle et al., 2011c)[234, 29, 235], geomorphological mapping indicating local hydraulic connectivity (Hayes et al., 2017)[63] and saturated sediments (Birch et al., 2017b)[121], and low-level humidity measurements implying methane reservoirs in excess of observed surface liquids (Lora and Ádámkovics, 2017)[136].

This vast collection of observations bespeaks a surface on Titan as hydrologically rich and complex as its atmosphere. With the exception of one large lake called Ontario Lacus (e.g. Turtle et al., 2009)[61], the south polar region is conspicuously dry, featuring broad empty paleobasins while the north polar region maintains extensive lake districts and large maria (Hayes, 2016; Birch et al., 2017a)[52, 64]. Preferential methane buildup in the north has been

shown to be a consequence of Saturn's orbital configuration (Aharonson et al., 2009; Lora et al., 2014)[58, 59] and has been demonstrated in previous GCMs (Schneider et al., 2012; Lora et al., 2015; Lora and Mitchell, 2015)[98, 99, 43], but again, contributions from surface hydrology remain unknown. Despite the hemispheric asymmetry, vigorous south polar cloud activity occurred during southern summer (e.g. Roe et al., 2002)[17], suggesting potential subsurface reservoirs capable of groundmethane evaporation. Recent models have begun to consider simple hydrology schemes for Titan (Mitchell, 2008; Schneider et al., 2012; Lora et al., 2015; Lora and Mitchell, 2015; Horvath et al., 2016)[138, 98, 99, 43, 139], but they have ignored key features like topography, finite infiltration rates, and surface-atmosphere coupling. Among these is an iteration of the Titan Atmospheric Model (TAM; Lora et al., 2015)[99] that imposed low-latitude infiltration and inexhaustible high-latitude reservoirs to effectively force a polar wetlands climate (Lora and Mitchell, 2015)[43]. Hereafter referred to as "TAM wetlands", this simulation is among the most consistent with observations (Lora and Mitchell, 2015; Faulk et al., 2017b)[43, 155], but remains problematic because it enforced rather than predicted Titan's observed climate.

In this chapter, we present a new version of TAM that includes simple and modular parameterizations of overland surface flow, infiltration, subsurface flow, and groundmethane evaporation (Fig. 4.1 shows a schematic of the model processes). Fully coupled to the atmosphere in a three-dimensional GCM with a complete physics package, these components allow methane to self-consistently distribute itself within the climate system according to moisture availability and topography information (topography in our model does not interact directly with the atmosphere via orographic effects). We evaluate the climatic evolution promoted by surface hydrology additions by comparing simulated results to observations and by examining the partitioning of global moisture transport, following previous GCM studies (Lora and Mitchell, 2015; Mitchell and Lora, 2016)[43, 38].

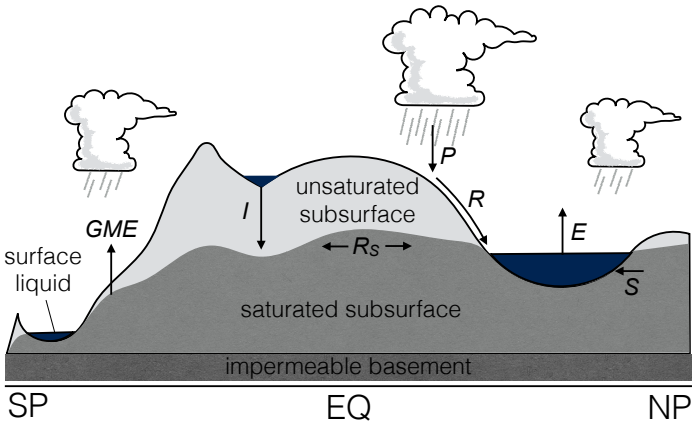

Figure 4.1: **Surface hydrology model**. A schematic of the surface hydrology components and processes incorporated into TAM in this study. Shows a representative longitude slice, with unsaturated low-latitude highlands and saturated high-latitude lowlands. Light grey represents unsaturated subsurface, grey represents methane table, and dark grey represents impermeable basement. Dark blue represents surface liquid. Transport processes include groundmethane evaporation (GME), infiltration (I), horizontal subsurface flow of the methane table (R_s) and its special case of outcropping onto the surface (O), precipitation (P), surface runoff (R), and evaporation (E). *Note that the unsaturated subsurface is not a reservoir and does not contain liquid.

4.2 Methods

4.2.1 TAM

The Titan Atmosphere Model (TAM) is a three-dimensional GCM based on the Geophysical Fluid Dynamics Laboratory spectral dynamical core that has been benchmarked against a variety of observations of Titan's atmosphere and seasonal methane cycle (Lora et al., 2015)[99]. The model includes a complete physics package, including a fully nongray radiative transfer code, a simplified parameterization of moist convection (Frierson et al., 2007)[140], large-scale condensation, a simplified saturation vapor pressure scheme (Lora and Ádámkovics, 2017)[136], and bulk aerodynamic surface fluxes, and thermal diffusion through the soil (see Chapter 1 of this dissertation for more information). The hydrology additions to TAM used in this chapter are described below.

4.2.2 Surface hydrology

Liquid methane is always in one of three reservoirs: the surface reservoir; the runoff reservoir; or the subsurface reservoir. The surface reservoir therefore represents the lakes and seas of Titan's hydrosphere, as sourced by precipitation and runoff. The runoff reservoir refers to the liquid methane that is "in transit," or flowing along topographic gradients, thus representing the river channels and flow networks on Titan's surface. Methane in the runoff reservoir is not available for evaporation. And the subsurface methane table reservoir refers to the liquid methane stored underground, representing Titan's saturated zone. In the following, we describe the steps of the surface hydrology scheme in the order that they occur.

4.2.2.1 Evaporation and infiltration

The first action to occur every timestep is the addition of the net accumulation of methane to the grid cell, given by the difference between precipitation and evaporation. Evaporation is calculated normally (i.e. via bulk aerodynamic formulae) except for where the surface falls below $h_{th,evap}$ (see Table 4.1 for all control values), in which case evaporation from

the subsurface reservoir proceeds, constituting groundmethane evaporation. Based on the terrestrial literature (Philip, 1957; Shah et al., 2007; Johnson et al., 2010)[236, 237, 238], groundmethane evaporation falls off exponentially with depth to the table such that $GME = E * exp[A * (h - z)]$, where z is the topography, h is the methane table height, E is the evaporation of a wet surface as calculated normally by bulk aerodynamic formulae, and A is a specified constant.

Thus, even when the surface reservoir is empty but the subsurface methane table reservoir is close to the surface, evaporation can occur, removing methane directly from the methane table (evaporation occurs as normal if the methane table is deep below the surface but there is perched surface liquid above $h_{th,evap}$). Terrestrial groundwater evaporation profiles vary widely and are strongly influenced by vegetation (Kurc and Small, 2004; Shah et al., 2007)[239, 237]. The extinction depth, defined as the depth where groundwater evaporation vanishes, is typically 1-5 meters in terrestrial settings, tending closer to 1 m for bare soil in arid desert regions devoid of vegetation, such as those in the Chilean desert (Johnson et al., 2010)[238]. In all simulations with subsurface effects, we set A=1 to attain an e-folding depth of 1 m, comparable to typical terrestrial groundwater evaporation profiles in arid and semiarid terrains. Precipitation and evaporation are calculated independently of the runoff reservoir.

We additionally include a vertically resolved soil model of 10 layers of variable thickness (with the deepest layer reaching ∼70 m below the surface) wherein heat is transported via conduction (Lora et al., 2015)[99]. The thermal properties of this soil match those of the "porous icy regolith" described in Tokano (2005)[9]. We consider the effect of subsurface methane saturation on the soil temperature by adjusting the thermal conductivity α and heat capacity c_v at a given depth according to whether the methane table has reached that depth. For saturated soil at a given depth z, $c_v(z) = \Delta z(z) * [c_{v,reg} * (1 - \eta) + c_{v,liq} * \eta]$ and, similarly, $\alpha(z) = \alpha_{reg} * (1 - \eta) + \alpha_{liq} * \eta$, where Δz is the layer thickness and η is the porosity.

If after evaporation the surface liquid is above $h_{th,hydro}$, infiltration occurs at the specified hydraulic conductivity K, set in our control simulations at 10^{-4} m s^{-1}, which represents the high end of hydraulic conductivity estimates for Titan (Hayes et al., 2008; Hayes et al., 2011;

Parameter	Explanation	Control value
K	Vertical hydraulic conductivity	10^{-4} m s^{-1}
D	Methane table flow coefficient	10^{-6}
	(corresponding horizontal hydraulic conductivity)*	$\sim 10^{-6}$ m s^{-1}
$h_{th,hydro}$	Infiltration/runoff threshold	2 x 10^{-2} m
L	Basin catchment length	1.5 x 10^{5} m
A	Groundwater evaporation scaling parameter	1.0
$h_{th,evap}$	Evaporation threshold	2 x 10^{-6} m
η	Porosity	0.5
ρ	Density of liquid	450 kg m^{-3}
n	Number of surface layers	10
α_{reg}	Thermal conductivity of porous icy regolith	0.1 W m^{-1} K^{-1}
α_{liq}	Thermal conductivity of liquid	0.3 W m^{-1} K^{-1}
$c_{v,reg}$	Volumetric heat capacity of porous icy regolith	1.12 x 10^{6} J m^{-3} K^{-1}
$c_{v,liq}$	Volumetric heat capacity of liquid	1.8 x 10^{6} J m^{-3} K^{-1}

Table 4.1: **Complete hydrology parameter list**. See text for full description of surface hydrology scheme. The parameters we vary in our simulations are the first two parameters, K and D. *Approximation of horizontal subsurface hydraulic conductivity is described in text.

Horvath et al., 2016)[57, 234, 139]. The threshold $h_{th,hydro}$ is set at 2 cm in all simulations to represent the initiation of broad-scale runoff and infiltration following large storm events (Cammeraat, 2004)[240]. Infiltration on Earth generally occurs at the expense of runoff for storm events, so we execute infiltration before runoff in our model (additional simulations show that a reversal of the infiltration-runoff computation order, as well as adjustments to the threshold $h_{th,hydro}$, lead to negligible changes in the resulting climate). Infiltration in our model occurs anywhere on the globe where the subsurface is unsaturated; and for simplicity, infiltrated methane is immediately added to the methane table, regardless of the depth to the table.

4.2.2.2 Runoff

If after infiltration surface liquid remains above $h_{th,hydro}$, we allow horizontal movement to the cell of steepest descent (O'Callaghan and Mark, 1984; Tarboton, 1997)[241, 242]. Single flow direction methods in an eight-point grid system enable convergent flow over topography in a fashion that closely approximates downslope flow; in addition, single flow

direction methods are more suitable to representing channel properties in coarse-resolution terrains when compared to multiple flow direction methods (Freeman, 1991; Shelef and Hilley, 2013)[243, 244].

Runoff is determined based on each grid cell's potential ϕ in meters, where ϕ is the combination of the geoid-corrected topography (Corlies et al., 2017)[89] and the surface liquid height. If the potential of a given cell is higher than any one of its eight neighbors, liquid is removed from the surface reservoir of that cell and added to the runoff reservoir of the cell of steepest descent, i.e. the cell with the steepest potential gradient $\frac{d\phi}{dl}$ where dl is the centered finite difference distance between the two cells. Any liquid currently in the given cell's runoff reservoir is moved to the runoff reservoir of the cell of steepest descent as well. We ignore meandering and unevenness at the subgrid scale. For cells at the highest possible latitude, the three poleward neighboring cells are considered to be the three cells at the same latitude but directly across the pole from the cell in question. We thus assume that the distance between a cell and the one directly across from it on the polar circle is equal to twice the difference between the cell and the pole itself.

Following Horvath et al. (2016)[139], we calculate the runoff flow rate using a form of the linear reservoir approximation, which assumes that the amount of surface runoff is linearly related to the amount of liquid stored in the catchment (Overton, 1970; Watt and Chow, 1985; Liston et al., 1994; Miller et al., 1994; Coe, 2000; Wang et al., 2011)[245, 246, 247, 248, 249, 250] such that $S = k_s Q$. The storage S is the amount of methane in the surface reservoir in kg m^{-2}. We take the coefficient k_s that relates flow Q to storage S to be equal to half the concentration time t_c (Overton, 1970; Liston et al., 1994; Horvath et al., 2016)[245, 247, 139], which is defined as the amount of time it takes a parcel of liquid to travel the distance of a catchment.

For large terrestrial catchment basins, $t_c = 0.000326(\frac{L}{S_0^{0.5}})^{0.79}$ hrs (Watt and Chow, 1985)[246], where L is the length of the catchment in meters and S_0 is the slope. Since basin concentration time decreases with increasing slope, flow is therefore dependent on topographic slope and available methane storage. We consider each grid cell to be a "basin," and assume a constant L of 150 km, the approximate median length of channels observed

in the polar regions on Titan (Burr et al., 2013a; Horvath et al., 2016)[81, 139] and an intermediate length scale for grid cells in our model at T21 resolution (roughly 5° horizontal resolution). We take S_0 to be the steepest potential gradient $\frac{d\phi}{dl}$. To modify this terrestrial approximation for Titan, we must scale the concentration time by a factor of $\mu/\rho g$ (where μ is the dynamic viscosity and ρ is density of liquid), since velocity is proportional to the ratio of gravity to kinematic viscosity and flow time is inversely proportional to velocity (Horvath et al., 2016)[139].

All together, this approximation gives concentration times between 1–20 days, comparable to basin lag times in terrestrial models (Askew, 1970; Singh, 1988; Vorosmarty et al., 1989; Liston et al., 1994)[251, 252, 253, 247]. Corresponding runoff rates therefore span several orders of magnitudes, ranging from 10^{-6}–10^{-2} kg m^{-2} s^{-1}, which are typically one or more orders of magnitude greater than evaporation changes when runoff occurs. To ensure smooth flow, the maximum runoff allowed from one cell to its destination cell is equal to half of the potential difference between the two cells. Note that given Titan's poorly constrained surface materials, basin geometry, and methane flow characteristics, calculating discharge using standard terrestrial methods is not straightforward (Burr et al., 2013a)[81]. Thus, concerning the parameterization of runoff speed, the crucial element to capture is that runoff is "fast" compared to evaporation when there are substantial liquid amounts, which our linear reservoir approximation achieves.

After the removal of surface liquid and the movement of runoff reservoir liquid are calculated for each grid cell, the return flow back to the surface reservoir is determined. The liquid in a given cell's runoff reservoir returns to that cell's surface reservoir under the following two conditions: 1) if the methane table at a given grid cell is below the topography but the grid cell lies at a local depression in potential ϕ (including both topography and surface liquid height); and 2) if the methane table at a given grid cell has reached the surface. The second condition is meant to simulate flow to a potentially large mare that immediately becomes available for evaporation at the shoreline. The fact that liquid in the runoff reservoir returns to the surface reservoir wherever the subsurface is saturated—regardless of whether the grid cell is at a local depression—implies that there may temporarily be a higher surface liquid

height at the shoreline than at the lake's center after the return flow is added. However, any potential difference will be again removed from the surface reservoir in the form of runoff and eventually make its way towards the center of lowest potential during subsequent timesteps. Buildup of methane at any one grid cell is prevented by the fact that runoff is calculated based on the potential of both the topography and the surface liquid height.

4.2.2.3 Subsurface transport

We refer to the subsurface reservoir as always below ground; however, where the soil is completely saturated, the effective height of the methane table then reaches above ground, and includes contributions from both the saturated subsurface reservoir and the surface reservoir. The height of the methane table is measured relative to the topographic minimum. Differences in the methane table height are then used to calculate horizontal adjustments to the methane table. In contrast to the surface runoff scheme, we use a multiple flow direction method such that liquid flows to multiple cells of lower potential rather than to the cell of steepest descent alone. Multiple flow direction methods in grid-based hydrologic models are prevalent in the terrestrial literature (Quinn et al., 1991; Freeman, 1991; Shelef and Hilley, 2013)[254, 243, 244], including for subsurface flow (Wigmosta et al., 1994; Wigmosta and Lettenmaier, 1999)[255, 256].

To calculate flowpaths based on local table slopes in our model, we modify the standard multiple flow direction method developed for overland flow (Freeman, 1991)[243]. Our iterative procedure is as follows: for each cell, 1) determine the cell among the lower potential neighbors with the least steep descent, which has height h_{least}; 2) route $dh = D\Delta t\frac{h-h_{least}}{2Ndl}$ to each of the lower potential neighbors, where h is the height in meters of the cell from which liquid is flowing, Δt is the timestep, N is the number of lower potential neighbors, and D is a specified constant with a unit of length over time; 3) repeat the procedure for the next least steep cell where h is updated to have been lowered by dh as calculated in step 2, and continue, decreasing N by 1 each time, until finishing with the cell of steepest descent. We use $\frac{h-h_{least}}{2Ndl}$ when calculating the flow rate to ensure there is enough liquid to

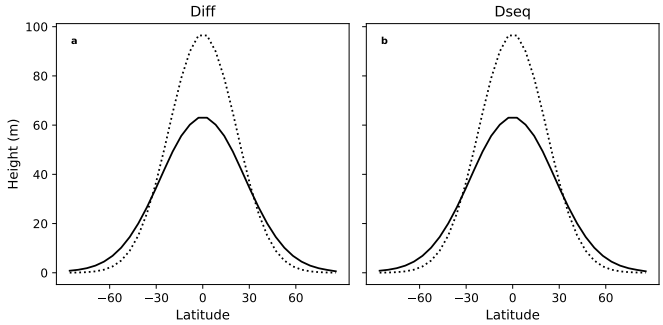

Figure 4.2: **Subsurface transport method**. Evolution of a sample methane table profile from its initial form (dotted black line) to a state 10 Earth days later (solid black line) for: a) the diffusion equation with a constant diffusion coefficient D_{diff}=0.5 m^2 s^{-1}; and b) our method ($Dseq$) with D=1 m s^{-1}. Table was initialized from a three-dimensional gaussian mound centered at 180°E and the equator; panels show longitude slice of 180°E.

repeat the algorithm until transport occurs to the cell of steepest descent alone. Depending on if methane table height adjustments dh are added to surface or subsurface reservoirs, the porosity dictates corresponding methane mass flow amounts. Calculated flow amounts are stored in a temporary array before being added to the reservoirs simultaneously once outflows have been calculated for every grid cell—as such, the order in which grid cell outflows are calculated does not influence flow amounts.

When compared to standard multiple flow direction methods for calculating watershed flowpaths that distribute flow proportionally to slopes (e.g. Freeman, 1991; Wigmosta et al., 1994)[243, 255], our method routes disproportionally more liquid to the cell of steepest descent and less to the cell of least steep descent. It is therefore more representative of the diffusive processes that would likely be active in a subsurface liquid table, as governed by the groundwater flow equation, producing table profiles that flatten smoothly. Indeed, by calculating fluxes in to and out of each cell, the above procedure essentially solves the diffusion equation explicitly. Numerical instabilities from sharp topographic gradients at coarse resolutions prevent us from solving the diffusion equation in spectral space, but our modified procedure clearly enables diffuse flow (Fig. 4.2). Since $\frac{1}{N}\sum_{n=1}^{N}\frac{h-h_n}{dl} \approx \frac{h-h_N}{dl}$, our procedure effectively solves the following equation for the linear velocity of groundwater flow:

$$\frac{dh}{dt} = K_h \frac{dh}{dl} \tag{4.1}$$

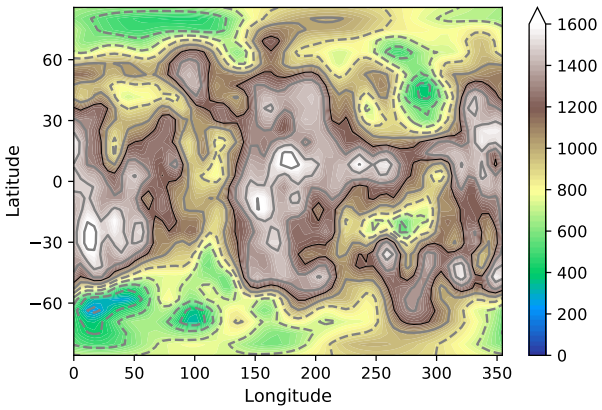

Figure 4.3: **Topography map**. Color contours show global elevation (m) above the topographic minimum from Corlies et al. (2017)[89], interpolated to T21 resolution for our simulations. Grey contours show normalized elevation, with solid lines indicating above-average elevation and dashed lines below-average elevation. Bolded line represents constant equipotential (1200 meters) used to initialize the control simulation.

where the horizontal hydraulic conductivity $K_h = \frac{D}{2}$. Thus, the specified constant coefficient D can be connected to a physical soil parameter that determines the subsurface transport rate. Fig. 4.2 shows the evolution of a sample methane table profile using our method (referred to as $Dseq$), as compared to the evolution of the same methane table profile using the diffusion equation with a constant coefficient equal to $\frac{D}{2}$. The D used in our control simulations, 10^{-6} m s^{-1}, therefore corresponds to a horizontal hydraulic conductivity typical of semi-pervious terrestrial materials, such as compacted sandstones and clays; and being of intermediate permeability, makes for a reasonable approximation for our control simulation.

4.2.2.4 Topography

Throughout the above, topography is used only as an input into hydrology calculations, and is not coupled to the atmosphere. The topography map used in our study is the most recently updated product of Cassini RADAR data (Corlies et al., 2017)[89]. Radar coverage is limited to only 9% of Titan's surface area, so an interpolation is required to generate a full global topographic map. We use the un-smoothed geoid-corrected interpolation of Titan's topography, with the geoid derived from parameters reported by Iess et al. (2012)[257], and further interpolate to T21 resolution for use in our simulations (Fig. 4.3). Thus, basins in

Simulation	K [m s^{-1}]	D [m s^{-1}]	Notes
Control	10^{-4}	10^{-6}	a) consistent with cloud observations b) minimal mid-latitude surface liquid
Low sub. transport	10^{-4}	10^{-7}	a) precip. shutdown in low latitudes b) losing surface liquid to low-latitude subsurface
High sub. transport	10^{-4}	10^{-5}	a) nearly continuous tropical rain band b) gaining surface liquid from low-latitude subsurface
Low infiltration	10^{-8}	10^{-6}	a) consistent with cloud observations b) strong surface transport; gaining surface liquid
Runoff	0.0	0.0	a) consistent with cloud observations; b) buildup in mid-latitude basins

Table 4.2: **Simulation descriptions**. The 'Notes' column briefly summarizes main takeaways related to a given simulation's a) precipitation distribution and b) surface liquid distribution. All parameters other than K and D are set to the control values, as specified in Table 4.1. See Methods for further description of surface hydrology scheme.

our topography do not exactly coincide with the observed basins. Nevertheless, given our interest in large-scale climate dynamics, the approximate correlation is suitable for our purposes.

4.2.3 Experimental setup

We run all simulations at T21 resolution (64 longitude grids by 32 latitude grids, giving a roughly 5° horizontal resolution) with 32 atmospheric vertical layers and a timestep Δt of 600 seconds, starting from an already spun-up atmosphere. For the control simulation, we begin with liquid methane up to an equipotential surface of 1200 meters relative to the topographic minimum. We keep the surface dry, such that the subsurface is completely saturated wherever the topography is below 1200 meters (see Fig. 4.3). Surface and subsurface reservoirs stabilize in the control simulation after 60 Titan years. Sensitivity simulations with varying parameter values (Table 4.2) are branched off after 60 Titan years and run for an additional 15 Titan years. A "runoff" simulation with only surface overland flow and no subsurface effects is run independently for 75 Titan years and included in our analysis. For the runoff simulation, we begin with a surface liquid methane reservoir that is globally five meters deep and consider the subsurface unsaturated when calculating surface thermal parameters.

4.3 Basic climate state

4.3.1 Precipitation

Without resolving clouds in our model, we rely on precipitation metrics to benchmark against cloud observations, with the inherent assumption that clouds are linked to precipitation. With that in mind, the zonal mean precipitation distribution of the control simulation (Fig. 4.4a) shows that the model captures the essential aspects of Titan's hydrologic cycle: abundant rain blankets the solstitial poles, while scattered storms populate the lower latitudes. The rain profile is similar to that of the TAM wetlands simulation, which imposed

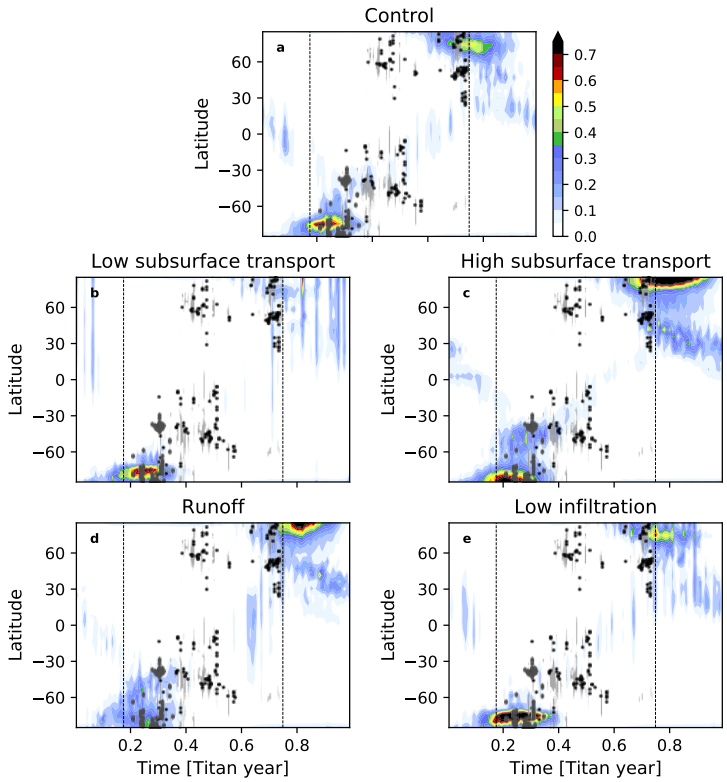

Figure 4.4: **Seasonal precipitation distributions with cloud observations**. Zonally averaged precipitation (mm d^{-1}) composited over the final five Titan years of: a) the control simulation; b) the low subsurface transport simulation; c) the high subsurface transport simulation; d) the runoff simulation; and e) the low infiltration simulation. Precipitation profiles are compared to tropospheric cloud locations (Roe et al., 2005; Bouchez and Brown, 2005; Schaller et al., 2006; Rodriguez et al., 2011; Turtle et al., 2011a; Turtle et al., 2017)[22, 18, 19, 27, 31] as observed by ISS (black circles), VIMS (grey circles), and ground-based telescopes (dark grey diamonds). Vertical dashed lines represent era of Titan cloud observations, extending from late 2001 to late 2017.

low-latitude infiltration and deep high-latitude reservoirs and strongly reproduced cloud observations from Cassini instruments and ground-based telescopes (Mitchell and Lora, 2016; Faulk et al., 2017b)[38, 155]. The control simulation maintains mid-latitude precipitation activity throughout the solstice-equinox transition, in closer agreement with cloud observations (Rodriguez et al., 2011)[27] and improving upon the TAM wetlands simulation that featured a sharp break in precipitation activity at the end of southern summer (a break that occurs in the runoff simulation as well; see Fig. 4.4d).

Sensitivity simulations robustly reproduce zonal precipitation profiles consistent with

cloud observations (Fig. 4.4). The only exception is the low subsurface transport case, wherein liquid becomes trapped in the deep low-latitude subsurface (see following sections for further discussion), shutting off lower latitude precipitation (Fig. 4.4b). In general, as expected from previous studies demonstrating the hydrologic cycle's dependence on surface liquid distribution (e.g. Mitchell, 2008; Lora et al., 2015; Newman et al., 2016)[138, 99, 100], more rain occurs in simulations with more available surface liquid. This is particularly apparent in the high subsurface transport simulation, wherein abundant surface liquid becomes available to evaporate into the atmosphere and promote rain at nearly all latitudes, with notably excessive southern mid-latitude rain during solstice compared to observations (Fig. 4.4c). Such a regime features a nearly continuous band of seasonal rain, analogous to Earth's intertropical convergence zone and also reported in previous Titan models with globally wet surfaces (Mitchell et al., 2006; Lora et al., 2015; Newman et al., 2016)[30, 99, 100]. This rain band is not as prominent in the low infiltration case, however, presumably because overland flow more effectively localizes surface liquid whereas subsurface transport provides diffuse saturation (see Fig. 4.12 for surface liquid accumulation maps). The zonal rain distribution of the low infiltration case exhibits strong solstitial rain in the south and more equinoctial breaks in convective activity, similar to the runoff simulation and in further indication of surface liquid localization that might reduce storm activity.

4.3.1.1 Extreme mid-latitude storms

TAM wetlands simulations exhibit rare, intense storms in the mid-latitudes that correlate with observed geomorphic features in those regions (Faulk et al., 2017b; Chapter 3)[155]. These storms have been proposed to be baroclinic eddies, driven by temperature gradients that are enhanced by evaporative cooling at high latitudes (Lora and Mitchell, 2015; Mitchell and Lora, 2016; Faulk et al., 2017b)[43, 38, 155]. Dry general circulation models have also produced high mid-latitude storms consistent with baroclinic eddies (Lebonnois et al., 2012)[225], suggesting that mid-latitude baroclinic instability may be a fundamental feature of Titan's climate.

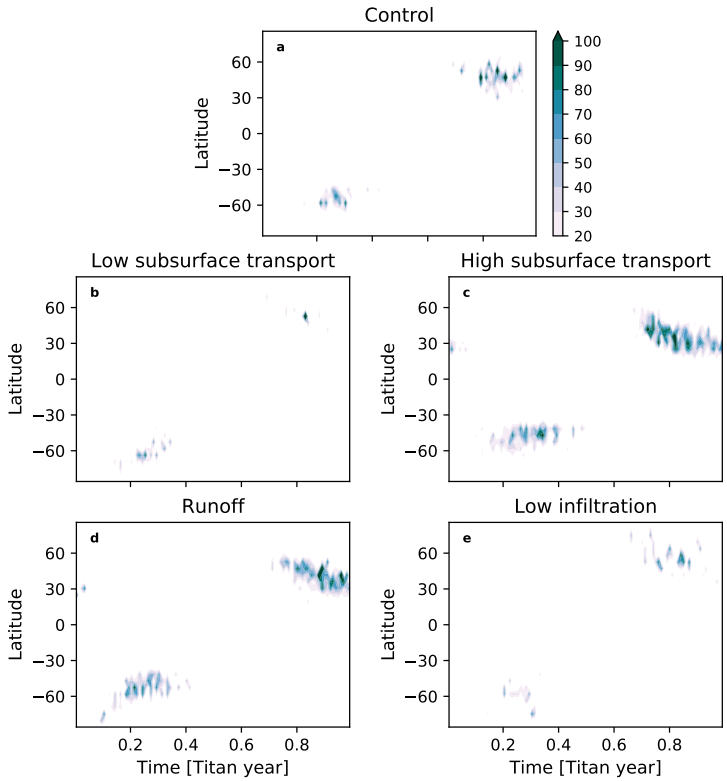

Figure 4.5: **Extreme precipitation events**. Maximum zonal maximum precipitation (mm d^{-1}) taken over the final 15 Titan years of each simulation, with panels the same as Fig. 4.4, calculated by taking the zonal maximum at a given time and latitude for each of the 15 Titan years and then selecting the maximum of those 15 values to construct the contours.

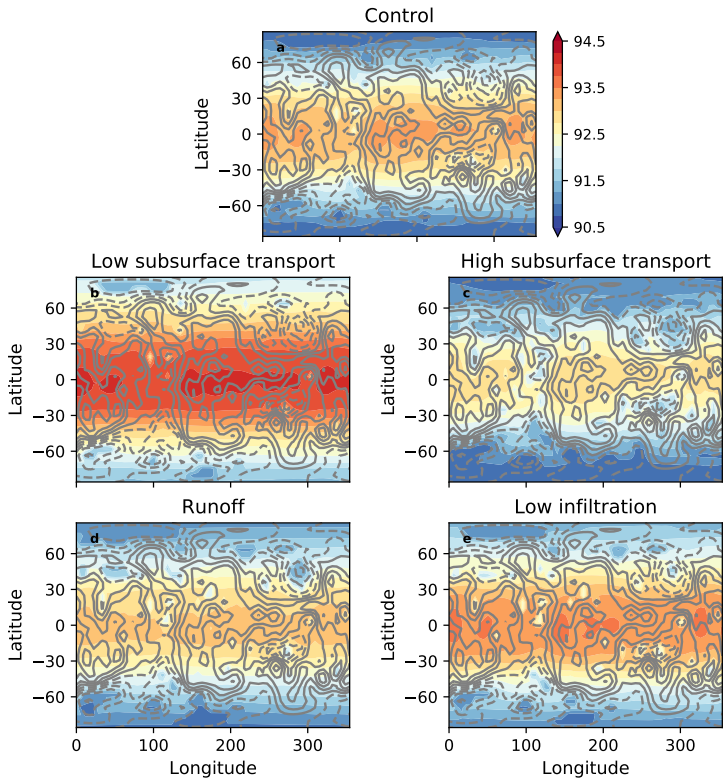

Figure 4.6: **Surface temperature maps**. Surface temperature (K; color contours) averaged over the final five Titan years of each simulation, with panels same as in previous figures. Grey contours show normalized topography (Corlies et al., 2017)[89] interpolated to T21 resolution, as in Fig. 4.3, with solid lines indicating above-average elevation and dashed lines below-average elevation.

Recreating wetlands climates, the simulations in our study generally exhibit the same extreme precipitation behavior, with the most extreme precipitation events over the last 15 Titan years of each simulation occurring in latitudes 50–70° (Fig. 4.5). Surface temperature maps show that temperature gradients are established across the mid-latitudes in each simulation (Fig. 4.6). These temperature gradients may therefore be responsible for providing the energy needed to generate the mid-latitude storms seen in our simulations.

4.3.2 Surface liquid

The surface liquid distribution (Fig. 4.7a) in the control simulation is also congruent with the observed lake distribution (Stofan et al., 2007; Hayes et al., 2008; Hayes, 2016)[56, 57, 52]. Major seas fill the polar basins associated with the observed maria in the northern hemi-

sphere (at ∼50–100°E) and Ontario Lacus in the southern hemisphere (at ∼150–180°E). Mid-latitude basins (see Fig. 4.3), such as at ∼60°W in the north and ∼25°E in the south, have not been observed by Cassini to contain surface liquid, and in the dry southern hemisphere have been interpreted as paleoseas (Hayes et al., 2016; Birch et al., 2017a)[52, 64]. The control simulation has markedly reduced surface liquid in these mid-latitude regions in comparison to the runoff, high subsurface transport, and low infiltration cases, which all produce anomalous seas in the mid-latitudes (Fig. 4.7; note that our maps are not equal-area projections). The anomalous northern mid-latitude sea at ∼60°W so prominent in the runoff simulation, for instance, is absent in the control simulation. The southern mid-latitude paleobasin at ∼25°E is in fact the lowest elevation region on Titan (Corlies et al., 2017; Birch et al., 2017a)[89, 64] and is home to a deep anomalous sea in the low infiltration case. In the control simulation, however, the northern-most basin holds the deepest sea (Fig. 4.7a; orange cross), consistent with observations of the large north polar maria (Hayes, 2016)[52].

4.3.3 Resolution sensitivity

To briefly test resolution sensitivity, we run a simulation at T42 resolution (128 longitude grids by 64 latitude grids) for five Titan years with all parameters set to control values and with the same initialization procedure as the control simulation (starting with a dry surface and saturated subsurface at lower elevations). Fig. 4.8 shows the zonal precipitation and surface liquid distributions of the emergent climate. They are similar to results for our T21 simulations (Fig. 4.4; Fig. 4.7), and may in fact improve upon the southern hemisphere surface liquid distribution by limiting mid-latitude basin buildup even further in the southern hemisphere. The southern hemisphere in the high-resolution simulation exhibits only one major body of liquid, corresponding in location with the observed Ontario Lacus feature. However, in the northern hemisphere of the high-resolution simulation, surface liquid is limited to the polar circle, inconsistent with the observed maria that reach much farther equatorward. This could stem from the fact that elevation information from Corlies et al. (2017)[89] reflects lake surfaces rather than lake bottoms, with flattened elevation profiles where lakes are observed. Flow routing into observed lake locations will therefore

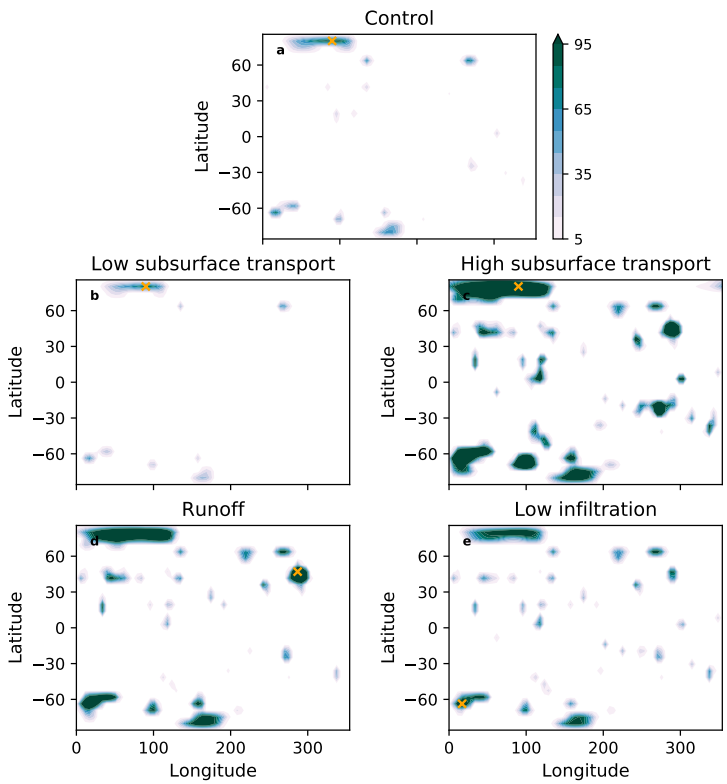

Figure 4.7: **Surface liquid distributions**. Surface liquid distribution (m) averaged over the final Titan year of each simulation, where each panel represents same simulation as in Fig. 4.4. Orange cross represents point of deepest surface liquid.

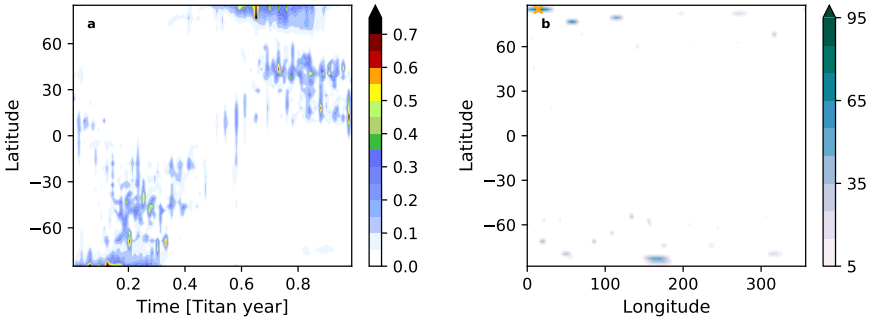

Figure 4.8: **High-resolution simulation**. a) Zonally averaged precipitation (mm d^{-1}) composited over five Titan years, as in Fig. 4.4, of the T42 simulation with control parameters. b) Surface liquid distribution (m) averaged over the fifth Titan year, as in Fig. 4.7, of the T42 simulation.

be less likely in our model at higher resolutions where these flattened surfaces become more prevalent, obscuring topographic basin bottom elevations in filled basins. Further work is needed to explore the impact of our hydrology scheme under higher resolutions, but this test shows that increasing resolution does not drastically change the basic climate state.

4.4 Meridional methane transport

Titan's current climate configuration features short and strong southern summers, which may promote stronger southern hemisphere evaporation (Aharonson et al., 2009)[58], or, conversely, enable greater northern hemisphere precipitation due to the longer northern summers (Schneider et al., 2012)[98], or force a combination of stronger southern evaporation and greater northern precipitation as shown in TAM wetlands simulations (Lora and Mitchell, 2015)[43]. Following the terrestrial literature (Peixoto and Oort, 1992; Trenberth and Stepaniak, 2003)[258, 259], Lora and Mitchell (2015) analyzed meridional moisture transports from TAM wetlands, decomposing the total atmospheric transport into the mean circulation component and the transient component representing eddy contributions. Here we focus on the partitioning of the total methane transport between the atmosphere, surface, and subsurface components, though we note that the partitioning of the total atmospheric transport between mean and transient components in all our simulations is similar to that of TAM wetlands (not shown).

We calculate the meridional moisture transport by the atmosphere:

$$F_{atm} = \int_{p_s}^{0} qv \frac{dp}{g} \tag{4.2}$$

where q is the simulated specific humidity, v is the simulated meridional wind, p and p_s are the pressure at model layers and surface pressure, and g is gravity. By computing changes in the surface liquid due to runoff alone and integrating in latitude, we can arrive at a corresponding meridional surface transport to compare against the above atmospheric transport:

$$F_{surf} = \int_{-\pi/2}^{\pi/2} 2\pi a cos\phi R d\phi \tag{4.3}$$

where R is the net input of simulated surface flow added to the surface reservoir in kg m^{-2} s^{-1}, a is Titan's radius, ϕ is the latitude in radians. Similarly, we calculate the meridional subsurface transport:

$$F_{sub} = \int_{-\pi/2}^{\pi/2} 2\pi a cos\phi [R_{sub} + O] d\phi \tag{4.4}$$

where R_{sub} is the net input of methane table flow added to the subsurface reservoir and O is the liquid outcropped onto the surface from methane table flow, both in kg m^{-2} s^{-1}.

Over long timescales, atmospheric convergence of moisture equals the net accumulation of methane by the atmosphere, given by the difference between precipitation and evaporation. Thus, regions of atmospheric convergence, i.e. where the atmospheric meridional transport is negatively sloped with increasing latitude (positive transport values indicate northward flow; negative, southward), correspond to regions of net positive methane accumulation. Similarly, regions of surface and subsurface convergence in our simulations correspond to net positive methane accumulation accomplished solely by surface and subsurface mechanisms, respectively. The TAM wetlands simulations exhibited convergent flow into the low latitudes with sharp peaks at the wetlands boundaries (Lora and Mitchell, 2015)[43]. Previous Titan models were noted for diverging moisture from the low latitudes (e.g. Mitchell, 2008)[138], but they assumed globally wet surfaces while TAM wetlands forced a bimodal climate of

equatorial deserts and polar wetlands. While the atmospheric transport in TAM wetlands converges moisture into the lower latitudes, poleward methane transport still exists at high latitudes, as a consequence of large solstitial transports (Lora and Mitchell, 2015)[43]. Indeed, the annual-mean total atmospheric transport in TAM wetlands is itself a small residual of large solstitial transports, as it is for all simulations in this study.

4.4.1 Control simulation

In our control simulation, subsurface transport diverges moisture out of the low latitudes to self-consistently produce the same bimodal climate as TAM wetlands. Towards the end of our simulations this divergent subsurface transport is generally balanced by the convergent atmospheric transport (Fig. 4.9a). The atmospheric transport of the control simulation (Fig. 4.9a; blue line) is therefore similar to the atmospheric transport of the wetlands simulation, with peaks in the mid-latitudes. With little surface liquid available to flow, surface transport in the control simulation remains small compared to atmospheric and subsurface transports at all latitudes, only becoming prominent in the mid-latitude basin regions. Note that the surface transport, unlike the atmospheric transport, is insensitive to seasonality, with little to no change between northern and southern summer (not shown).

The control climate is regionally out of steady-state equilibrium, since the total transport (Fig. 4.9a; dotted black line) is not zero at all latitudes; but the total transport at the equator is approximately zero, indicating minimal cross-equatorial transport. Summed over all latitudes, the total transport (Fig. 4.9a; dotted black line) is net northward at $\sim 10^{13}$ kg per Titan year, but that amount is dwarfed by the total methane inventory in the global climate system, which is on the order of 10^{19} kg.

4.4.2 Sensitivity simulations

The climates in the other simulations, on the other hand, exhibit modest cross-equatorial transport, even in the runoff simulation that was run independently for the same amount of time as the control simulation. Recall that sensitivity simulations branched off from the

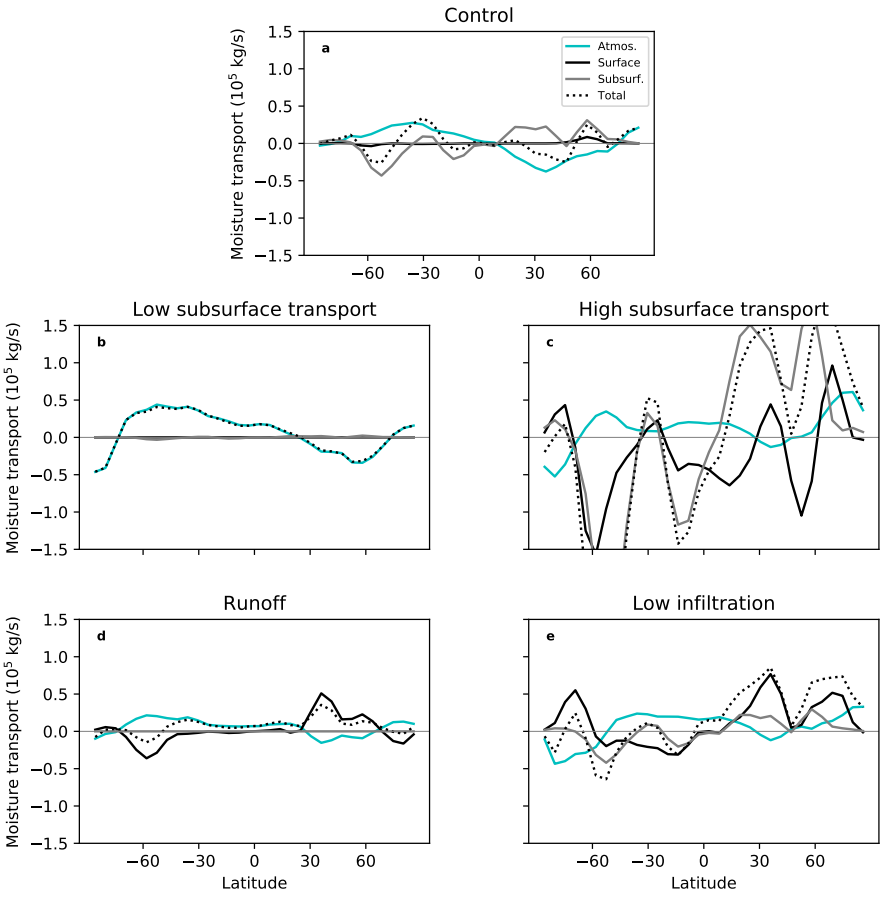

Figure 4.9: **Meridional moisture transport**. Zonally averaged meridional moisture transports averaged over the final five Titan years of each simulation, where each panel represents same simulation as in Fig. 4.4. Transports due to the atmosphere (blue line), overland surface flow (black line), subsurface flow (grey line), and total (dotted black line) are shown. Positive values indicate northward transport, while negative values indicate southward transport.

control simulation were run for a relatively short amount of time.

In the low subsurface transport case, subsurface outflow is not strong enough to balance atmospheric inflow into the low latitudes (Fig. 4.9b), rendering the climate system further out of equilibrium than in the control simulation. The total transport is therefore dominated by the atmospheric transport, featuring a strong northward cross-equatorial component. This leads to a scenario where rain in the low latitudes infiltrates and is trapped in the subsurface of the equatorial highlands. Since infiltrated methane in our model is directly added to the methane table, deep highland methane (which can be several hundreds of meters below the surface) cannot return easily to the atmosphere in the absence of subsurface transport, leading to a precipitation shutdown (Fig. 4.4b).

Conversely, in the high subsurface transport case, strong divergent subsurface flow out of the high-elevation low latitudes exceeds atmospheric transport and dominates the climate system (Fig. 4.9c), leading to considerable surface liquid buildup in the polar lowlands. Computational constraints prevent us from running these simulations out for hundreds to thousands of Titan years, but the end state of this high subsurface transport scenario would presumably be a complete flattening of the global methane table, with abundant surface liquid in the basins of both hemispheres. Substantial outcropping onto the surface promotes a large, predominantly southward surface transport driven particularly by low- and mid-latitude basin regions in both hemispheres. Southward surface transport exists at all equatorial latitudes and is especially prominent in the southern mid-latitudes around $\sim$60°S.

The surface transport in the runoff simulation is comparable in magnitude to the atmospheric transport (Fig. 4.9d), and is in fact stronger in the mid-latitude regions. Rather than broadly divergent, the surface transport direction is predominantly northward, like the atmospheric transport, suggesting an enhancing effect of the hemispheric surface liquid asymmetry by overland surface flow. In the northern hemisphere, northward surface transport exists at all latitudes poleward of the equator until $\sim$75°N, routing large stores of methane down the broad zonal topographic gradient into the northern lowlands. In the southern hemisphere, southward surface transport exists in the mid-latitudes and northward surface transport exists in the polar region, thereby forming a region of convergence around

~60°S, as seen in the high subsurface transport case.

Lowering infiltration results in a similar climatic evolution as the high subsurface transport simulation, except that in this case the dominant mechanism for producing polar wetlands is overland surface flow rather than subsurface transport, as indicated by the strong surface transport (Fig. 4.9e; black line). In contrast to the high subsurface transport case, though, the surface transport in the low infiltration case is net northward, with northward transport everywhere in the northern hemisphere, largely echoing the profile from the runoff simulation. A broad region of convergence in the southern mid-latitudes exists as well, as in the high subsurface transport, runoff, and control (albeit quite small) simulations.

4.5 Evolution of methane reservoirs

4.5.1 Control simulation

Fig. 4.10 displays maps of average surface liquid fluxes by each component of the hydrologic cycle in the control simulation. The initial years (Fig. 4.10; top row) exhibit a different climatology than the final years (Fig. 4.10; bottom row). Greater mid-latitude precipitation and weaker polar evaporation in the initial years are largely responsible for producing the surface liquid distribution seen in Fig. 4.7a. Fig. 4.10b shows that the greatest amount of precipitation occurs over mid-latitude highlands, but including infiltration in Fig. 4.10c demonstrates that nearly all of this mid-latitude rainfall infiltrates into the subsurface, thus limiting the amount available for mid-latitude runoff. Meanwhile, weaker infiltration in the saturated polar regions promotes greater runoff in those zones, leading to net positive accumulation in the polar basins (Fig. 4.10d,e).

Towards the end of the control simulation, greater surface liquid amounts lead to greater evaporation (recall the simulation begins with zero surface liquid). Surface evaporation over the seas—in addition to modest groundmethane evaporation (see Fig. 4.11; top row)—maintains the polar precipitation structure (Fig. 4.10f), but mid-latitude precipitation is reduced and strong surface evaporation outweighs precipitation over the seas (Fig. 4.10g).

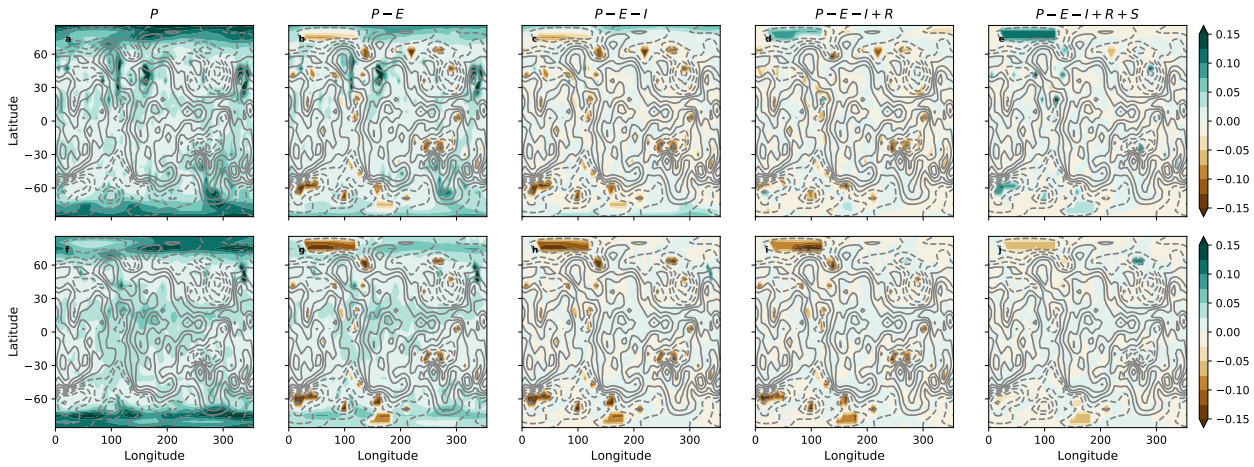

Figure 4.10: **Surface liquid accumulation maps for control simulation**. From left to right, maps of a,f) P, b,g) $P-E$, c,h) $P-E-I$, d,i) $P-E-I+R$, and e,j) $P-E-I+R+O$, where P is precipitation, E is surface liquid evaporation, I is infiltration, R is net input from surface runoff, and O is outcropping. Color contours for each panel are same and shown on right in mm d^{-1}. Top row gives averages over the first five Titan years of the control simulation, while bottom row shows averages over the final five Titan years of the control simulation. Grey contours show normalized topography as in previous figures.

Polar precipitation is locally infiltrated into unsaturated pockets, as demonstrated by the effect of infiltration at the highest latitudes (Fig. 4.10h). Thus, minimal surface runoff occurs (Fig. 4.10i), but moderate outcropping from the subsurface largely balances surface evaporation from basins in low and high latitudes (Fig. 4.10j), and also helps maintain sea-adjacent unsaturated pockets by removing infiltrated liquid (Fig. 4.11; top row).

The most bottom-right panel of Fig. 4.10 displays the average net surface liquid accumulation at the end of the control simulation (Fig. 4.10j). Consistent with a stable surface liquid amount, there is approximately as much surface drying as wetting; meanwhile, in the subsurface, infiltration is in balance with groundmethane evaporation and subsurface transport (Fig. 4.11; top row). However, slight net drying in the high-latitude seas of both hemispheres exists in our simulations, suggesting that the maria in our simulations may have limited lifetimes.

4.5.2 Sensitivity simulations

Fig. 4.11 shows maps of various contributions to subsurface liquid accumulation for all simulations. As noted above, in the control simulation, groundmethane evaporation is highest in

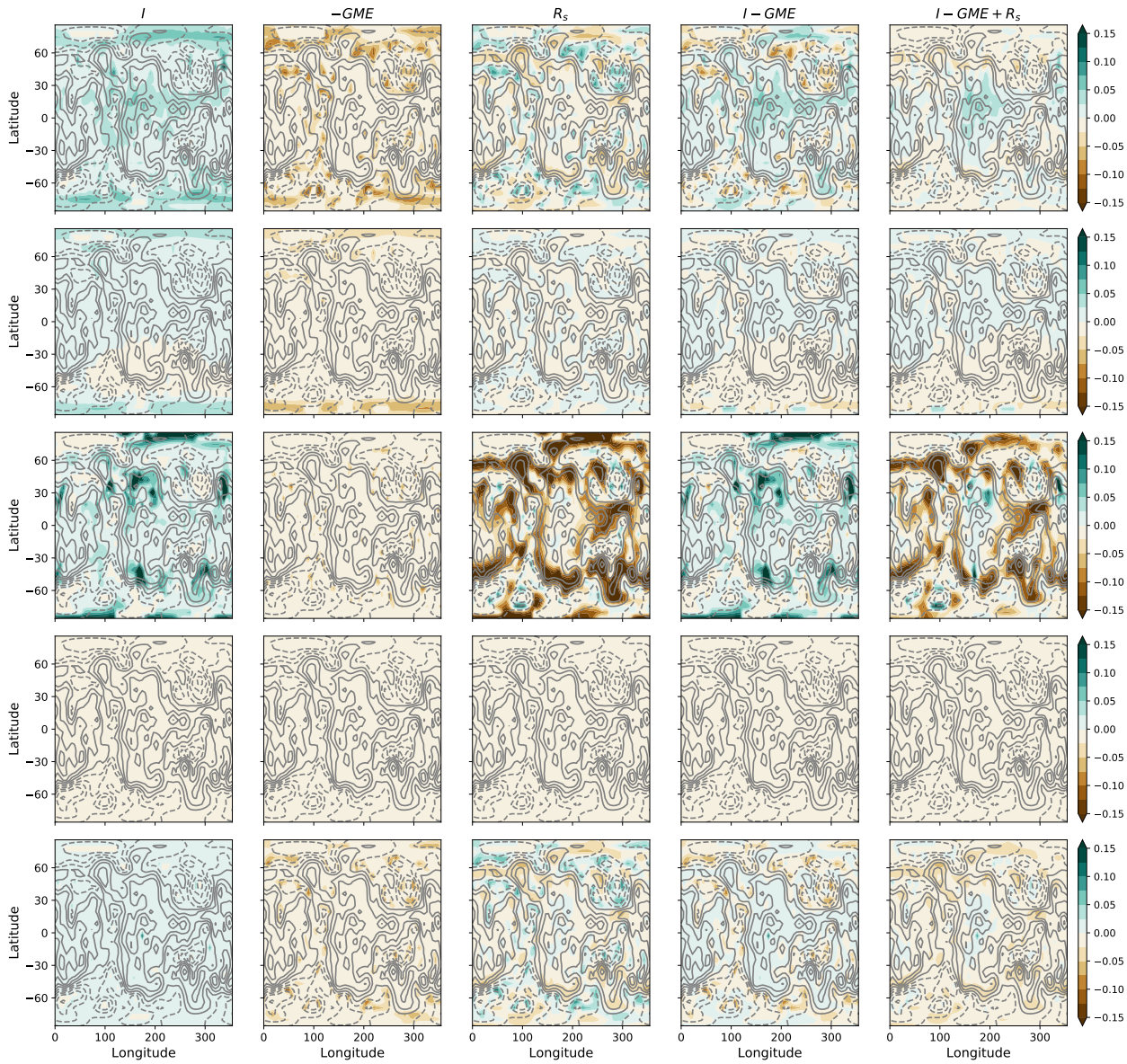

Figure 4.11: **Subsurface liquid accumulation maps**. From left to right, maps of I, GME, R_s, $I-GME$, and $I-GME+R_s$, where I is infiltration, GME is groundmethane evaporation, and R_s is net input to the methane table from horizontal subsurface flow. Color contours for each panel are same and shown on right in mm d^{-1}. From top to bottom, rows pertain to: 1) control simulation, 2) low subsurface transport case, 3) high subsurface transport case, 4) runoff case (which excludes subsurface effects so all values here are zero), and 5) low infiltration case. Values are averaged over the last five Titan years of each simulation. Grey contours show normalized topography as in previous figures.

the saturated polar regions (see Fig. 4.12 for saturation maps), particularly on the outskirts of large seas, and is balanced by horizontal subsurface transport that moves liquid towards the seas at topographic minima (Fig. 4.11; third column). Unsaturated pockets are generally adjacent to large seas (Fig. 4.12); they are continuously filled by infiltration and emptied by horizontal subsurface transport in a steady balance. This process is apparent in the other cases as well. The high subsurface transport case, however, has abundant surface liquid and therefore less contributions from groundmethane evaporation, which only occurs when the surface is dry. Stronger rain (see Fig. 4.13 for contributions to surface liquid accumulation) leads to stronger infiltration in this case, but substantial outcropping vastly outweighs infiltration at high latitudes and mid-latitudes, leading to net global drying of the subsurface reservoir (Fig. 4.11; fifth column). Net drying of the subsurface reservoir also occurs in the low infiltration case, while net wetting (albeit small and difficult to discern at these contours) occurs in the low subsurface transport case, concentrated in the mid-latitudes.

Maps showing contributions pertinent to surface liquid accumulation (Fig. 4.13) reflect the general climatic evolution interpreted from the above subsurface liquid accumulation (Fig. 4.11) and moisture transport (Fig. 4.9) scenarios. The control simulation features approximately as much surface drying as wetting (Fig. 4.13; sixth column). The low subsurface transport case features net global surface drying, particularly from the south polar sea associated with Ontario Lacus due to less polar precipitation than the control simulation (Fig. 4.13; first column). Meanwhile, in the high subsurface transport and low infiltration cases, polar basins fill substantially and the equatorial highlands remain neutral (Fig. 4.13; sixth column). Outcropping in the high subsurface transport case is largely responsible for providing the available surface liquid for runoff given the strong surface drying realized by precipitation, evaporation, and infiltration contributions (Fig. 4.13; fourth column). In the runoff simulation, due to the absence of infiltration, mid-latitude rain pools in mid-latitude basins, balancing strong evaporation. Precipitation in the runoff simulation is higher in the northern hemisphere than southern hemisphere, driving the net wetting of northern maria (Fig. 4.13; sixth column). Surface runoff in the low infiltration case drives surface wetting by routing abundant surface liquid into seas, outweighing evaporation.

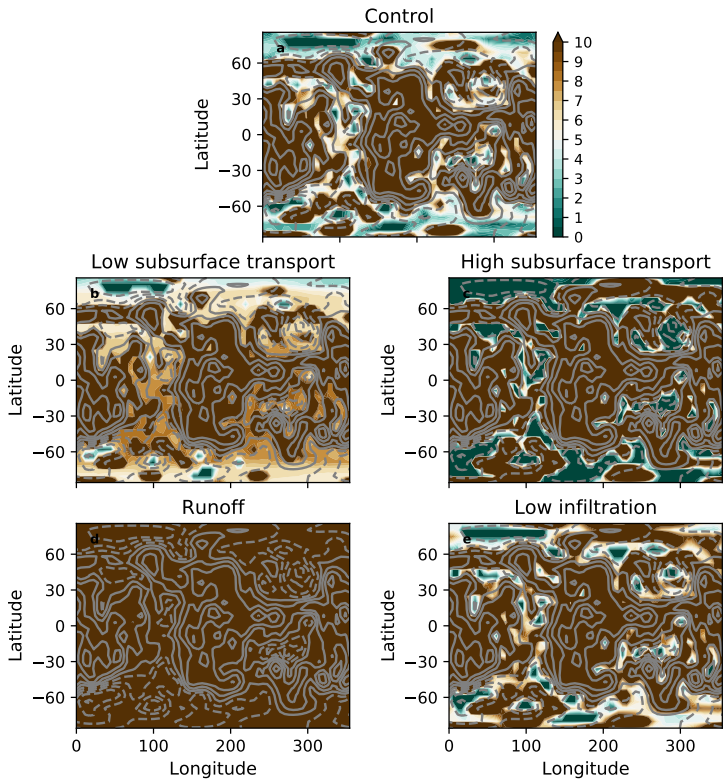

Figure 4.12: **Near-surface saturation maps**. Depth to methane table (m) averaged over the final five Titan years of each simulation, with panels and topography (grey contours) as in previous figures. Note subsurface in runoff case is considered unsaturated.

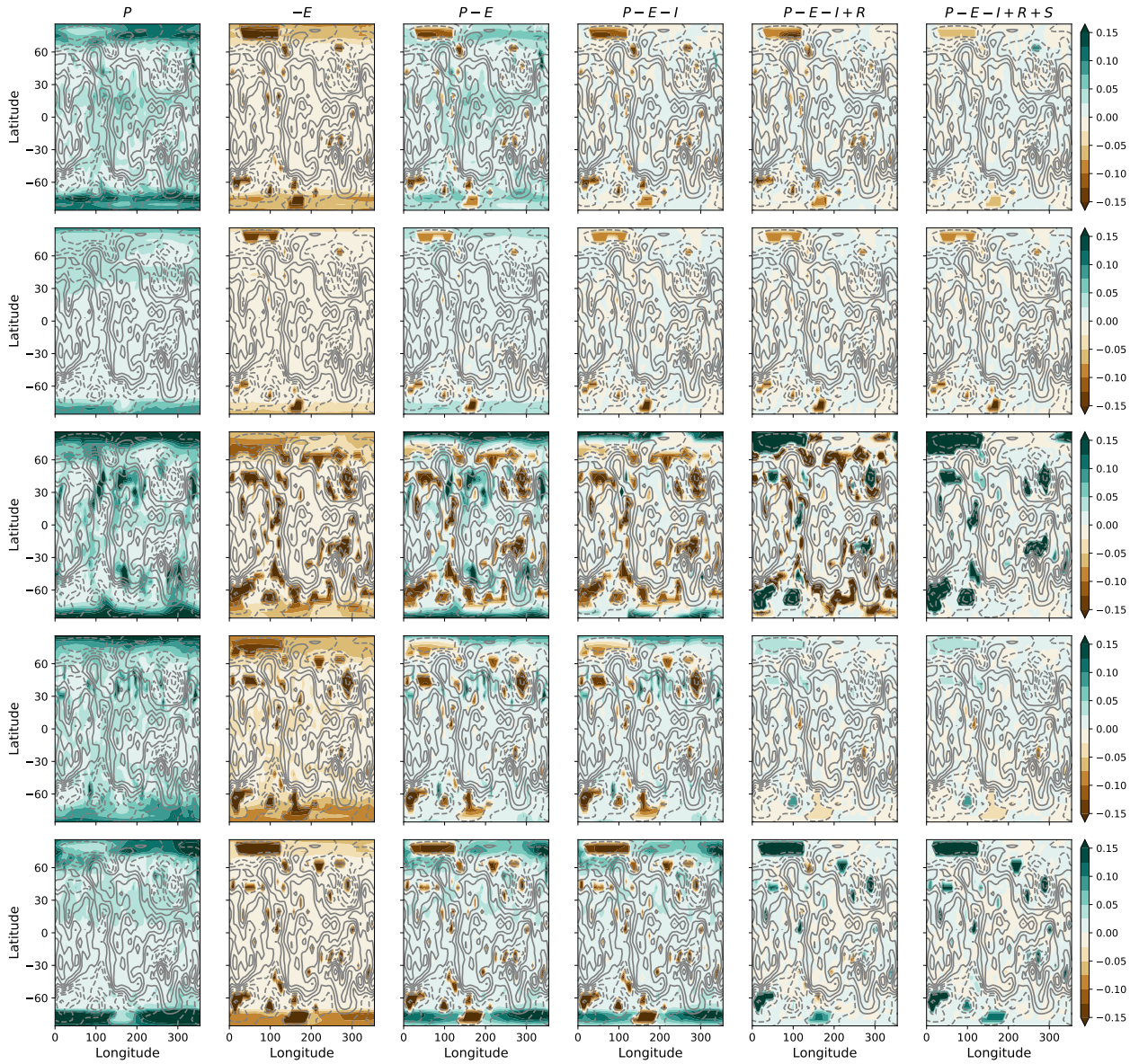

Figure 4.13: **Surface liquid accumulation maps for all simulations**. From left to right, maps of P, E, $P - E$, $P - E - I$, $P - E - I + R$, and $P - E - I + R + O$, as in Fig. 4.10 but with the addition here of evaporation. From top to bottom, as in Supplementary Fig. 4.5, rows pertain to: 1) control simulation, 2) low subsurface transport case, 3) high subsurface transport case, 4) runoff case (which excludes subsurface effects so all values here are zero), and 5) low infiltration case. Values are averaged over the last five Titan years of each simulation. Grey contours show normalized topography as in previous figures.

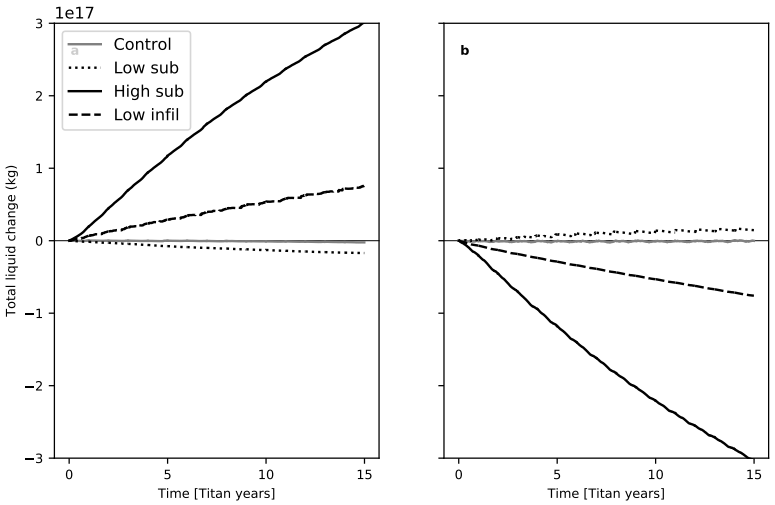

Figure 4.14: **Methane inventories for simulations incorporating subsurface effects**. a) Total surface liquid inventory change (kg) from the 60th Titan year of the control simulation for the control (grey line), low subsurface transport (black dotted line), high subsurface transport (black solid line), and low infiltration (black dashed line) simulations. b) Total subsurface liquid inventory change (kg) for same simulations on same scale as left panel.

Fig. 4.14 displays liquid reservoir changes in time for each simulation with subsurface effects included, as further evidence that infiltration-dominant regimes (e.g. the control and low subsurface transport simulations) maintain or lose surface liquid to the subsurface while flow-dominant regimes (e.g. the high subsurface transport and low infiltration simulations) gain surface liquid at the expense of the subsurface.

4.5.3 Interhemispheric transport rates

Summed over all latitudes and normalized by latitude, the net northward total transport in the control simulation is $\sim$1.5 x 10^4 kg s^{-1}, which is on the order of 10^{13} kg per Titan year and therefore corresponds to an interhemispheric transport timescale of 10^3–10^4 Titan years for a methane inventory of 10^{16}–10^{17} kg. This inventory was estimated for Titan's observed surface liquid using initial radar observations and terrestrial dimensional relationships (e.g. Lorenz et al., 2008b)[129], but may in fact be much larger when considering subsurface methane, thereby extending the transport timescale. Indeed, in our simulations, the atmospheric inventory is an order of magnitude greater than the surface inventory, while the subsurface inventory is two orders of magnitude greater than the surface inventory. The magnitude of

any presumed subsurface liquid inventory on actual Titan, however, is unknown and difficult at this point to constrain.

Liquid reservoirs in simulations branched from the control are still stabilizing after 15 Titan years (Fig. 4.14), making it difficult to interpret whether total transport rates are steady. The runoff simulation, however, was run for 75 Titan years and exhibits a steady net northward transport rate (i.e. the magnitude changed little over the final Titan decades) that is an order of magnitude greater than that for the control simulation. Modest northward cross-equatorial transport occurs at the equator (Fig. 4.9d; dotted line), and, in the absence of any subsurface inventory, indicates a dessication timescale of the southern hemisphere of $\sim 10^3$ Titan years. This adds to the argument that the control simulation is more consistent with observations, given the unlikelihood that a climate would exist so far out of steady-state equilibrium.

4.6 Discussion

Adding surface hydrology to an existing GCM recreates a wetlands climate, with strong solstitial precipitation over saturated polar regions, dispersed mid-latitude storms, high-latitude maria, and equatorial deserts. The infiltration-dominant control simulation produces the best match to observations, beautifully reproducing Titan's mid-latitude cloud outbursts (Fig. 4.4a) and polar maria (Fig. 4.7a), suggesting that Titan itself resides in an infiltration-dominant regime where the subsurface is important. Low- and mid-latitude basins have limited buildup because they are adjacent to unsaturated highlands and therefore receive limited runoff because local precipitation at nearby highlands infiltrates to the deep methane table. The polar regions, on the other hand, are more saturated, promoting methane buildup in basins through a combination of greater precipitation and less infiltration than the lower latitudes, leading to the polar maria. The runoff simulation, which excludes subsurface effects, also reproduces a wetlands climate consistent with cloud observations; and additionally features enhanced northward transport potentially consistent with the observed hemispheric asymmetry in surface liquids. Low-latitude highlands block northern

liquid from returning to the southern hemisphere along the surface, thereby cementing and accelerating the net northward transport done by the atmosphere. However, large low- and mid-latitude seas form in the runoff simulation that are not observed, with the deepest existing in a northern mid-latitude basin known to be dry (Hayes et al., 2008)[57]. Furthermore, the runoff simulation is not in steady-state equilibrium, rendering it unlikely to represent Titan's modern climate.

The control and runoff simulations exemplify two opposing climate regimes found in our study: infiltration-dominant and flow-dominant. Infiltration-dominant regimes, like the control and low subsurface transport simulations, adequately simulate the observed surface liquid distribution, whereas flow-dominant regimes, like the three other cases, produce anomalous seas inconsistent with observations (Fig. 4.7). The extremes of these two regimes—the low and high subsurface transport cases—are either too dry or too wet (Figs. 4.13, 4.14), and therefore feature precipitation distributions inconsistent with observations, with rainfall that is either too sparse (Fig. 4.4b) or too abundant (Fig. 4.4c), respectively. As such, the control simulation represents an appropriate balance between the two regimes. In all cases, the atmosphere deposits methane into the low latitudes while surface and subsurface transports route methane into mid-latitude basins, particularly in the southern hemisphere at ∼60°S (Fig. 4.9). Polar regions are kept saturated by strong precipitation at the highest latitudes (Figs. 4.10, 4.12)—a result of the cross-equatorial branch of the seasonal circulation transporting moisture to the summer pole (e.g. Mitchell, 2006)[30]. In the annual-mean, however, the net atmospheric transport in the beginning of the control simulation (and in all simulations except for the high subsurface transport case) is northward.

A picture therefore emerges in the south of low-latitude southern hemisphere liquid pooling in mid-latitude basins, where it evaporates into the atmosphere to be transported northward. In all simulations, atmospheric transport is northward at latitudes equatorward of ∼60-70°S (Fig. 4.9), which approximately coincides with the latitude of maximum surface flow convergence. As the atmosphere transports methane northward, methane that does not cross the equator and rains out at low latitudes flows (either over land or through the subsurface after infiltrating into unsaturated highlands) back poleward down the topographic

gradient into the mid-latitude basins. At the end of the control simulation, northward atmospheric transport is balanced approximately by southward subsurface transport at equatorial latitudes; thus, little methane is able to cross the equator and move from the southern hemisphere to the northern hemisphere. A similar story unfolds in the northern hemisphere, though southward atmospheric transport in the northern hemisphere is weaker than northward atmospheric transport in the southern hemisphere.

Before reaching steady-state equilibrium, the climate in all simulations forces liquid buildup in the high latitudes, while transporting methane into the northern hemisphere (except for in the high subsurface transport case). In our control simulation that has reached steady-state equilibrium, the climate maintains high-latitude wetlands due to poleward surface and subsurface transports, while limiting interhemispheric transport from a balance between atmospheric and subsurface transports at the equator. The runoff simulation cannot reach steady-state even after 75 Titan years, indicating the importance of subsurface flow in achieving climate equilibrium. It has been suggested that Titan's modern climate may not be in equilibrium (Moore et al., 2014)[120], as potentially forced by a global restructuring following a major pulse of methane into the system such as from a cryovolcanic episode (Tobie et al., 2006)[130] or impact event (Zahnle et al., 2014)[260]. However, our control simulation reproduces Titan's modern surface liquid and cloud distributions while being in approximate steady-state equilibrium with minimal interhemispheric transport. This result suggests that Titan's modern climate may indeed be in steady-state equilibrium itself (e.g. Lunine and Atreya, 2008)[261]—a more likely scenario than us witnessing Titan at a special time in its evolution.

Some inconsistencies with observations remain in our control simulation, particularly the comparable size of the anomalous southern mid-latitude sea with Ontario Lacus, the major observed body of liquid in the southern hemisphere. Our simulations even show that Ontario Lacus may be diminishing (Fig. 4.10j), conflicting with observations. While evaporation is comparable between the south polar sea and the anomalous southern mid-latitude sea in our simulations (Fig. 4.13), precipitation is much higher at the poles (Fig. 4.10a,f), which may help explain the lake's observed persistence. Surface liquid accumulation maps (Figs.

4.10j, 4.13), however, show that overall drying in the south polar basin associated with Ontario Lacus is greater than overall drying in the southern mid-latitude basin at ∼25°E in our simulations. We speculate that simplifications in our hydrology parameterizations may account for this discrepancy. First, topography remains uncoupled to the atmosphere in this model, leading us to neglect zonally asymmetric orographic effects on the lower tropospheric circulation (Tokano, 2008)[262]. Second, flow amounts are calculated according to terrestrial methods that may not apply to Titan's particular bedrock and drainage characteristics, nor to the coarse resolution of a global GCM. Furthermore, we assume in our model that subsurface flow occurs through a globally connected methane aquifer of homogenous soil makeup. However, it is more likely that subsurface connections, if they exist at all, occur through a network of regional aquifers of varying rock types (Hayes et al., 2017; Birch et al., 2017b)[63, 121]. Thick megaregolith and exposed bedrock may dominate the low latitudes (Howard et al., 2016)[222], for instance, while karstic material constitutes the high latitudes (Cornet et al., 2015; Hayes et al., 2017; Birch et al., 2017b)[220, 139, 63, 121], in which case infiltration and subsurface flow would be spatially dependent, perhaps on the scale of individual basins.

The infiltration rates used in the control simulation and low infiltration case essentially bracket the range of hydraulic conductivity values given by permeability estimates (Hayes et al., 2008)[57], which constrain conductivities to be 10^{-8}–10^{-2} m s^{-1}. Shoreline recession at Ontario Lacus (Hayes et al., 2011; Turtle et al., 2011c)[234, 235] is consistent with vertical infiltration rates on the low end of this range, on the order of 10^{-8} m s^{-1}. This rate is used in our low infiltration case, which produces a climate largely consistent with observations, with the exception of the anomalous mid-latitude seas produced by mid-latitude runoff. Consequently, a plausible scenario might be a mixture of the infiltration-dominant and flow-dominant regimes: one with high infiltration capacity in the mid-latitudes and high latitudes, and low infiltration capacity in the low latitudes. In addition to infiltration in mid-latitude highlands, this setup would presumably lead to runoff eroding exposed bedrock in the low latitudes and draining into maria via saturation flow in the high latitudes, as observed (e.g. Burr et al., 2013a)[81]; and may also be more consistent with the unique geomorpholog-

ical character of mid-latitude climate zones, which are generally plains units composed of organic-rich material deposits (Malaska et al., 2016; Lopes et al., 2016)[226, 85]. While these mid-latitude terrains are hypothesized to be dominated by aeolian deposition, evidence for sediment transport by extreme storms (Birch et al., 2016; Faulk et al., 2017b)[82, 155] also suggests a local fluvial control on landscape morphology. In the above hypothetical case of high infiltration capacity in the mid-latitudes, surface runoff and resulting sediment transport would indeed be limited to the most extreme storms, potentially consistent with these mid-latitude plains units.

Similarly, horizontal subsurface transport rates may be higher in the high latitudes and lower in the low latitudes and mid-latitudes (Horvath et al., 2016)[139], precluding sea formation in mid-latitude basins and promoting polar saturation. The control subsurface transport rate correlates to a hydraulic conductivity that on Earth is typical of semi-pervious soils, such as compacted sandstones, clays, silt, and fine sand (see section 4.2). This rate is therefore consistent with reports from the Huygens probe, which landed near the equator on what was interpreted to be wet clay or sand (Zarnecki et al., 2005; Lorenz et al., 2006b)[132, 133], but the properties of the regolith and bedrock below the first few centimeters and at other latitudes are poorly constrained. Soils in polar lake districts have been suggested to be composed of highly porous karst-like materials that may contribute to the surface liquid evolution of polar seas over geological timescales via dissolution processes (e.g. Cornet et al., 2015)[220]. Future missions to Titan, including a possible lander, would further characterize Titan's unique lithologic conditions and inform global climate model developments.

Our model may also be leveraged to address the existence of ephemeral lakes on Titan, which have been suggested by observations of evaporite deposits (Barnes et al., 2011)[65] and of potential lakes in the equatorial deserts (Griffith et al., 2012; Vixie et al., 2015)[68, 69]. In a preliminary investigation using the simulations presented in this work, ephemeral lakes lasting for one to two Titan years occur predominantly equatorward of 40° and occasionally in the regions associated with Hotei Regio and Tui Regio (Moore and Howard, 2010)[263]. These lakes may be sourced by intense mid-latitude storms or connected to local subsurface aquifers that seasonally outcrop, but further work is necessary to fully explore such features.

4.7 Summary

In summary, past climate models of Titan have broadly reproduced Titan's hydrologic cycle but have done so without considering the influence of atmospherically-coupled surface hydrology. By adding surface and subsurface parameterizations to a Titan GCM, we now successfully reproduce the observed cloud and surface liquid distributions within a more physically consistent framework and attain approximate steady-state equilibrium. Our simulations present a suite of possible climate states for Titan, demonstrating that surface and/or subsurface transport may be crucial to the overall global methane transport and large-scale climate. We show that divergent subsurface transport may balance the convergent atmospheric transport in an infiltration-dominant regime that stores methane in low-latitude highlands while producing surface-saturated polar wetlands regions. Variations of hydrologic parameters robustly recreate this wetlands climate of equatorial deserts and saturated polar regions. Flow-dominant regimes, however, produce anomalous seas in mid-latitude basins that are not observed, while a simulation with decreased subsurface transport locks too much methane in low-latitude highlands and consequently shuts down precipitation. Our infiltration-dominant control simulation best reproduces observations and reaches steady-state equilibrium in terms of interhemispheric transport, suggesting that Titan's modern climate may itself be in a similar steady-state equilibrium thanks to the presence of subsurface flows. This study exemplifies our model's utility as a tool for climatic understanding, suggesting the model's potential application to other planetary settings, including Titan's own paleoclimate. Future missions and modeling work can better constrain Titan's regional soil parameters to lay the groundwork for understanding Titan as a fully connected surface-atmosphere system, like Earth, and elucidate the timeline of its climatic evolution.

CHAPTER 5

Conclusions

Titan is a world of flowing rivers and rain that reminds us of our own. Storm clouds bring seasonal, monsoon-like downpours, feeding rivers that spill into great lakes and seas. Flowing liquid can make its mark on the surface by carving channels into the bedrock and carrying sediments vast distances. Already obscured to us by haze and distance, Titan may hold further mysteries in the form of potentially vast subsurface hydrocarbon reservoirs that replenish the atmosphere and maintain the global climate structure.

In this dissertation, we have explored the rich hydroclimate of Titan through several perspectives, from moist tropical dynamics to geomorphic work by extreme rainstorms to surface and subsurface transports. Titan's prominence as an active hydrologic body, the only one in the Solar System other than Earth, has compelled us to compare against Earth every step of the way and to update our model in Earth's likeness. Each perspective illuminates the intimate connection between atmosphere and surface, showing the connection to be so deep as to dissolve formal distinctions and conceive of planetary climate as a holistic system. In this brief and final chapter, we summarize our findings and detail possible avenues for future work.

5.1 Surface-atmosphere connections

Regional variations in surface features suggest corresponding variations in climate, particularly variations in precipitation—since rainfall and subsequent runoff in terrestrial settings are crucial towards eroding the surface and filling lakes, while the absence of rainfall promotes dune formation. Among the first observations of Titan by Cassini was the basic climate di-

chotomy of equatorial deserts and polar maria as driven by atmospheric moisture transport. To understand what we see, then, we use computer models to analyze characteristics of the atmosphere and, where available, of the coupled surface-atmosphere system.

In Chapter 2, we study a wide range of atmospheric circulations with an idealized moist general circulation model to evaluate the mechanisms controlling intertropical convergence zone (ITCZ) migrations. Observations of a seasonal convergence zone on the slowly rotating Titan motivate us to reconsider the theoretical underpinnings of the terrestrial ITCZ in a new planetary light. We use a zonally symmetric aquaplanet model with a slab ocean of fixed depth and force top-of-atmosphere insolation to remain fixed at the pole for an "eternal solstice" simulation and also vary seasonally for a range of rotation rates, keeping all other parameters Earth-like. For rotation rates $\Omega_E/8$ and slower, a transient maximum in zonal-mean precipitation appears at the summer pole; however, the ITCZ associated with the ascending branch of the Hadley circulation lies at $\sim 60^\circ$.

We assess how widely-used predictors of the ITCZ position perform in this wide parameter space. Standard predictors based on different estimates of the Hadley cell's poleward extent are correlated with but overestimate off-equatorial ITCZ locations. Interestingly, in the eternal solstice case for Earth's rotation rate, the ITCZ remains at subtropical latitudes even though the lower-level moist static energy maximizes at the summer pole. While seemingly at odds with convective quasi-equilibrium arguments, this can happen because, at Earth's rotation rates, the thermal stratification set in convective regions can only be communicated within the tropics, where temperature gradients are constrained to be weak. We therefore develop an understanding of the ITCZ's position based on top-of-atmosphere energetics and the boundary layer momentum budget and argue that friction and pressure gradient forces determine the region of maximum convergence, offering a modified dynamical perspective on the monsoon-like seasonal weather patterns of terrestrial planets. Large maria and wetlands units observed in Titan's polar regions are suggested to be a consequence of seasonal rainfall that concentrates precipitation in the highest latitudes.

In Chapter 3, we turn our focus towards individual rainstorms, particularly intense baroclinic ones, rather than on the large-scale circulation. Geomorphic features typically associ-

ated with extreme rainfall events in terrestrial settings, including extensive fluvial features and alluvial fans, have been detected on Titan's surface. Methane flow from precipitation on Titan can transport sediments and potentially erode the icy bedrock, but averaged precipitation rates from prior global-scale modeling are too low by at least an order of magnitude to initiate sediment transport of observed grain sizes in the low latitudes. We quantify the regional magnitude, frequency, and variability of extreme rainfall events from simulations of present-day Titan, with a general circulation model coupled to a land model partially covered by wetlands reservoirs that can capture Titan's regionally varying hydroclimate. We find that the most extreme storms tend to occur in the mid-latitudes, where observed alluvial fans are most concentrated. Storms capable of sediment transport and erosion occur at all latitudes in our simulations, consistent with the observed global coverage of fluvial features. Our results therefore demonstrate the influential role of extreme precipitation in shaping Titan's surface, and provide the basis for estimating erosion rates based on individual storm events.

Surface hydrology components, including surface and subsurface flow, infiltration, and groundwater evaporation, are essential to Earth's hydrologic cycle and may be similarly influential on other planetary bodies. Titan in particular harbors a rich hydroclimate comparable to Earth's, with evidence of active surface hydrology tied to the atmospheric circulation in the form of drainage basins and wetlands zones that are particularly concentrated in the low-elevation polar regions. General circulation models for Titan have thus far neglected basic representations of surface hydrology, however, and therefore neglected the potential hydraulic influence of Titan's large-scale topography. In Chapter 4, we add a surface hydrology model to an existing Titan atmospheric model and find that infiltration and topography-driven flow play fundamental roles in reproducing Titan's observed surface liquid and cloud distribution. We propose that Titan's current climate involves some combination of infiltration dominating unsaturated low-latitude highlands, and surface or subsurface flow dominating saturated high-latitude lowlands and mid-latitude basins. Surface hydrology therefore promotes poleward methane transport, contributing to the production of the observed polar wetlands and equatorial deserts.

5.2 Planetary applications

The demonstrated climate-surface connections in this dissertation may additionally enable studies of other planetary processes and planetary settings. The past and future climates of Earth are heavily influenced by the large-scale circulation examined in Chapter 2. Snowball state evolutions on terrestrial planets depend on energy transported by the Hadley cell (Pierrehumbert, 2005; Abbot and Pierrehumbert, 2010; Voigt et al., 2012)[209, 210, 264]; and, perhaps of greatest current importance to the planetary community, climate change will undoubtedly alter the structure of the large-scale circulation and therefore change regional precipitation patterns (e.g. Byrne and Schneider, 2018)[265]. Additionally, our work to understand the climate over a range of planetary parameters can inform efforts to determine the habitability of terrestrial exoplanets. Given the simple connection demonstrated in Chapter 2 between rotation rate and circulation, even simple models of other planets can yield tremendous information about their potential climates (e.g. Yang et al., 2014)[266].

Geomorphic connections span space and time as well. Flash floods on Earth periodically carry sediments to produce alluvial fans but can also trigger landslides and mudslides, such as in southern California (e.g. Campbell, 1974)[267]. Understanding the connections between intense rainstorms and their effects on the surface could therefore potentially help in identifying and evaluating landslide risks. The analysis done in Chapter 3 could also be extended to past climates on Titan and, even, on Mars, the surface of which also clearly displays large alluvial fans (Moore and Howard, 2005)[117]. In fact, the surface-atmosphere connections suggested by this dissertation could potentially occur on any planetary body, rendering planetary surfaces as records of past and present climates, and thereby opening up new avenues towards understanding the impacts of climate changes on Earth and elsewhere.

Furthermore, the surface hydrology model developed in Chapter 4 can be easily applied to other planetary bodies, and therefore provide a more realistic framework for performing extreme precipitation analyses as well as a tool for understanding contributions to planetary hydroclimate. For instance, general circulation models have been useful in addressing the early Martian climate problem (e.g. Wordsworth et al., 2016)[268], in which valley networks

play a significant role in constraining past climate. Orographic precipitation on Mars has been connected to these valley networks, indicating significant topographic control on precipitation patterns and resulting geomorphic work (Scanlon et al., 2013)[269]. While ice flow modeling is crucial in studying the ancient Martian climate (Wordsworth et al., 2013; Fastook and Head, 2014)[270, 271], our model and analyses could also be leveraged to investigate the geomorphic connections and hydraulic influence of topography on early Mars, adding to the current arsenal of Martian GCMs (e.g. Wordsworth et al., 2013; Forget et al., 2013; Mischna et al., 2013; Urata and Toon, 2013; Soto et al., 2015; Wordsworth et al., 2015)[270, 272, 273, 274, 275, 276]. Indeed, work to extend TAM to other planetary environments has already begun, with the model having been used recently to explore Titan-like exoplanets around varying star types (Lora et al., 2018)[277].

Throughout this work, we have emphasized the role of climate in controlling regional surface expression, and neglected other likely factors such as lithology and tectonics. Evidence for tectonic activity on Titan exists in the form of mountains (Radebaugh et al., 2007; Mitri et al., 2010)[278, 279], faults and canyons (Solomonidou et al., 2013)[280], and river organization (Cartwright et al., 2011; Burr et al., 2013b)[281, 122]. Such tectonics may be driven by internal cooling or tidal flexing and need not be connected to a geologically active interior (Moore and Pappalardo, 2011)[282], but, in either case, tectonics capable of diverting flow are far from being included in a Titan GCM. Lithology presents another difficulty, particularly since our limited access to Titan's surface conceals the nature of its composition. Radiometer (e.g. Janssen et al., 2016)[283] and VIMS (e.g. Barnes et al., 2007; Soderblom et al., 2007, etc.)[284, 285] observations can distinguish surface material units and hint at possible constitutions, including exposed water ice bedrock, hydrocarbon and nitrile grains, and tholin aerosol dust. But uncertainties in these categorizations remain, notwithstanding their impact on fluid runoff and geomorphic feature production (Litwin et al., 2012)[97]. The relationship between lithology and sediment transport is even unclear on Earth (e.g. Hurst et al., 2013)[286], further confounding geomorphic interpretations for Titan.

As soil parameters for Titan are further constrained and our surface hydrology model is refined to include groundwater flow based on physical parameters such as soil transmissivity,

the GCM presented in this dissertation can be applied to more particular questions regarding Titan's climate. For instance, just as individual rainstorms were tracked in Chapter 3 to assess the regional potential for geomorphic work, with knowledge of surface materials and with a full surface hydrology scheme in place, these rainstorms could be further examined to calculate physically consistent erosion rates—potentially updating or confirming previous estimates and constraints (Black et al., 2012; Moore et al., 2014)[94, 120]. Other points of interest the model could tackle include: the evolution of paleobasins; the sources and characteristics of ephemeral lakes; comparisons of Titanian geomorphic relationships against equivalent terrestrial relationships, such as the rainfall intensity-duration control on landslides (Caine, 1980)[287]; the existence of dynamic subsurface hydrocarbon storage that might include unsaturated flow (Hewlett and Hibbert, 1963)[288]; and further rainfall and runoff variability analyses, with a particular focus on regional influences on sheetflood and/or debris flow formations (e.g. Cartwright and Burr, 2017)[84]. A full model with heterogeneous soil properties and updated flow procedures—as well as, in the atmosphere, resolved clouds (e.g. Rafkin and Barth, 2015)[13], an improved moist convection scheme that includes entrainment (Sahany et al., 2012)[289], coupled topography, and incorporated ethane—would help address these questions. Such additions would improve our understanding of not just Titan's climate, but also its paleoclimate and the past and present climates of other planetary bodies as well—bodies that, like Earth and like Titan, are terrestrial and tempestuous and dynamically interlaced within themselves, tethered and whole.

REFERENCES

[1] Roe, H. G. Titan's methane weather. *Annual Review of Earth and Planetary Sciences* **40**, 355–382 (2012).

[2] Ricker, G. R. *et al.* Transiting Exoplanet Survey Satellite (TESS). In *Bulletin of the American Astronomical Society*, vol. 42, 459 (2010).

[3] Niemann, H. *et al.* The abundances of constituents of Titan's atmosphere from the GCMS instrument on the Huygens probe. *Nature* **438**, 779–784 (2005).

[4] Fulchignoni, M. *et al.* In situ measurements of the physical characteristics of Titan's environment. *Nature* **438**, 785–791 (2005).

[5] Barth, E. L. & Rafkin, S. C. R. TRAMS: A new dynamic cloud model for Titan's methane clouds. *Geophysical Research Letters* **34** (2007). URL `http://dx.doi.org/10.1029/2006GL028652`. L03203.

[6] Barth, E. L. & Rafkin, S. C. Convective cloud heights as a diagnostic for methane environment on Titan. *Icarus* **206**, 467–484 (2010).

[7] Griffith, C. A., McKay, C. P. & Ferri, F. Titan's tropical storms in an evolving atmosphere. *The Astrophysical Journal Letters* **687**, L41 (2008).

[8] Schinder, P. J. *et al.* The structure of Titan's atmosphere from Cassini radio occultations. *Icarus* **215**, 460–474 (2011).

[9] Tokano, T. Meteorological assessment of the surface temperatures on Titan: Constraints on the surface type. *Icarus* **173**, 222–242 (2005).

[10] Lorenz, R. D., Griffith, C. A., Lunine, J. I., McKay, C. P. & Rennò, N. O. Convective plumes and the scarcity of Titan's clouds. *Geophysical Research Letters* **32** (2005).

[11] Hueso, R. & Sánchez-Lavega, A. Methane storms on Saturn's moon Titan. *Nature* **442**, 428–431 (2006).

[12] Mitchell, J. L., Pierrehumbert, R. T., Frierson, D. M. & Caballero, R. The impact of methane thermodynamics on seasonal convection and circulation in a model Titan atmosphere. *Icarus* **203**, 250–264 (2009).

[13] Rafkin, S. C. & Barth, E. Environmental control of deep convective clouds on Titan: The combined effect of CAPE and wind shear on storm dynamics, morphology, and lifetime. *Journal of Geophysical Research: Planets* **120**, 739–759 (2015).

[14] Griffith, C., Rafkin, S., Rannou, P. & McKay, C. Storms, clouds, and weather. In *Titan*, 190 (Cambridge University Press, 2014).

[15] Griffith, C. A., Hall, J. L. & Geballe, T. R. Detection of daily clouds on Titan. *Science* **290**, 509–513 (2000).

[16] Brown, M. E., Bouchez, A. H. & Griffith, C. A. Direct detection of variable tropospheric clouds near Titan's south pole. *Nature* **420**, 795–797 (2002).

[17] Roe, H., De Pater, I., Macintosh, B. & McKay, C. Titan's clouds from Gemini1 and Keck2 adaptive optics imaging. *Astrophy. J* **581**, 1399–1406 (2002).

[18] Bouchez, A. H. & Brown, M. E. Statistics of Titan's south polar tropospheric clouds. *The Astrophysical Journal Letters* **618**, L53 (2005).

[19] Schaller, E. L., Brown, M. E., Roe, H. G. & Bouchez, A. H. A large cloud outburst at Titan's south pole. *Icarus* **182**, 224–229 (2006).

[20] Griffith, C. *et al.* The evolution of Titan's mid-latitude clouds. *Science* **310**, 474–477 (2005).

[21] Porco, C. C. *et al.* Imaging of Titan from the Cassini spacecraft. *Nature* **434**, 159–168 (2005).

[22] Roe, H., Bouchez, A., Trujillo, C., Schaller, E. & Brown, M. Discovery of temperate latitude clouds on Titan. *The Astrophysical Journal Letters* **618**, L49 (2005).

[23] Schaller, E. L., Brown, M. E., Roe, H. G., Bouchez, A. H. & Trujillo, C. A. Dissipation of titan's south polar clouds. *Icarus* **184**, 517–523 (2006).

[24] Rodriguez, S. *et al.* Global circulation as the main source of cloud activity on Titan. *Nature* **459**, 678–682 (2009).

[25] Brown, M. E., Roberts, J. E. & Schaller, E. L. Clouds on Titan during the Cassini prime mission: A complete analysis of the VIMS data. *Icarus* **205**, 571–580 (2010).

[26] Turtle, E. *et al.* Seasonal changes in Titan's meteorology. *Geophysical Research Letters* **38** (2011).

[27] Rodriguez, S. *et al.* Titan's cloud seasonal activity from winter to spring with Cassini/VIMS. *Icarus* **216**, 89–110 (2011).

[28] Schaller, E., Roe, H., Schneider, T. & Brown, M. Storms in the tropics of Titan. *Nature* **460**, 873–875 (2009).

[29] Turtle, E. *et al.* Rapid and extensive surface changes near Titan's equator: Evidence of April showers. *Science* **331**, 1414–1417 (2011).

[30] Mitchell, J. L., Pierrehumbert, R. T., Frierson, D. M. & Caballero, R. The dynamics behind Titan's methane clouds. *Proceedings of the National Academy of Sciences* **103**, 18421–18426 (2006).

[31] Turtle, E. *et al.* Seasonal evolution in the behavior of Titans clouds from Cassign ISS, 2004-2017. In *European Planetary Science Congress 2017*, vol. 11, EPSC2017–352–1 (2017). URL `http://meetingorganizer.copernicus.org/EPSC2017/EPSC2017-352-1.pdf`.

[32] Schinder, P. J. *et al.* The structure of Titan's atmosphere from Cassini radio occultations: Occultations from the Prime and Equinox missions. *Icarus* **221**, 1020–1031 (2012).

[33] Jennings, D. *et al.* Titan's surface brightness temperatures. *The Astrophysical Journal Letters* **691**, L103 (2009).

[34] Jennings, D. *et al.* Surface temperatures on Titan during northern winter and spring. *The Astrophysical Journal Letters* **816**, L17 (2016).

[35] Samuelson, R. E., Nath, N. R. & Borysow, A. Gaseous abundances and methane supersaturation in Titan's troposphere. *Planetary and Space Science* **45**, 959–980 (1997).

[36] Schneider, T. The general circulation of the atmosphere. *Annual Review of Earth and Planetary Sciences* **34**, 655–688 (2006).

[37] Held, I. M. & Hou, A. Y. Nonlinear axially symmetric circulations in a nearly inviscid atmosphere. *Journal of the Atmospheric Sciences* **37**, 515–533 (1980).

[38] Mitchell, J. L. & Lora, J. M. The climate of Titan. *Annual Review of Earth and Planetary Sciences* **44**, 353–380 (2016).

[39] Walker, C. C. & Schneider, T. Eddy influences on Hadley circulations: Simulations with an idealized GCM. *Journal of the Atmospheric Sciences* **63**, 3333–3350 (2006).

[40] Bordoni, S. & Schneider, T. Monsoons as eddy-mediated regime transitions of the tropical overturning circulation. *Nature Geoscience* **1**, 515–519 (2008).

[41] Schneider, T. & Bordoni, S. Eddy-mediated regime transitions in the seasonal cycle of a Hadley circulation and implications for monsoon dynamics. *Journal of the Atmospheric Sciences* **65**, 915–934 (2008).

[42] Levine, X. J. & Schneider, T. Baroclinic eddies and the extent of the Hadley circulation: An idealized GCM study. *Journal of the Atmospheric Sciences* **72**, 2744–2761 (2015).

[43] Lora, J. M. & Mitchell, J. L. Titan's asymmetric lake distribution mediated by methane transport due to atmospheric eddies. *Geophysical Research Letters* **42**, 6213–6220 (2015).

[44] Mitchell, J. Titan's transport-driven methane cycle. *The Astrophysical Journal Letters* **756**, L26 (2012).

[45] Flasar, F. & Achterberg, R. The structure and dynamics of Titan's middle atmosphere. *Philosophical Transactions of the Royal Society of London A: Mathematical, Physical and Engineering Sciences* **367**, 649–664 (2009).

[46] Sobel, A. H. & Neelin, J. D. The boundary layer contribution to intertropical convergence zones in the quasi-equilibrium tropical circulation model framework. *Theoretical and Computational Fluid Dynamics* **20**, 323–350 (2006).

[47] Neelin, J. D. & Held, I. M. Modeling tropical convergence based on the moist static energy budget. *Monthly Weather Review* **115**, 3–12 (1987).

[48] Privé, N. C. & Plumb, R. A. Monsoon dynamics with interactive forcing. Part I: Axisymmetric studies. *Journal of the atmospheric sciences* **64**, 1417–1430 (2007).

[49] Kang, S. M., Held, I. M., Frierson, D. M. & Zhao, M. The response of the ITCZ to extratropical thermal forcing: Idealized slab-ocean experiments with a GCM. *Journal of Climate* **21**, 3521–3532 (2008).

[50] Schneider, T., Bischoff, T. & Haug, G. H. Migrations and dynamics of the intertropical convergence zone. *Nature* **513**, 45–53 (2014).

[51] Tokano, T. *et al.* Methane drizzle on Titan. *Nature* **442**, 432–435 (2006).

[52] Hayes, A. G. The lakes and seas of Titan. *Annual Review of Earth and Planetary Sciences* **44**, 57–83 (2016).

[53] Glein, C. R. & Shock, E. L. A geochemical model of non-ideal solutions in the methane–ethane–propane–nitrogen–acetylene system on Titan. *Geochimica et Cosmochimica Acta* **115**, 217–240 (2013).

[54] Tan, S. P. *et al.* Titan's liquids: Exotic behavior and its implications on global fluid circulation. *Icarus* **250**, 64–75 (2015).

[55] Mastrogiuseppe, M. *et al.* Radar sounding using the Cassini altimeter: waveform modeling and Monte Carlo approach for data inversion of observations of Titan's seas. *IEEE Transactions on Geoscience and Remote Sensing* **54**, 5646–5656 (2016).

[56] Stofan, E. *et al.* The lakes of Titan. *Nature* **445**, 61–64 (2007).

[57] Hayes, A. *et al.* Hydrocarbon lakes on Titan: Distribution and interaction with a porous regolith. *Geophysical Research Letters* **35** (2008).

[58] Aharonson, O. *et al.* An asymmetric distribution of lakes on Titan as a possible consequence of orbital forcing. *Nature Geoscience* **2**, 851–854 (2009).

[59] Lora, J., Lunine, J., Russell, J. & Hayes, A. Simulations of Titan's paleoclimate. *Icarus* **243**, 264–273 (2014).

[60] Liu, J. & Schneider, T. Contrasting responses to orbital precession on Titan and Earth. *Geophysical Research Letters* **43**, 7774–7780 (2016).

[61] Turtle, E. *et al.* Cassini imaging of Titan's high-latitude lakes, clouds, and south-polar surface changes. *Geophysical Research Letters* **36** (2009).

[62] Wall, S. *et al.* Active shoreline of Ontario Lacus, Titan: A morphological study of the lake and its surroundings. *Geophysical Research Letters* **37** (2010). URL `http://dx.doi.org/10.1029/2009GL041821`. L05202.

[63] Hayes, A. *et al.* Topographic constraints on the evolution and connectivity of Titan's lacustrine basins. *Geophysical Research Letters* **44** (2017).

[64] Birch, S. *et al.* Morphological evidence that Titan's southern hemisphere basins are paleoseas. *Icarus* (2017).

[65] Barnes, J. *et al.* Organic sedimentary deposits in Titan's dry lakebeds: Probable evaporite. *Icarus* **216**, 136–140 (2011).

[66] Barnes, J. W. *et al.* Shoreline features of Titan's Ontario Lacus from Cassini/VIMS observations. *Icarus* **201**, 217–225 (2009).

[67] MacKenzie, S. M. *et al.* Evidence of Titan's climate history from evaporite distribution. *Icarus* **243**, 191–207 (2014).

[68] Griffith, C. A. *et al.* Possible tropical lakes on Titan from observations of dark terrain. *Nature* **486**, 237–239 (2012).

[69] Vixie, G. *et al.* Possible temperate lakes on Titan. *Icarus* **257**, 313–323 (2015).

[70] Lorenz, R. *et al.* The sand seas of Titan: Cassini RADAR observations of longitudinal dunes. *Science* **312**, 724–727 (2006).

[71] Radebaugh, J. *et al.* Dunes on Titan observed by Cassini RADAR. *Icarus* **194**, 690–703 (2008).

[72] Le Gall, A. *et al.* Cassini SAR, radiometry, scatterometry and altimetry observations of Titan's dune fields. *Icarus* **213**, 608–624 (2011).

[73] Dhingra, R. D., Barnes, J. W., Yanites, B. J. & Kirk, R. L. Large catchment area recharges Titan's Ontario Lacus. *Icarus* **299**, 331–338 (2018).

[74] Tomasko, M. *et al.* Rain, winds and haze during the Huygens probe's descent to Titan's surface. *Nature* **438**, 765–778 (2005).

[75] Elachi, C. *et al.* Cassini radar views the surface of Titan. *Science* **308**, 970–974 (2005).

[76] Lorenz, R. *et al.* Fluvial channels on Titan: Initial Cassini RADAR observations. *Planetary and Space Science* **56**, 1132–1144 (2008).

[77] Lunine, J. & Lorenz, R. Rivers, lakes, dunes, and rain: Crustal processes in Titan's methane cycle. *Annual Review of Earth and Planetary Sciences* **37**, 299–320 (2009).

[78] Le Gall, A. *et al.* Radar-bright channels on Titan. *Icarus* **207**, 948–958 (2010).

[79] Lopes, R. *et al.* Distribution and interplay of geologic processes on Titan from Cassini Radar data. *Icarus* **205**, 540–558 (2010).

[80] Langhans, M. *et al.* Titan's fluvial valleys: Morphology, distribution, and spectral properties. *Planetary and Space Science* **60**, 34–51 (2012).

[81] Burr, D. M. *et al.* Fluvial features on Titan: Insights from morphology and modeling. *Geological Society of America Bulletin* **125**, 299–321 (2013).

[82] Birch, S., Hayes, A., Howard, A., Moore, J. & Radebaugh, J. Alluvial fan morphology, distribution and formation on Titan. *Icarus* **270**, 238–247 (2016).

[83] Radebaugh, J. *et al.* Alluvial and fluvial fans on Saturn's moon Titan reveal processes, materials and regional geology. *Geological Society, London, Special Publications* **440**, SP440–6 (2016).

[84] Cartwright, R. & Burr, D. Using synthetic aperture radar data of terrestrial analogs to test for alluvial fan formation mechanisms on Titan. *Icarus* **284**, 183–205 (2017).

[85] Lopes, R. M. *et al.* Nature, distribution, and origin of Titan's Undifferentiated Plains. *Icarus* **270**, 162–182 (2016).

[86] Wood, C. *et al.* Impact craters on Titan. *Icarus* **206**, 334–344 (2010).

[87] Neish, C. & Lorenz, R. Titan's global crater population: A new assessment. *Planetary and Space Science* **60**, 26–33 (2012).

[88] Lorenz, R. *et al.* A global topographic map of Titan. *Icarus* **225**, 367–377 (2013).

[89] Corlies, P. *et al.* Titan's Topography and Shape at the End of the Cassini Mission. *Geophysical Research Letters* **44** (2017).

[90] Neish, C. & Lorenz, R. Elevation distribution of Titan's craters suggests extensive wetlands. *Icarus* **228**, 27–34 (2014).

[91] Neish, C. *et al.* Fluvial erosion as a mechanism for crater modification on Titan. *Icarus* **270**, 114–129 (2016).

[92] Perron, J. *et al.* Valley formation and methane precipitation rates on Titan. *Journal of Geophysical Research: Planets (1991–2012)* **111** (2006).

[93] Jaumann, R. *et al.* Fluvial erosion and post-erosional processes on Titan. *Icarus* **197**, 526–538 (2008).

[94] Black, B., Perron, J., Burr, D. & Drummond, S. Estimating erosional exhumation on Titan from drainage network morphology. *Journal of Geophysical Research: Planets (1991–2012)* **117** (2012).

[95] Collins, G. Relative rates of fluvial bedrock incision on Titan and Earth. *Geophysical Research Letters* **32** (2005).

[96] Burr, D., Emery, J., Lorenz, R., Collins, G. & Carling, P. Sediment transport by liquid surficial flow: Application to Titan. *Icarus* **181**, 235–242 (2006).

[97] Litwin, K. L., Zygielbaum, B. R., Polito, P. J., Sklar, L. S. & Collins, G. C. Influence of temperature, composition, and grain size on the tensile failure of water ice: Implications for erosion on Titan. *Journal of Geophysical Research: Planets* **117** (2012). URL `http://dx.doi.org/10.1029/2012JE004101`. E08013.

[98] Schneider, T., Graves, S., Schaller, E. & Brown, M. Polar methane accumulation and rainstorms on Titan from simulations of the methane cycle. *Nature* **481**, 58–61 (2012).

[99] Lora, J., Lunine, J. & Russell, J. GCM simulations of Titans middle and lower atmosphere and comparison to observations. *Icarus* (2015).

[100] Newman, C., Richardson, M., Lian, Y. & Lee, C. Simulating Titan's methane cycle with the TitanWRF General Circulation Model. *Icarus* **267**, 106–134 (2016).

[101] Perron, J. T. Climate and the pace of erosional landscape evolution. *Annual Review of Earth and Planetary Sciences* **45** (2017).

[102] Whipple, K. X. & Tucker, G. E. Dynamics of the stream-power river incision model: Implications for height limits of mountain ranges, landscape response timescales, and research needs. *Journal of Geophysical Research: Solid Earth* **104**, 17661–17674 (1999).

[103] Seybold, H., Rothman, D. H. & Kirchner, J. W. Climate's watermark in the geometry of stream networks. *Geophysical Research Letters* **44**, 2272–2280 (2017).

[104] Molnar, P., Anderson, R. S., Kier, G. & Rose, J. Relationships among probability distributions of stream discharges in floods, climate, bed load transport, and river incision. *Journal of Geophysical Research: Earth Surface* **111** (2006).

[105] DiBiase, R. A. & Whipple, K. X. The influence of erosion thresholds and runoff variability on the relationships among topography, climate, and erosion rate. *Journal of Geophysical Research: Earth Surface* **116** (2011).

[106] Ferrier, K. L., Huppert, K. L. & Perron, J. T. Climatic control of bedrock river incision. *Nature* **496**, 206–209 (2013).

[107] Blair, T. C. & McPherson, J. G. Alluvial fan processes and forms. In *Geomorphology of Desert Environments*, 354–402 (Springer, 1994).

[108] Borga, M., Stoffel, M., Marchi, L., Marra, F. & Jakob, M. Hydrogeomorphic response to extreme rainfall in headwater systems: Flash floods and debris flows. *Journal of Hydrology* **518**, 194–205 (2014).

[109] Cook, T. L., Yellen, B. C., Woodruff, J. D. & Miller, D. Contrasting human versus climatic impacts on erosion. *Geophysical Research Letters* **42**, 6680–6687 (2015).

[110] D'Arcy, M., D.C., R.-B. & Whittaker, A. Glacial-interglacial climate changes recorded by debris flow deposits, Owens Valley, California. *Quaternary Science Reviews* **169**, 288–311 (2017).

[111] Wolman, M. G. & Miller, J. P. Magnitude and frequency of forces in geomorphic processes. *The Journal of Geology* 54–74 (1960).

[112] Tucker, G. E. & Bras, R. L. A stochastic approach to modeling the role of rainfall variability in drainage basin evolution. *Water Resources Research* **36**, 1953–1964 (2000).

[113] Baker, V. R. Planetary geomorphology. *Journal of Geological Education* **32**, 236–246 (1984).

[114] Milton, D. J. Water and processes of degradation in the Martian landscape. *Journal of Geophysical Research* **78**, 4037–4047 (1973).

[115] Baker, V. R. & Milton, D. J. Erosion by catastrophic floods on Mars and Earth. *Icarus* **23**, 27–41 (1974).

[116] Craddock, R. A. & Howard, A. D. The case for rainfall on a warm, wet early Mars. *Journal of Geophysical Research: Planets* **107** (2002).

[117] Moore, J. M. & Howard, A. D. Large alluvial fans on Mars. *Journal of Geophysical Research: Planets* **110** (2005). URL `http://dx.doi.org/10.1029/2004JE002352`. E04005.

[118] Hynek, B. M., Beach, M. & Hoke, M. R. Updated global map of Martian valley networks and implications for climate and hydrologic processes. *Journal of Geophysical Research: Planets* **115** (2010).

[119] Jacobsen, R. & Burr, D. Greater contrast in Martian hydrological history from more accurate estimates of paleodischarge. *Geophysical Research Letters* **43**, 8903–8911 (2016).

[120] Moore, J. M., Howard, A. D. & Morgan, A. M. The landscape of Titan as witness to its climate evolution. *Journal of Geophysical Research: Planets* **119**, 2060–2077 (2014).

[121] Birch, S. *et al.* Geomorphologic mapping of Titan's polar terrains: Constraining surface processes and landscape evolution. *Icarus* **282**, 214–236 (2017).

[122] Burr, D. M., Drummond, S. A., Cartwright, R., Black, B. A. & Perron, J. T. Morphology of fluvial networks on Titan: Evidence for structural control. *Icarus* **226**, 742–759 (2013).

[123] Black, B. A. *et al.* Global drainage patterns and the origins of topographic relief on Earth, Mars, and Titan. *Science* **356**, 727–731 (2017).

[124] Lopes, R. *et al.* Cryovolcanism on Titan: New results from Cassini RADAR and VIMS. *Journal of Geophysical Research: Planets* **118**, 416–435 (2013).

[125] Leier, A. L., DeCelles, P. G. & Pelletier, J. D. Mountains, monsoons, and megafans. *Geology* **33**, 289–292 (2005).

[126] Gibling, M., Tandon, S., Sinha, R. & Jain, M. Discontinuity-bounded alluvial sequences of the southern Gangetic Plains, India: Aggradation and degradation in response to monsoonal strength. *Journal of Sedimentary Research* **75**, 369–385 (2005).

[127] Yung, Y. L., Allen, M. & Pinto, J. P. Photochemistry of the atmosphere of Titan-Comparison between model and observations. *The Astrophysical Journal Supplement Series* **55**, 465–506 (1984).

[128] Atreya, S. K. *et al.* Titan's methane cycle. *Planetary and Space Science* **54**, 1177–1187 (2006).

[129] Lorenz, R. D. *et al.* Titan's inventory of organic surface materials. *Geophysical Research Letters* **35** (2008).

[130] Tobie, G., Lunine, J. I. & Sotin, C. Episodic outgassing as the origin of atmospheric methane on Titan. *Nature* **440**, 61–64 (2006).

[131] Lebreton, J.-P. *et al.* An overview of the descent and landing of the Huygens probe on Titan. *Nature* **438**, 758–764 (2005).

[132] Zarnecki, J. *et al.* A soft solid surface on Titan as revealed by the Huygens Surface Science Package. *Nature* **438**, 792–795 (2005).

[133] Lorenz, R., Niemann, H., Harpold, D., Way, S. & Zarnecki, J. Titan's damp ground: Constraints on Titan surface thermal properties from the temperature evolution of the Huygens GCMS inlet. *Meteoritics & Planetary Science* **41**, 1705–1714 (2006).

[134] Liu, Z. Y.-C., Radebaugh, J., Harris, R. A., Christiansen, E. H. & Rupper, S. Role of fluids in the tectonic evolution of Titan. *Icarus* **270**, 2–13 (2016).

[135] Ádámkovics, M. *et al.* Meridional variation in tropospheric methane on Titan observed with AO spectroscopy at Keck and VLT. *Icarus* **270**, 376–388 (2016).

[136] Lora, J. M. & Ádámkovics, M. The near-surface methane humidity on titan. *Icarus* **286**, 270–279 (2017).

[137] Rannou, P., Montmessin, F., Hourdin, F. & Lebonnois, S. The latitudinal distribution of clouds on Titan. *Science* **311**, 201–205 (2006).

[138] Mitchell, J. The drying of Titan's dunes: Titan's methane hydrology and its impact on atmospheric circulation. *Journal of Geophysical Research: Planets (1991–2012)* **113** (2008).

[139] Horvath, D. G., Andrews-Hanna, J. C., Newman, C. E., Mitchell, K. L. & Stiles, B. W. The influence of subsurface flow on lake formation and north polar lake distribution on Titan. *Icarus* **277**, 103–124 (2016).

[140] Frierson, D. M. The dynamics of idealized convection schemes and their effect on the zonally averaged tropical circulation. *Journal of the Atmospheric Sciences* **64**, 1959–1976 (2007).

[141] Brown, R. G. & Bretherton, C. S. A test of the strict quasi-equilibrium theory on long time and space scales. *Journal of the Atmospheric Sciences* **54**, 624–638 (1997).

[142] Bretherton, C. S., Peters, M. E. & Back, L. E. Relationships between water vapor path and precipitation over the tropical oceans. *Journal of Climate* **17**, 1517–1528 (2004).

[143] Toon, O. B., McKay, C., Ackerman, T. & Santhanam, K. Rapid calculation of radiative heating rates and photodissociation rates in inhomogeneous multiple scattering atmospheres. *Journal of Geophysical Research: Atmospheres* **94**, 16287–16301 (1989).

[144] Tomasko, M., Bézard, B., Doose, L., Engel, S. & Karkoschka, E. Measurements of methane absorption by the descent imager/spectral radiometer (DISR) during its descent through Titan's atmosphere. *Planetary and Space Science* **56**, 624–647 (2008).

[145] Rothman, L. S. *et al.* The HITRAN 2008 molecular spectroscopic database. *Journal of Quantitative Spectroscopy and Radiative Transfer* **110**, 533–572 (2009).

[146] Richard, C. *et al.* New section of the HITRAN database: Collision-induced absorption (CIA). *Journal of Quantitative Spectroscopy and Radiative Transfer* **113**, 1276–1285 (2012).

[147] Rothman, L. S. *et al.* The HITRAN molecular spectroscopic database and HAWKS (HITRAN Atmospheric Workstation): 1996 edition. *Journal of Quantitative Spectroscopy and Radiative Transfer* **60**, 665–710 (1998).

[148] Vinatier, S. *et al.* Vertical abundance profiles of hydrocarbons in Titan's atmosphere at 15 S and 80 N retrieved from Cassini/CIRS spectra. *Icarus* **188**, 120–138 (2007).

[149] Tomasko, M. *et al.* A model of Titan's aerosols based on measurements made inside the atmosphere. *Planetary and Space Science* **56**, 669–707 (2008).

[150] Anderson, C. M. & Samuelson, R. E. Titan's aerosol and stratospheric ice opacities between 18 and 500 μm: Vertical and spectral characteristics from Cassini CIRS. *Icarus* **212**, 762–778 (2011).

[151] Vinatier, S. *et al.* Optical constants of Titan's stratospheric aerosols in the 70–1500 cm- 1 spectral range constrained by Cassini/CIRS observations. *Icarus* **219**, 5–12 (2012).

[152] Frierson, D. M., Held, I. M. & Zurita-Gotor, P. A gray-radiation aquaplanet moist GCM. Part I: Static stability and eddy scale. *Journal of the Atmospheric Sciences* **63**, 2548–2566 (2006).

[153] Held, I. M. & Suarez, M. J. A proposal for the intercomparison of the dynamical cores of atmospheric general circulation models. *Bulletin of the American Meteorological Society* **75**, 1825–1830 (1994).

[154] Faulk, S., Mitchell, J. & Bordoni, S. Effects of rotation rate and seasonal forcing on the ITCZ extent in planetary atmospheres. *Journal of the Atmospheric Sciences* **74**, 665–678 (2017).

[155] Faulk, S., Mitchell, J., Moon, S. & Lora, J. Regional patterns of extreme precipitation on Titan consistent with observed alluvial fan distribution. *Nature Geoscience* **10**, 827 (2017).

[156] Waliser, D. E. & Gautier, C. A satellite-derived climatology of the ITCZ. *Journal of Climate* **6**, 2162–2174 (1993).

[157] Yihui, D. & Chan, J. C. The East Asian summer monsoon: An overview. *Meteorology and Atmospheric Physics* **89**, 117–142 (2005).

[158] Janowiak, J. E., Arkin, P. A., Xie, P., Morrissey, M. L. & Legates, D. R. An examination of the east Pacific ITCZ rainfall distribution. *Journal of Climate* **8**, 2810–2823 (1995).

[159] Ramage, C. Structure of an oceanic near-equatorial trough deduced from research aircraft traverses. *Monthly Weather Review* **102**, 754–759 (1974).

[160] Sadler, J. C. The monsoon circulation and cloudiness over the GATE area. *Monthly Weather Review* **103**, 369–387 (1975).

[161] Waliser, D. E. & Somerville, R. C. Preferred latitudes of the intertropical convergence zone. *Journal of the Atmospheric Sciences* **51**, 1619–1639 (1994).

[162] Sobel, A. H., Nilsson, J. & Polvani, L. M. The weak temperature gradient approximation and balanced tropical moisture waves. *Journal of the Atmospheric Sciences* **58**, 3650–3665 (2001).

[163] Raymond, D. J. Thermodynamic control of tropical rainfall. *Quarterly Journal of the Royal Meteorological Society* **126**, 889–898 (2000).

[164] Sobel, A. H. & Bretherton, C. S. Modeling tropical precipitation in a single column. *Journal of Climate* **13**, 4378–4392 (2000).

[165] Lindzen, R. S. & Hou, A. V. Hadley circulations for zonally averaged heating centered off the equator. *Journal of the Atmospheric Sciences* **45**, 2416–2427 (1988).

[166] Arakawa, A. & Schubert, W. H. Interaction of a cumulus cloud ensemble with the large-scale environment, Part I. *Journal of the Atmospheric Sciences* **31**, 674–701 (1974).

[167] Emanuel, K. A., David Neelin, J. & Bretherton, C. S. On large-scale circulations in convecting atmospheres. *Quarterly Journal of the Royal Meteorological Society* **120**, 1111–1143 (1994).

[168] Nie, J., Boos, W. R. & Kuang, Z. Observational evaluation of a convective quasi-equilibrium view of monsoons. *Journal of Climate* **23**, 4416–4428 (2010).

[169] Emanuel, K. A. On thermally direct circulations in moist atmospheres. *Journal of the Atmospheric Sciences* **52**, 1529–1534 (1995).

[170] Chiang, J. C. & Bitz, C. M. Influence of high latitude ice cover on the marine Intertropical Convergence Zone. *Climate Dynamics* **25**, 477–496 (2005).

[171] Broccoli, A. J., Dahl, K. A. & Stouffer, R. J. Response of the ITCZ to Northern Hemisphere cooling. *Geophysical Research Letters* **33** (2006).

[172] Kang, S. M., Frierson, D. M. & Held, I. M. The tropical response to extratropical thermal forcing in an idealized GCM: The importance of radiative feedbacks and convective parameterization. *Journal of the Atmospheric Sciences* **66**, 2812–2827 (2009).

[173] Chiang, J. C. & Friedman, A. R. Extratropical cooling, interhemispheric thermal gradients, and tropical climate change. *Annual Review of Earth and Planetary Sciences* **40**, 383 (2012).

[174] Frierson, D. M. & Hwang, Y.-T. Extratropical influence on ITCZ shifts in slab ocean simulations of global warming. *Journal of Climate* **25**, 720–733 (2012).

[175] Donohoe, A., Marshall, J., Ferreira, D. & Mcgee, D. The relationship between ITCZ location and cross-equatorial atmospheric heat transport: From the seasonal cycle to the Last Glacial Maximum. *Journal of Climate* **26**, 3597–3618 (2013).

[176] Frierson, D. M. *et al.* Contribution of ocean overturning circulation to tropical rainfall peak in the Northern Hemisphere. *Nature Geoscience* **6**, 940–944 (2013).

[177] Bischoff, T. & Schneider, T. Energetic constraints on the position of the intertropical convergence zone. *Journal of Climate* **27**, 4937–4951 (2014).

[178] Adam, O., Bischoff, T. & Schneider, T. Seasonal and interannual variations of the energy flux equator and ITCZ. part I: Zonally averaged ITCZ position. *Journal of Climate* **29**, 3219–3230 (2016).

[179] Bischoff, T. & Schneider, T. The equatorial energy balance, ITCZ position, and double-ITCZ bifurcations. *Journal of Climate* **29**, 2997–3013 (2016).

[180] Shekhar, R. & Boos, W. R. Improving energy-based estimates of monsoon location in the presence of proximal deserts. *Journal of Climate* **29**, 4741–4761 (2016).

[181] Lindzen, R. S. & Nigam, S. On the role of sea surface temperature gradients in forcing low-level winds and convergence in the tropics. *Journal of the Atmospheric Sciences* **44**, 2418–2436 (1987).

[182] Tomas, R. A. & Webster, P. J. The role of inertial instability in determining the location and strength of near-equatorial convection. *Quarterly Journal of the Royal Meteorological Society* **123**, 1445–1482 (1997).

[183] Pauluis, O. Boundary layer dynamics and cross-equatorial Hadley circulation. *Journal of the Atmospheric Sciences* **61**, 1161–1173 (2004).

[184] Back, L. E. & Bretherton, C. S. On the relationship between SST gradients, boundary layer winds, and convergence over the tropical oceans. *Journal of Climate* **22**, 4182–4196 (2009).

[185] Tomas, R. A., Holton, J. R. & Webster, P. J. The influence of cross-equatorial pressure gradients on the location of near-equatorial convection. *Quarterly Journal of the Royal Meteorological Society* **125**, 1107–1127 (1999).

[186] Toma, V. E. & Webster, P. J. Oscillations of the intertropical convergence zone and the genesis of easterly waves. Part I: diagnostics and theory. *Climate dynamics* **34**, 587–604 (2010).

[187] Chao, W. C. Multiple quasi equilibria of the ITCZ and the origin of monsoon onset. *Journal of the Atmospheric Sciences* **57**, 641–652 (2000).

[188] Chao, W. C. & Chen, B. Multiple quasi equilibria of the ITCZ and the origin of monsoon onset. Part II: Rotational ITCZ attractors. *Journal of the Atmospheric Sciences* **58**, 2820–2831 (2001).

[189] Pfeffer, R. L. Wave-mean flow interactions in the atmosphere. *Journal of the Atmospheric Sciences* **38**, 1340–1359 (1981).

[190] Becker, E., Schmitz, G. & Geprägs, R. The feedback of midlatitude waves onto the Hadley cell in a simple general circulation model. *Tellus A* **49**, 182–199 (1997).

[191] Walker, C. C. & Schneider, T. Response of idealized Hadley circulations to seasonally varying heating. *Geophysical Research Letters* **32** (2005).

[192] Merlis, T. M., Schneider, T., Bordoni, S. & Eisenman, I. Hadley circulation response to orbital precession. Part I: Aquaplanets. *Journal of Climate* **26**, 740–753 (2013).

[193] Levine, X. J. & Schneider, T. Response of the Hadley circulation to climate change in an aquaplanet GCM coupled to a simple representation of ocean heat transport. *Journal of the Atmospheric Sciences* **68**, 769–783 (2011).

[194] Satoh, M. Hadley circulations in radiative-convective equilibrium in an axially symmetric atmosphere. *Journal of the Atmospheric Sciences* **51**, 1947–1968 (1994).

[195] Caballero, R., Pierrehumbert, R. T. & Mitchell, J. L. Axisymmetric, nearly inviscid circulations in non-condensing radiative-convective atmospheres. *Quarterly Journal of the Royal Meteorological Society* **134**, 1269–1285 (2008).

[196] Plumb, R. A. & Hou, A. Y. The response of a zonally symmetric atmosphere to subtropical thermal forcing: Threshold behavior. *Journal of the Atmospheric Sciences* **49**, 1790–1799 (1992).

[197] Haberle, R. M. *et al.* Mars atmospheric dynamics as simulated by the NASA Ames General Circulation Model: I. The zonal-mean circulation. *Journal of Geophysical Research: Planets (1991–2012)* **98**, 3093–3123 (1993).

[198] Lewis, S. R. Modelling the Martian atmosphere. *Astronomy & Geophysics* **44**, 4–6 (2003).

[199] Williams, G. P. The dynamical range of global circulations: Part I. *Climate Dynamics* **2**, 205–260 (1988).

[200] Navarra, A. & Boccaletti, G. Numerical general circulation experiments of sensitivity to Earth rotation rate. *Climate Dynamics* **19**, 467–483 (2002).

[201] Mitchell, J. L. & Vallis, G. K. The transition to superrotation in terrestrial atmospheres. *Journal of Geophysical Research: Planets (1991–2012)* **115** (2010).

[202] Mitchell, J. L., Vallis, G. K. & Potter, S. F. Effects of the seasonal cycle on superrotation in planetary atmospheres. *The Astrophysical Journal* **787**, 23 (2014).

[203] Pinto, J. R. D. & Mitchell, J. L. Atmospheric superrotation in an idealized GCM: Parameter dependence of the eddy response. *Icarus* **238**, 93–109 (2014).

[204] Kaspi, Y. & Showman, A. P. Atmospheric dynamics of terrestrial exoplanets over a wide range of orbital and atmospheric parameters. *The Astrophysical Journal* **804**, 60 (2015).

[205] Frierson, D. M. Midlatitude static stability in simple and comprehensive general circulation models. *Journal of the Atmospheric Sciences* **65**, 1049–1062 (2008).

[206] Hartmann, D. L. *Global Physical Climatology*, vol. 56 (Academic Press, 1994).

[207] Fein, J. S. & Stephens, P. L. *Monsoons* (Wiley New York, 1987).

[208] Xie, S.-P. The shape of continents, air-sea interaction, and the rising branch of the Hadley circulation. In *The Hadley Circulation: Present, Past and Future*, 121–152 (Springer, 2004).

[209] Pierrehumbert, R. T. Climate dynamics of a hard snowball Earth. *Journal of Geophysical Research: Atmospheres* **110** (2005).

[210] Abbot, D. S. & Pierrehumbert, R. T. Mudball: Surface dust and snowball Earth deglaciation. *Journal of Geophysical Research: Atmospheres* **115** (2010).

[211] Donohoe, A., Frierson, D. M. & Battisti, D. S. The effect of ocean mixed layer depth on climate in slab ocean aquaplanet experiments. *Climate Dynamics* **43**, 1041–1055 (2014).

[212] Poggiali, V. *et al.* Liquid-filled canyons on Titan. *Geophysical Research Letters* **43**, 7887–7894 (2016).

[213] Arzani, N. Catchment lithology as a major control on alluvial megafan development, Kohrud Mountain range, central Iran. *Earth Surface Processes and Landforms* **37**, 726–740 (2012).

[214] Rossi, M. W., Whipple, K. X. & Vivoni, E. R. Precipitation and evapotranspiration controls on daily runoff variability in the contiguous United States and Puerto Rico. *Journal of Geophysical Research: Earth Surface* (2016).

[215] Mather, A., Stokes, M. & Whitfield, E. River terraces and alluvial fans: The case for an integrated Quaternary fluvial archive. *Quaternary Science Reviews* (2016).

[216] Iverson, R. M. Debris-flow mechanics. In *Debris-flow hazards and related phenomena*, 105–134 (Springer, 2005).

[217] Davidson, S. K., Hartley, A. J., Weissmann, G. S., Nichols, G. J. & Scuderi, L. A. Geomorphic elements on modern distributive fluvial systems. *Geomorphology* **180**, 82–95 (2013).

[218] Raulin, F., Brasse, C., Poch, O. & Coll, P. Prebiotic-like chemistry on Titan. *Chemical Society Reviews* **41**, 5380–5393 (2012).

[219] Hörst, S. M. Titan's atmosphere and climate. *Journal of Geophysical Research: Planets* **122**, 432–482 (2017).

[220] Cornet, T. *et al.* Dissolution on Titan and on Earth: Toward the age of Titan's karstic landscapes. *Journal of Geophysical Research: Planets* **120**, 1044–1074 (2015).

[221] Beaty, C. B. Age and estimated rate of accumulation of an alluvial fan, White Mountains, California, USA. *American Journal of Science* **268**, 50–77 (1970).

[222] Howard, A. D., Breton, S. & Moore, J. M. Formation of gravel pavements during fluvial erosion as an explanation for persistence of ancient cratered terrain on Titan and Mars. *Icarus* **270**, 100–113 (2016).

[223] Griffith, C. A. *et al.* Characterization of clouds in Titan's tropical atmosphere. *The Astrophysical Journal Letters* **702**, L105 (2009).

[224] Wilson, P. & Toumi, R. A fundamental probability distribution for heavy rainfall. *Geophysical Research Letters* **32** (2005).

[225] Lebonnois, S., Burgalat, J., Rannou, P. & Charnay, B. Titan global climate model: A new 3-dimensional version of the IPSL Titan GCM. *Icarus* **218**, 707–722 (2012).

[226] Malaska, M. J. *et al.* Geomorphological map of the Afekan Crater region, Titan: Terrain relationships in the equatorial and mid-latitude regions. *Icarus* **270**, 130–161 (2016).

[227] Manabe, S. Climate and the ocean circulation. *Mon. Wea. Rev* **97**, 739–774 (1969).

[228] Chen, F. & Dudhia, J. Coupling an advanced land surface–hydrology model with the Penn State–NCAR MM5 modeling system. Part I: Model implementation and sensitivity. *Monthly Weather Review* **129**, 569–585 (2001).

[229] Smith, D. E. *et al.* The global topography of Mars and implications for surface evolution. *Science* **284**, 1495–1503 (1999).

[230] Ford, P. G. & Pettengill, G. H. Venus topography and kilometer-scale slopes. *Journal of Geophysical Research: Planets* **97**, 13103–13114 (1992).

[231] Smrekar, S. E. *et al.* Recent hotspot volcanism on Venus from VIRTIS emissivity data. *Science* **328**, 605–608 (2010).

[232] Moore, J. M. *et al.* The geology of Pluto and Charon through the eyes of New Horizons. *Science* **351**, 1284–1293 (2016).

[233] Willett, S. D., McCoy, S. W., Perron, J. T., Goren, L. & Chen, C.-Y. Dynamic reorganization of river basins. *Science* **343**, 1248765 (2014).

[234] Hayes, A. *et al.* Transient surface liquid in Titan's polar regions from Cassini. *Icarus* **211**, 655–671 (2011).

[235] Turtle, E., Perry, J., Hayes, A. & McEwen, A. Shoreline retreat at Titan's Ontario Lacus and Arrakis Planitia from Cassini Imaging Science Subsystem observations. *Icarus* **212**, 957–959 (2011).

[236] Philip, J. R. Evaporation, and moisture and heat fields in the soil. *Journal of meteorology* **14**, 354–366 (1957).

[237] Shah, N., Nachabe, M. & Ross, M. Extinction depth and evapotranspiration from ground water under selected land covers. *Groundwater* **45**, 329–338 (2007).

[238] Johnson, E., Yáñez, J., Ortiz, C. & Muñoz, J. Evaporation from shallow groundwater in closed basins in the Chilean Altiplano. *Hydrological Sciences Journal–Journal des Sciences Hydrologiques* **55**, 624–635 (2010).

[239] Kurc, S. A. & Small, E. E. Dynamics of evapotranspiration in semiarid grassland and shrubland ecosystems during the summer monsoon season, central New Mexico. *Water Resources Research* **40** (2004).

[240] Cammeraat, E. L. Scale dependent thresholds in hydrological and erosion response of a semi-arid catchment in southeast Spain. *Agriculture, Ecosystems & Environment* **104**, 317–332 (2004).

[241] O'Callaghan, J. F. & Mark, D. M. The extraction of drainage networks from digital elevation data. *Computer Vision, Graphics, and Image Processing* **28**, 323–344 (1984).

[242] Tarboton, D. G. A new method for the determination of flow directions and upslope areas in grid digital elevation models. *Water Resources Research* **33**, 309–319 (1997).

[243] Freeman, T. G. Calculating catchment area with divergent flow based on a regular grid. *Computers & Geosciences* **17**, 413–422 (1991).

[244] Shelef, E. & Hilley, G. E. Impact of flow routing on catchment area calculations, slope estimates, and numerical simulations of landscape development. *Journal of Geophysical Research: Earth Surface* **118**, 2105–2123 (2013).

[245] Overton, D. Route or convolute? *Water Resources Research* **6**, 43–52 (1970).

[246] Watt, W. E. & Chow, K. A. A general expression for basin lag time. *Canadian Journal of Civil Engineering* **12**, 294–300 (1985).

[247] Liston, G., Sud, Y. & Wood, E. Evaluating GCM land surface hydrology parameterizations by computing river discharges using a runoff routing model: Application to the Mississippi basin. *Journal of Applied Meteorology* **33**, 394–405 (1994).

[248] Miller, J. R., Russell, G. L. & Caliri, G. Continental-scale river flow in climate models. *Journal of Climate* **7**, 914–928 (1994).

[249] Coe, M. T. Modeling terrestrial hydrological systems at the continental scale: Testing the accuracy of an atmospheric GCM. *Journal of Climate* **13**, 686–704 (2000).

[250] Wang, J. *et al.* The coupled routing and excess storage (CREST) distributed hydrological model. *Hydrological Sciences Journal* **56**, 84–98 (2011).

[251] Askew, A. J. Derivation of formulae for variable lag time. *Journal of Hydrology* **10**, 225–242 (1970).

[252] Singh, V. P. Hydrologic systems. Volume I: Rainfall-runoff modeling. *Prentice Hall, Englewood Cliffs New Jersey. 1988. 480* (1988).

[253] Vörösmarty, C. J. *et al.* Continental scale models of water balance and fluvial transport: An application to South America. *Global Biogeochemical Cycles* **3**, 241–265 (1989).

[254] Quinn, P., Beven, K., Chevallier, P. & Planchon, O. The prediction of hillslope flow paths for distributed hydrological modelling using digital terrain models. *Hydrological Processes* **5**, 59–79 (1991).

[255] Wigmosta, M. S., Vail, L. W. & Lettenmaier, D. P. A distributed hydrology-vegetation model for complex terrain. *Water Resources Research* **30**, 1665–1679 (1994).

[256] Wigmosta, M. S. & Lettenmaier, D. P. A comparison of simplified methods for routing topographically driven subsurface flow. *Water Resources Research* **35**, 255–264 (1999).

[257] Iess, L. *et al.* The tides of Titan. *Science* **337**, 457–459 (2012).

[258] Peixoto, J. P. & Oort, A. H. Physics of climate (1992).

[259] Trenberth, K. E. & Stepaniak, D. P. Covariability of components of poleward atmospheric energy transports on seasonal and interannual timescales. *Journal of Climate* **16**, 3691–3705 (2003).

[260] Zahnle, K. J., Korycansky, D. G. & Nixon, C. A. Transient climate effects of large impacts on Titan. *Icarus* **229**, 378–391 (2014).

[261] Lunine, J. I. & Atreya, S. K. The methane cycle on Titan. *Nature Geoscience* **1**, 159–164 (2008).

[262] Tokano, T. Dune-forming winds on Titan and the influence of topography. *Icarus* **194**, 243–262 (2008).

[263] Moore, J. & Howard, A. Are the basins of Titan's Hotei Regio and Tui Regio sites of former low latitude seas? *Geophysical Research Letters* **37** (2010).

[264] Voigt, A., Held, I. M. & Marotzke, J. Hadley cell dynamics in a virtually dry snowball Earth atmosphere. *Journal of the Atmospheric Sciences* **69**, 116–128 (2012).

[265] Byrne, M. P. & Schneider, T. Atmospheric dynamics feedback: Concept, simulations, and climate implications. *Journal of Climate* **31**, 3249–3264 (2018).

[266] Yang, J., Boué, G., Fabrycky, D. C. & Abbot, D. S. Strong dependence of the inner edge of the habitable zone on planetary rotation rate. *The Astrophysical Journal Letters* **787**, L2 (2014).

[267] Campbell, R. Debris flows originating from soil slips during rainstorms in Southern California. *Quarterly Journal of Engineering Geology* **7**, 339–349 (1974).

[268] Wordsworth, R. D. The climate of early Mars. *Annual Review of Earth and Planetary Sciences* **44**, 381–408 (2016).

[269] Scanlon, K. E., Head, J. W., Madeleine, J.-B., Wordsworth, R. D. & Forget, F. Orographic precipitation in valley network headwaters: Constraints on the ancient Martian atmosphere. *Geophysical Research Letters* **40**, 4182–4187 (2013).

[270] Wordsworth, R. *et al.* Global modelling of the early martian climate under a denser CO2 atmosphere: Water cycle and ice evolution. *Icarus* **222**, 1–19 (2013).

[271] Fastook, J. L. & Head, J. W. Glaciation in the Late Noachian Icy Highlands: Ice accumulation, distribution, flow rates, basal melting, and top-down melting rates and patterns. *Planetary and Space Science* **106**, 82–98 (2015).

[272] Forget, F. *et al.* 3D modelling of the early martian climate under a denser CO2 atmosphere: Temperatures and CO2 ice clouds. *Icarus* **222**, 81–99 (2013).

[273] Mischna, M. A., Baker, V., Milliken, R., Richardson, M. & Lee, C. Effects of obliquity and water vapor/trace gas greenhouses in the early martian climate. *Journal of Geophysical Research: Planets* **118**, 560–576 (2013).

[274] Urata, R. A. & Toon, O. B. Simulations of the martian hydrologic cycle with a general circulation model: Implications for the ancient martian climate. *Icarus* **226**, 229–250 (2013).

[275] Soto, A., Mischna, M., Schneider, T., Lee, C. & Richardson, M. Martian atmospheric collapse: Idealized GCM studies. *Icarus* **250**, 553–569 (2015).

[276] Wordsworth, R. D., Kerber, L., Pierrehumbert, R. T., Forget, F. & Head, J. W. Comparison of "warm and wet" and "cold and icy" scenarios for early Mars in a 3-D climate model. *Journal of Geophysical Research: Planets* **120**, 1201–1219 (2015).

[277] Lora, J. M., Kataria, T. & Gao, P. Atmospheric circulation, chemistry, and infrared spectra of Titan-like exoplanets around different stellar types. *The Astrophysical Journal* **853**, 58 (2018).

[278] Radebaugh, J. *et al.* Mountains on Titan observed by cassini RADAR. *Icarus* **192**, 77–91 (2007).

[279] Mitri, G. *et al.* Mountains on Titan: Modeling and observations. *Journal of Geophysical Research: Planets* **115** (2010).

[280] Solomonidou, A. *et al.* Morphotectonic features on Titan and their possible origin. *Planetary and Space Science* **77**, 104–117 (2013).

[281] Cartwright, R., Clayton, J. A. & Kirk, R. L. Channel morphometry, sediment transport, and implications for tectonic activity and surficial ages of Titan basins. *Icarus* **214**, 561–570 (2011).

[282] Moore, J. M. & Pappalardo, R. T. Titan: An exogenic world? *Icarus* **212**, 790–806 (2011).

[283] Janssen, M. A. *et al.* Titan's surface at 2.18-cm wavelength imaged by the Cassini RADAR radiometer: Results and interpretations through the first ten years of observation. *Icarus* **270**, 443–459 (2016).

[284] Barnes, J. *et al.* Global-scale surface spectral variations on Titan seen from Cassini/VIMS. *Icarus* **186**, 242–258 (2007).

[285] Soderblom, L. *et al.* Correlations between Cassini VIMS spectra and RADAR SAR images: Implications for Titan's surface composition and the character of the Huygens Probe Landing Site. *Planetary and Space Science* **55**, 2025–2036 (2007).

[286] Hurst, M. D., Mudd, S. M., Yoo, K., Attal, M. & Walcott, R. Influence of lithology on hillslope morphology and response to tectonic forcing in the northern Sierra Nevada of California. *Journal of Geophysical Research: Earth Surface* **118**, 832–851 (2013).

[287] Caine, N. The rainfall intensity-duration control of shallow landslides and debris flows. *Geografiska annaler: Series A, Physical Geography* **62**, 23–27 (1980).

[288] Hewlett, J. D. & Hibbert, A. R. Moisture and energy conditions within a sloping soil mass during drainage. *Journal of Geophysical Research* **68**, 1081–1087 (1963).

[289] Sahany, S., Neelin, J. D., Hales, K. & Neale, R. B. Temperature–moisture dependence of the deep convective transition as a constraint on entrainment in climate models. *Journal of the Atmospheric Sciences* **69**, 1340–1358 (2012).